Resonant Coastal Waves and Superinertial Oscillations

A THESIS SUBMITTED TO THE GRADUATE DIVISION OF THE UNIVERSITY OF HAWAII IN PARTIAL FULFILLMENT OF THE REQUIREMENTS FOR THE DEGREE OF

MASTER OF SCIENCE

IN

OCEANOGRAPHY

AUGUST 1995

By

Claude Frederick Lumpkin

Thesis Committee:

Pierre Flament, Chairperson
Doug Luther
Mark Merrifield
Dennis Moore

We certify that we have read this thesis and that, in our opinion, it is satisfactory in scope and quality as a dissertation for the degree of Master of Science in Oceanography.

THESIS COMMITTEE

_____

Chairperson

_____

_____

_____

Acknowledgements

This work was developed in a series of meetings with Doug Luther, Pierre Flament, Dennis Moore and Mark Merrifield. The author would like to acknowledge these individuals for their guidance, insights, and the inspiration they helped provide. Janet Becker gave additional assistance with theory and data analysis. Discussions with the UH Physical Oceanography Graduate Students group (particularly Michael Sawyer, Sean Kennan and Reka Domokos) were also helpful. Doug Luther, Pierre Flament, Pat Caldwell, Tom Schroeder and Arnold Hori helped the author obtain the data. Funding for this project, and financial support for the author, was provided by the National Oceanic and Atmospheric Administration through the Maui Algae Bloom Project. The author would also like to thank his wife Cristina, who gave support through the bad times and helped celebrate the good times.

Abstract

Simple models of free and forced waves around a cylinder are reviewed and applied to simulate trapped waves around the Hawaiian Islands. Correspondences between theoretical eigenfrequencies obtained from these models and observed spectral peaks in sea level and current records provide evidence for low mode subinertial trapped waves, some not previously identified. Azimuthal phase differences estimated from multiple sea level stations around Kauai, Oahu and Hawaii are also consistent with a trapped wave description.

Superinertial, intertidal peaks are observed in sea level spectra, but not in current spectra. Coherence amplitude and phase suggests a propagating wave of low azimuthal mode around Kauai and Oahu. There is not conclusive phase evidence of superinertial wave propagation around Hawaii. Significant coherence between sea level at Kauai and Hawaii suggests a large-scale component to the intertidal signal. Hypotheses are presented for the superinertial oscillations, including resonance in the forcing, seiche motion, and a high-frequency eigenmode of the Pacific basin.

A simple model is developed describing direct wind forcing of trapped waves around a cylindrical island. In the model, a north-south wind stress acts as a body force on a surface mixed layer. Stratification is described by a constant buoyancy frequency. A rigid lid is imposed, and the depth-independent (barotropic) response is neglected. Length-scale independent linear dissipation is assumed. The baroclinic response in this model displays resonance at the eigenfrequencies of the free azimuthal mode one island-trapped wave. With a dissipation time scale of 15.8 days, first baroclinic mode subinertial trapped waves forced by a wind stress of 0.10 N/m^2 reach rms equivalent sea surface displacements of 1.1 cm, maximum alongshore velocities of 7.2 cm/s, maximum

isopycnal displacements of 16 m, and a Q of 14. This response is of the order of observed trapped waves at the island of Hawaii, suggesting that direct atmospheric forcing plays a significant role in the generation of island-trapped waves. Excitation of the baroclinic modes produces isopycnal displacements and alongshore currents well below the mixed layer near the island. A comparison with observations reveals that the higher baroclinic mode response is too large in the model. Suggestions are offered for future modeling endeavors.

Evidence that island-trapped energy from Hawaii leaks to the Maui group of islands (Maui, Molokai, Lanai and Kahoolawe) is demonstrated in time-dependent coherence peaks between sea level at Hilo (Hawaii) and Kahului (Maui). Energetic trapped wave events at Hilo correspond to periods of enhanced coherence between Hilo and Kahului. Hilo sea level and the north and east wind at Kahului are treated as inputs forcing Kahului sea level; the empirically-derived transfer function between Hilo and Kahului sea level has a significantly nonzero peak at the observed trapped wave period at Kahului. It is concluded that leakage is the dominant forcing mechanism for the observed trapped wave peak at Kahului.

Table of Contents

List of Tables

List of Figures

List of Symbols

$\boldsymbol{a}$	vector containing true transfer functions
a	island radius
$\mathbf{D}$	matrix containing cross-spectral terms (defined in eq. 6.57)
e_k	total horizontal specific kinetic energy
$\bar{e}_k$	far-field horizontal specific kinetic energy
e_p	specific potential energy
$\boldsymbol{F}$	vector containing forcing terms
f	frequency
f_o	inertial frequency
G_i	gain of tranfer function estimate α_i
g	gravitational acceleration
$H_m^{(i)}$	Hankel function of the i^{th} kind, order m
$h(n)$	equivalent depth of mode n
h_{mix}	depth of mixed layer
I_m	modified Bessel function of the first kind, order m
J_m	Bessel function of the first kind, order m
K_m	modified Bessel function of the second kind, order m
k	radial wavenumber (superinertial)
m	azimuthal mode index
N	buoyancy frequency
n	vertical mode index
$P(n)$	mode n amplitude of perturbation pressure
P_o	pressure amplitude term (defined in eq. 6.25a)
p	perturbation pressure
Q	resonance quality
R	radial structure function
r	radial coordinate
r_d	radius of deformation
S_{xx}	autospectrum of time series x
S_{xy}	cross-spectrum of time series x and y
S_{cw}	clockwise rotary spectrum
S_{ccw}	counter-clockwise rotary spectrum
T	wave period
$T_i(n)$	mode n amplitude of forcing term F_i
t	time
$U_3(n)$	mode n amplitude of vertical velocity
$\overline{U}_\alpha(n)$	mode n amplitude of far-field horizontal velocity (component α)
$\hat{U}_\alpha(n)$	mode n amplitude of total horizontal velocity (component α)
U_o	velocity amplitude term (defined in eq. 6.17b)
$\boldsymbol{u}$	velocity vector

$\boldsymbol{V}$	vector containing cross-spectral terms (defined in eq. 6.56)
x_1	eastward coordinate (Cartesian coordinate system)
x_2	northward coordinate (Cartesian coordinate system)
x_3	vertical coordinate (Cartesian coordinate system)
Y_m	Bessel function of the second kind, order m
z	vertical coordinate (cylindrical coordinate system)
$\boldsymbol{\alpha}$	vector containing estimated transfer functions
α, β	indices representing horizontal components
ε	square root of island radius a divided by radius of deformation r_d
$\varepsilon_{\alpha\beta}$	two-dimensional Levi-Civita symbol
η	vertical displacement from rest
η_{eq}	equivalent surface displacement
θ	azimuthal coordinate
κ	radial wavenumber (subinertial)
μ	damping coefficient
ξ_{ccw}	counter-clockwise amplitude term (defined in eq. 6.25b)
ξ_{cw}	clockwise amplitude term (defined in eq. 6.25c)
σ	nondimensionalized frequency (defined in eq. 6.17a)
σ_x^2	variance of time series x
τ_o	surface wind stress
Φ	phase
$\phi(n)$	vertical structure function of u_1, u_2 and p, mode n
$\varphi(n)$	vertical structure function of u_3 and η, mode n
ω	angular frequency

Chapter 1

Introduction

A decade has passed since Luther [1985] presented evidence of resonant coastal waves in sea level records from Kauai, Oahu, Hawaii, and the Maui island group (Maui, Lanai, Molokai and Kahoolawe, all separated by shallow channels; see Fig. 1). At the time, multiple sea level stations on a single Hawaiian island with an appreciable history of data collection existed only on Oahu, forcing Luther to extrapolate phase information from trapped waves at Oahu to the other islands. In light of observations collected since 1985, the suite of trapped waves around the Hawaiian Islands may now be examined in greater depth.

While many studies have examined trapped waves along a straight coast and seamount-trapped waves [Davis and Bogden, 1989; Brink, 1989; Brink, 1990], few have focused upon waves trapped to islands. However, island-trapped waves are perhaps the most dramatic form of non-vortical motion trapped to topography. The island geometry is closed, leading to quantization of the eigenfrequencies and possible resonance. Furthermore, waves around islands are exposed to direct wind forcing, the effectiveness of which will be examined in this paper. Island-trapped waves may thus be extremely energetic, narrow-band constituents of the flow field around islands.

The impact of resonant coastal waves on horizontal dispersion and residence times near Hawaii is demonstrated in Fig. 2. Band-passed currents (integrated over time) are shown in four frequency bands, including the subinertial band encompassing the gravest trapped wave around the island of Hawaii (this will be derived in Chapter 2). The currents were measured at 54 m depth off Keahole Pt. on the leeward side of Hawaii (Fig. 1; details on the data may be found in Chapter 3). Assuming the integrated currents ac-

curately emulate the Lagrangian drift of fluid particles, trapped waves were responsible for advection over 6 km compared to 2 km for inertial, diurnal and semidiurnal motion. A study of the near-inertial, tidal and intertidal currents around the Hawaiian Islands appears in Chapter A, along with an examination of the mean currents around the islands.

Waves trapped to an island have been modeled as barotropic Kelvin waves trapped to a vertically-walled cylinder by LONGUET-HIGGINS [1969]. WUNSCH [1972] extended this theory for internal coastal waves by replacing the total water depth with the equivalent depth of each baroclinic mode. While WUNSCH [1972] and HOGG [1980] chose the radius of the theoretical cylinder to fit an observed peak in current or temperature spectra, LUTHER [1985] reasoned that the ray path of the trapped waves should be mapped onto an appropriate equivalent radius. Luther calculated the theoretical periods of resonant Kelvin waves around each of the major Hawaiian Islands using equivalent radii calculated from the shape of the islands at 20 m depth (the 250 m isobath was used for the Maui group) and a yearly-averaged estimate of the first baroclinic equivalent depth. At each island, the theoretical period of the gravest mode fell within 12% of the period of a sea level spectral peak, in one case differing by only 1%. Phase differences for the Oahu stations in the trapped wave band corresponded to the expected azimuthal structure from the theory. Luther anticipated the existence of higher baroclinic mode coastal waves at all islands, and found sea level evidence for the second baroclinic mode wave at Oahu.

A surprising observation made by LUTHER [1985] was the presence of superinertial, intertidal peaks present in the sea level spectra of several islands. Nonzero phase differences for the Oahu stations led Luther to conclude that superinertial trapped waves of approximately 17–18 h period exist around each of the major Hawaiian islands.

WUNSCH [1972] considered scattering of an internal wave field incident upon a cylindrical island. He found a pseudo-resonant response at frequencies corresponding to a superinertial spectral peak in Bermuda thermocline temperature. LUTHER [1985] ruled out geometrically-dependent hypotheses such as trapped-leaky refraction for the superinertial oscillations he observed in Hawaiian sea level spectra, as the peaks occurred at 17–18 h period for several islands of different radii. Luther suspected that pseudo-resonant forcing may explain these spectral peaks. However, he noted that the pseudo-resonant dispersion curves derived by Wunsch were made under a small wavenumber approximation not applicable for the Hawaiian superinertial oscillations.

In their studies of motion at Bermuda, WUNSCH [1972] and HOGG [1980] found that trapped waves were seasonal, with greater energy in the winter months. This, along with strong coherence and large phase jumps between the trapped wave signal and the local winds, led them to conclude that the waves were a product of direct, local forcing. LUTHER [1985] suggested that direct forcing by a large-scale wind field would effectively excite the odd azimuthal modes. He also proposed that trapped waves at the Maui group of islands may be forced by leakage from the energetic wave trapped to the island of Hawaii. Leakage is possible when the islands are separated by a distance smaller than the decay scale of the waves, as is the case with Hawaii and the Maui island group. In addition, these islands have similar eigenfrequencies for the gravest mode, which allows co-resonant leakage. Evidence of leakage may be found in a coherence peak between sea level at Kahului (Maui) and Hilo (Hawaii) near the eigenfrequency of the Maui group's gravest trapped wave [LUTHER, 1985].

In this paper, the subinertial and superinertial oscillations described by LUTHER [1985] are examined in sea level and current records. The baroclinic trapped wave model for the subinertial waves is shown to be supported by newer data. Phase information

from multiple sea level stations at Kauai and Hawaii are consistent with the azimuthal structures assumed by Luther, and current spectra indicate the presence of a suite of higher trapped wave modes. The superinertial oscillations are shown to present a more challenging picture. A number of hypotheses are presented for this motion, but no definitive conclusions are drawn. Finally, this paper focuses upon local and remote forcing mechanisms for trapped waves around the Hawaiian Islands.

Chapter 2 examines motion around a right-walled cylinder, the framework used by LONGUET-HIGGINS [1969] in his examination of island-trapped waves. The addition of stratification admits subinertial baroclinic waves [WUNSCH, 1972]. This model is used to calculate the natural frequencies of coastal waves around the major Hawaiian Islands [LUTHER, 1985]. Superinertial oscillations are also considered in Chapter 2, where it is shown that there are no superinertial trapped solutions to the free set of vertically-separated governing equations [LONGUET-HIGGINS, 1969]. The maximum pseudo-resonant response of forced superintial oscillations [WUNSCH, 1972] is shown to join smoothly with the dispersion curves of subinertial trapped waves for azimuthal modes greater than the first. However, pseudo-resonance is shown to be a near-inertial phenomenon, and thus inappropriate to describe intertidal sea level oscillations at the Hawaiian Islands.

Chapter 3 provides background on the time series analyzed in this work, and describes the methods used to investigate trapped waves in the data.

Chapter 4 presents evidence that subinertial sea level autospectral and coherence peaks are consistent with the trapped wave model of Chapter 2, as demonstrated by LUTHER [1985]. Phase differences between multiple stations are in all cases consistent with an azimuthal mode one structure for the subinertial waves. Current spectra are also presented which suggest the existence of a suite of higher-mode trapped waves.

Attention is shifted to superinertial oscillations in Chapter 5. The autospectral peaks described by LUTHER [1985] are shown to be a strong feature of windward sea level stations, but not present in current spectra. Sea level cross-spectra indicate distinctly nonzero phase shifts for several closely-spaced stations (such as Nawiliwili and Port Allen, both on Kauai), while significant coherence between Hilo (Hawaii) and Nawiliwili indicates a large-scale component to the intertidal motion. Several hypotheses for the spectral peaks are considered, although no single model can account for all the observations.

In Chapter 6, two mechanisms are examined which may force subinertial trapped waves. A directly wind-forced model suggested by LUTHER [1985] is developed in Section 6.1. A spatially homogeneous wind field, modeled as a body force acting on a mixed layer of constant depth, is applied to an ocean containing a vertically-walled cylindrical island. The directly-forced Ekman flow in the mixed layer is interrupted by the presence of the island, which leads to vertical displacements and resulting geostrophic currents. For an assumed wind stress of 0.1 N/m^2, the model response is of the same order as observed sea surface displacements and alongshore currents in the trapped wave band. It is concluded that local forcing plays a significant role in the generation of trapped waves at the island of Hawaii. However, remote forcing mechanisms may play a rare but dominant role in the generation of these waves; trapped waves have been observed with responses an order of magnitude greater than those of the model. From a comparison of the model output with observations, it is concluded that future models need to incorporate scale-dependent dissipation, asymmetries in the forcing field, and geometrical complications such as sloping island flanks.

LUTHER's [1985] hypothesis of remote forcing via leakage is examined in Section 6.2. Coherence peaks between Hilo (Hawaii) and Kahului (Maui) suggest leakage of trapped

wave energy from Hawaii to the Maui island group. The results of a multiple regression analysis are presented which support this hypothesis. It is shown that the transfer function between Hilo and Kahului sea level has a peak at the observed trapped wave peak in the Kahului sea level autospectrum, and that a majority of the trapped wave variance at the Maui group may be attributed to leakage from the island of Hawaii.

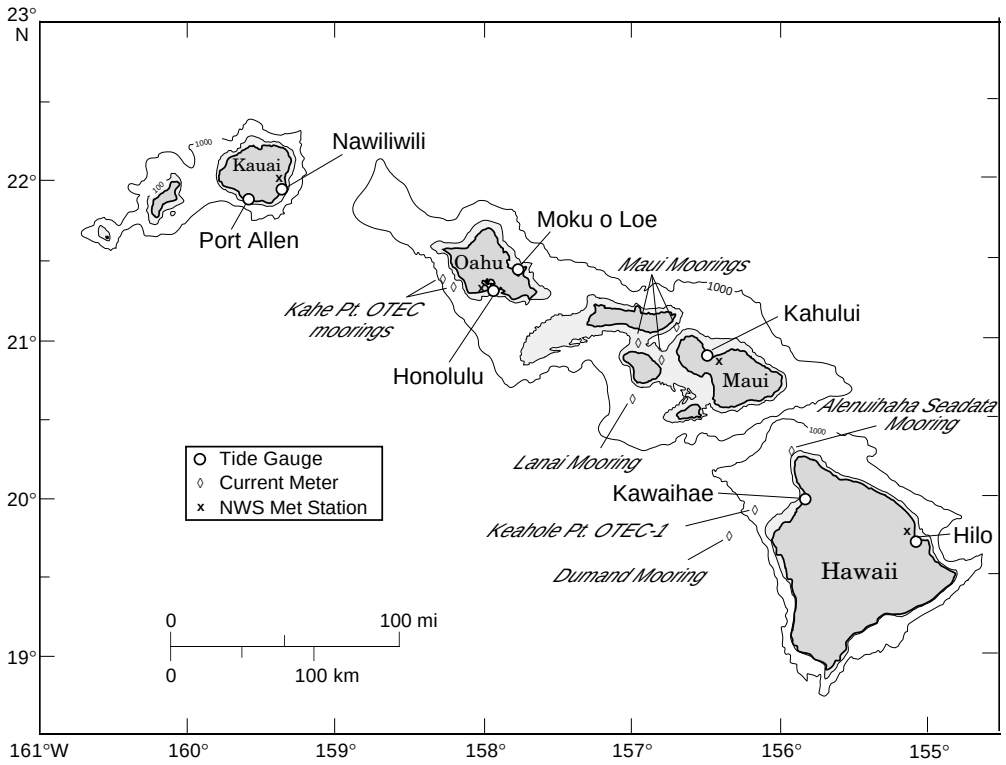

Figure 1: Sea level and meteorological stations and current meter sites mentioned in the text. Dark shading is land; light shading defines the 100 m isobath and indicates the rough outline of the island-trapped wave ray paths.

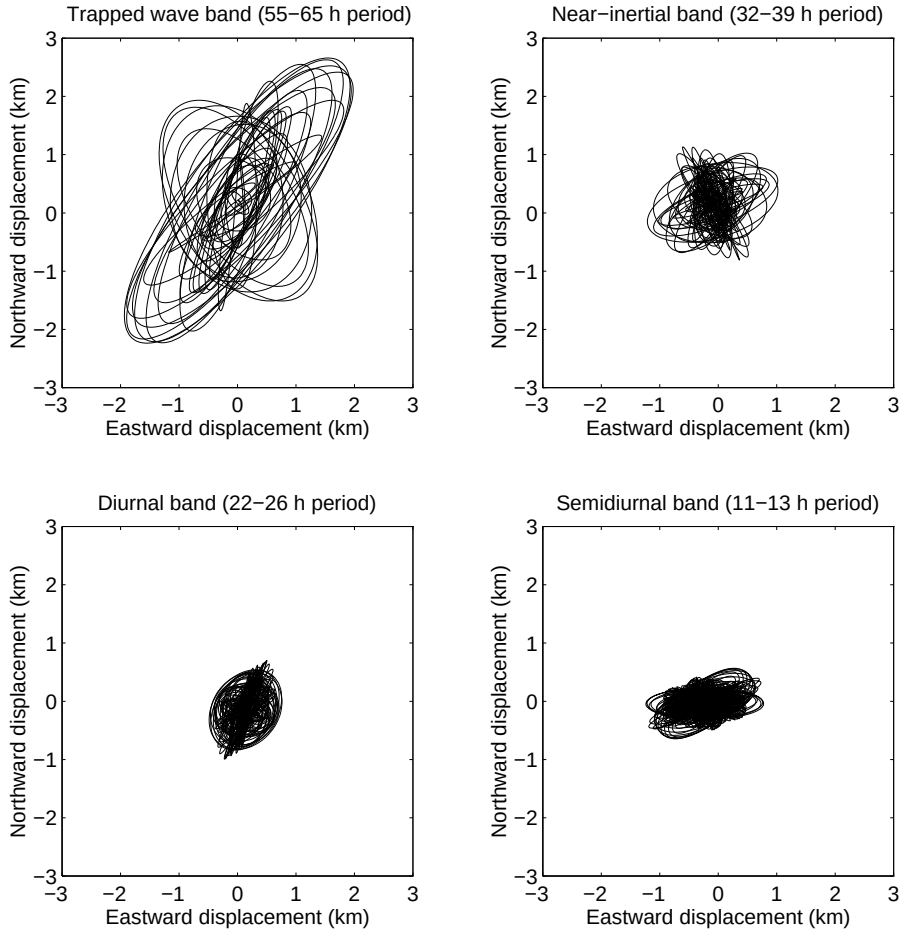

Figure 2: Progressive vector plots of the currents at the OTEC-1 Keahole Pt. site, off the leeward coast of Hawaii (see Fig. 1). The currents were measured by an Aanderaa RCM-4 meter. Band-passing has isolated the motion at 55–65 h period (top left), 32–39 h period (top right), 22–26 h period (bottom left) and 11–13 h period (bottom right). As will be shown in Chapter 2, the band from 55–65 h encompasses the gravest trapped wave around the island of Hawaii.

Chapter 2

Theory

The theoretical framework is described for examining island-trapped waves. Free solutions to the governing equations exist at the frequencies of resonant Kelvin waves. Pseudo-resonant forcing of superinertial waves is shown to result from incident internal plane waves at near-inertial frequencies.

2.1 Free waves trapped to a cylinder

The simplest geometry for studying waves trapped to an island is that of a vertically-walled cylinder in a hydrostatic, Boussinesq fluid on an f-plane. The nonsloping walls of the cylinder allow vertical separability of the equations of motion, and may be justified for the gravest internal modes if the deformation radii are much larger than the horizontal scale of the island flank.

In order to relate this geometry to that of an actual island with an irregular coastline, an appropriate "equivalent radius" must be chosen. Wunsch [1972] and Hogg [1980] chose an equivalent radius such that the theoretical gravest eigenfrequency matched an observed spectral peak, leading them to search for higher baroclinic mode peaks in order to justify the theory. Luther [1985] noted that the bathymetric outline of an island below the thermocline could be mapped onto an equivalent radius, on the physical grounds that the isobath determines the ray path of a subinertial Kelvin wave trapped to the island. This approach, and the relatively simple bathymetry of Kauai, Oahu and Hawaii, allowed him to approach the following framework with *a priori* equivalent radii for several of the Hawaiian Islands.

For vertically separable, hydrostatic motion bearing no potential vorticity on an f-plane, the motion is described by

$$r_d^2 \nabla^2 P - \left(1 + f_o^{-2} \partial_t^2\right) P = 0, \tag{2.1}$$

where ∇^2 is the horizontal Laplacian operator, r_d is the deformation radius $\sqrt{gh(n)}/f_o$, and the total perturbation pressure is

$$p(r,\theta,z,t) = \sum_{n=0}^{\infty} \phi(z;n) P(r,\theta,t;n). \tag{2.2}$$

(A derivation of (2.1) in the presence of forcing and dissipation is presented in Chapter 6.) For each mode n, the vertical dependence is described by the structure function ϕ. The separation constant has been formulated in terms of the equivalent depth $h(n)$. Solutions to the homogeneous equation (2.1) may be assumed of the form

$$P(r,\theta,t;n) = R(r;n,m)\mathrm{e}^{i(m\theta-\omega_{mn}t)}. \tag{2.3}$$

Substitution of (2.3) into (2.1) reveals that the radial structure functions satisfy the Bessel equation

$$r^2\partial_r^2 R + r\partial_r R + \left(k^2r^2 - m^2\right) R = 0, \tag{2.4}$$

where

$$k^2 = \frac{1}{r_d^2}\left(\frac{\omega_{mn}^2}{f_o^2} - 1\right). \tag{2.5}$$

In the superinertial regime $\omega/f_o > 1$, the radial wavenumber k is real and structure functions of the form $J_m(kr)$ and $Y_m(kr)$ are solutions to (2.4). If $\omega/f_o < 1$, k becomes imaginary and the modified Bessel functions K_m and I_m are appropriate (see Abramowitz and Stegun [1972], eqn. 9.6.3). Introducing a boundary at $r = a$ (the cylindrical island radius) imposes the material boundary condition

$$a\partial_r R(a) - \frac{f_o}{\omega_{mn}} m R(a) = 0, \tag{2.6}$$

which leads directly to the dispersion relation for the free system [Lamb, 1945].

Chambers [1965] examined superinertial barotropic eigenfrequencies around a cylindrical island within the framework outlined above. Using radial structure functions of

the form $Y_m(kr)$, he found theoretical eigenfrequencies of the same order as observed peaks in bottom pressure spectra off Guadelupe Island, Mexico. LONGUET-HIGGINS [1969] generalized Chambers' results by expressing the superinertial radial structure functions as an arbitrary real combination of J_m and Y_m. He noted that these functions decay like $r^{-1/2}$ at infinity, and thus contained finite energy outside an arbitrarily large radius, leading him to dismiss such solutions as not truly trapped.

LONGUET-HIGGINS [1969] first considered free barotropic subinertial waves trapped to an island. He discarded the solutions I_m so that energy would remain finite as $r \to \infty$; the material boundary condition then leads to a dispersion relation determined by

$$\frac{mK_m(\kappa a)}{\kappa a K'_m(\kappa a)} = \pm\sqrt{1 - \frac{(\kappa a)^2}{\varepsilon}} = \frac{\omega_m}{f_o} \tag{2.7}$$

where

$$\kappa^2 = \frac{1}{r_d^2}\left(1 - \frac{\omega_m^2}{f_o^2}\right) \tag{2.8}$$

and

$$\varepsilon = \left(\frac{a}{r_d}\right)^2. \tag{2.9}$$

This dispersion relation for the first four azimuthal modes appears as Fig. 3. Longuet-Higgins noted that one and only one anticyclonic solution exists for azimuthal mode m if

$$\varepsilon \geq m(m-1). \tag{2.10}$$

Longuet-Higgins interpreted this as giving a critical radius for each azimuthal mode; he included the gravest mode by defining a first azimuthal critical radius of zero. From the dispersion relation (2.7), Longuet-Higgins predicted a subinertial barotropic eigenfrequency infinitesimally lower than the inertial for Oahu. He noted that the trapping scale κ^{-1} was very large for this barotropic island-trapped wave; in fact, for Oahu values

of a, f_o and h_0, the trapping distance is many orders of magnitude larger than the circumference of the Earth. WUNSCH [1972] extended Longuet-Higgins' results to include baroclinic trapped waves by replacing the total depth h_0 by the appropriate equivalent depth of each internal mode. Due to the reduced phase speeds of the baroclinic waves, or equivalently due to the small Rossby radii, the internal trapped waves exist at frequencies measurably below inertial and are trapped relatively close to the islands (for Oahu values, the trapping scale is of order 150 km for the gravest internal mode).

LUTHER [1985] used the baroclinic version of (2.7) to predict the resonant periods of trapped waves at the major Hawaiian islands and compared them to the periods of observed sea level spectral peaks. These calculations are reproduced in Table 2.1. Note that all references to "theoretical periods" in the present work are also calculated using the baroclinic form of (2.7).

Table 2.1: Theoretical island-trapped wave periods using parameters chosen by LUTHER [1985]. No entry indicates the cutoff radius has been exceeded by the equivalent radius for that mode; consequently, no solution exists. Brackets indicate modes which are believed to be seen in the sea level data (see Table 4.1); parentheses indicate modes present in current meter data (see Section 4.2).

					Island-trapped wave period (days)			
	Inertial period	Equivalent Radius			1st baroclinic		2nd baroclinic	
Island	(days)	(km)	$\sqrt{\varepsilon_1}$	$\sqrt{\varepsilon_2}$	$m=1$	$m=2$	$m=1$	$m=2$
Kauai	1.33	24.7	.47	.94	[1.37]	—	1.87	—
Oahu	1.36	29.4	.55	1.09	[1.46]	—	[2.12]	—
Maui group	1.40	85.5	1.55	3.11	[2.82]	[1.47]	5.02	2.52
Hawaii	1.49	70.3	1.21	2.41	([2.50])	—	(4.29)	(2.16)

2.2 Pseudo-resonant scattering

A curious feature of the dispersion curves for the subinertial azimuthal modes $m \geq 2$ is their abrupt cutoff at the critical radius (see Fig. 3). From an analogy with Kelvin waves along a straight coast, one would expect the curve to pass smoothly into the superinertial regime. The superinertial dispersion relation derived by CHAMBERS [1965] defines curves which join smoothly with those of Fig. 3, but no physical argument for neglecting the J_m structure functions for all values of ka is immediately obvious.

The most appropriate physical condition which imposes a specific combination of the Y and J solutions is the radiation condition. WUNSCH [1972] examined these solutions for the system forced by incoming internal gravity plane waves; his results may be obtained as follows:

A hydrostatic pressure field with zero vertical average may be written as

$$p(\boldsymbol{x}, t) = \sum_{n=1}^{\infty} \phi(x_3; n) \sum_{m=-\infty}^{\infty} p(r, t; n, m) \mathrm{e}^{im\theta} \tag{2.11}$$

where ϕ is the baroclinic vertical structure function obeying

$$\frac{\mathrm{d}}{\mathrm{d}x_3}\left(\frac{1}{N^2}\frac{\mathrm{d}}{\mathrm{d}x_3}\phi\right) + \frac{1}{gh}\phi = 0. \tag{2.12}$$

Wunsch considered a cylinder of radius a struck by an incident wave given by

$$p_i = p_o \mathrm{e}^{-i(kr\cos\theta + \omega t)}. \tag{2.13}$$

The wavenumber k is given by (2.5), and the frequency is assumed positive (the wave is incident from the right). Wunsch let $p_o = 1$ and used

$$\frac{1}{2\pi}\int_0^{2\pi} \mathrm{d}\theta \ \mathrm{e}^{-i(kr\cos\theta - m\theta)} = \mathrm{e}^{-\frac{1}{2}m\pi i} J_m(kr) \tag{2.14}$$

[JONES, 1964, eqn. 1.208] and the fact that

$$p_i(r, t; n, m) = \frac{1}{2\pi}\int_0^{2\pi} \mathrm{d}\theta \ \mathrm{e}^{-i(kr\cos\theta + m\theta)} \mathrm{e}^{-i\omega t} \tag{2.15}$$

to find

$$p_i(r,\theta,t;n) = \sum_{m=-\infty}^{\infty} (-i)^m J_m(kr) \mathrm{e}^{i(m\theta-\omega t)}. \tag{2.16}$$

This must combine with a scattered solution $p_s(r,\theta,t;n)$ to satisfy the boundary condition of no normal flow at $r=a$. For outward radiation of p_s at $r=\infty$,

$$p_s(r,\theta,t;n) = \sum_{m=-\infty}^{\infty} b_m H_m^{(1)}(kr) \mathrm{e}^{i(m\theta-\omega t)}. \tag{2.17}$$

In order to satisfy the boundary condition

$$\left[\frac{f_o}{a}\partial_\theta + \partial_r\partial_t\right](p_i + p_r) = 0 \quad \text{at} \quad r=a, \tag{2.18}$$

the coefficients b_m are given by

$$b_m = (-i)^m \frac{kaJ'_m(ka) - \frac{f_o}{\omega}J_m(ka)}{kaH'^{(1)}_m(ka) - \frac{f_o}{\omega}mH_m^{(1)}(ka)}. \tag{2.19}$$

Then

$$\begin{aligned} p(r,\theta,t;n) \quad = \quad & \left[J_0(kr) - \tfrac{J'_0(ka)}{H'^{(1)}_0(ka)}H_0^{(1)}(kr)\right]\mathrm{e}^{-i\omega t} \\ & + \sum_{m=1}^{\infty}\left[J_m(kr) - \frac{kaJ'_m(ka) - \frac{f_o}{\omega}mJ_m(ka)}{kaH'^{(1)}_m(ka) - \frac{f_o}{\omega}mH_m^{(1)}(ka)}H_m^{(1)}(kr)\right]\mathrm{e}^{i(m\theta-\omega t)} \\ & + \sum_{m=1}^{\infty}\left[J_m(kr) - \frac{kaJ'_m(ka) + \frac{f_o}{\omega}mJ_m(ka)}{kaH'^{(1)}_m(ka) + \frac{f_o}{\omega}mH_m^{(1)}(ka)}H_m^{(1)}(kr)\right]\mathrm{e}^{-i(m\theta+\omega t)}. \end{aligned} \tag{2.20}$$

For $f_o > 0$, Wunsch noted that the denominator of the third line of this expression (corresponding to the clockwise-rotating part) could become very small. However, for any value of $\omega/f_o > 1$ the denominator never becomes zero. Thus, while no superinertial solutions to the free system exist when the radiation condition is imposed, a forced "pseudo-resonance" can occur at minimum values of

$$\left|kaH'^{(1)}_m(ka) \pm \frac{f_o}{\omega}mH_m^{(1)}(ka)\right|. \tag{2.21}$$

The pseudo-resonant behavior of (2.20) is apparent in graphs of the perturbation pressure $|p(r=a,\theta=0,t=0;n)|$ vs. ω/f_o for various values of ε (Fig. 4). Wunsch noted that a pseudo-resonant peak for a particular value of ε (i.e. a particular vertical mode) was constituted by a single azimuthal mode, and that the peaks occurred in a near-inertial frequency band for a large range of ε. As the value of ε is increased, higher azimuthal modes may become pseudo-resonant at increasingly off-inertial frequencies. This behavior of the pseudo-resonant peaks led him to conclude that a 20 h peak in Bermuda's thermocline temperature spectrum (latitude 32.3° N, inertial period 22.4 h) was a signature of this phenomenon. Lacking phase information for this signal, Wunsch concluded that the peak was probably a superposition of many azimuthal modes.

At near-inertial frequencies, ka becomes small and $H_m^{(1)}(ka) = J_m(ka) + iY_m(ka)$ is dominated by $Y_m(ka)$. Wunsch [1972] used this approximation to derive his pseudo-resonant dispersion curves. In this limit the pseudo-resonant curves correspond to the free solutions derived by Chambers [1965]. Luther [1985] found superinertial peaks in several Hawaiian sea level spectra; however, the peaks did not fall on Wunsch's pseudo-resonant dispersion curves, and an appropriate value of ka for the peak is $O(1)$. The roots of (2.21) may be determined graphically, extending Wunsch's formulation for $ka \not\ll 1$ (Fig. 5). However, these roots cannot account for the superinertial peaks observed by Luther [1985], as the magnitude of (2.21) only becomes small in the limit $ka \ll 1$. This may be emphasized by defining an arbitrary pseudo-resonant criteria, chosen in Fig. 5 to be

$$\left| kaH'^{(1)}_m(ka) \pm \frac{f_o}{\omega} mH_m^{(1)}(ka) \right| \leq 0.1, \tag{2.22}$$

and noting that the minimum value of the denominator rises quickly above this threshold as the frequency rises above the inertial.

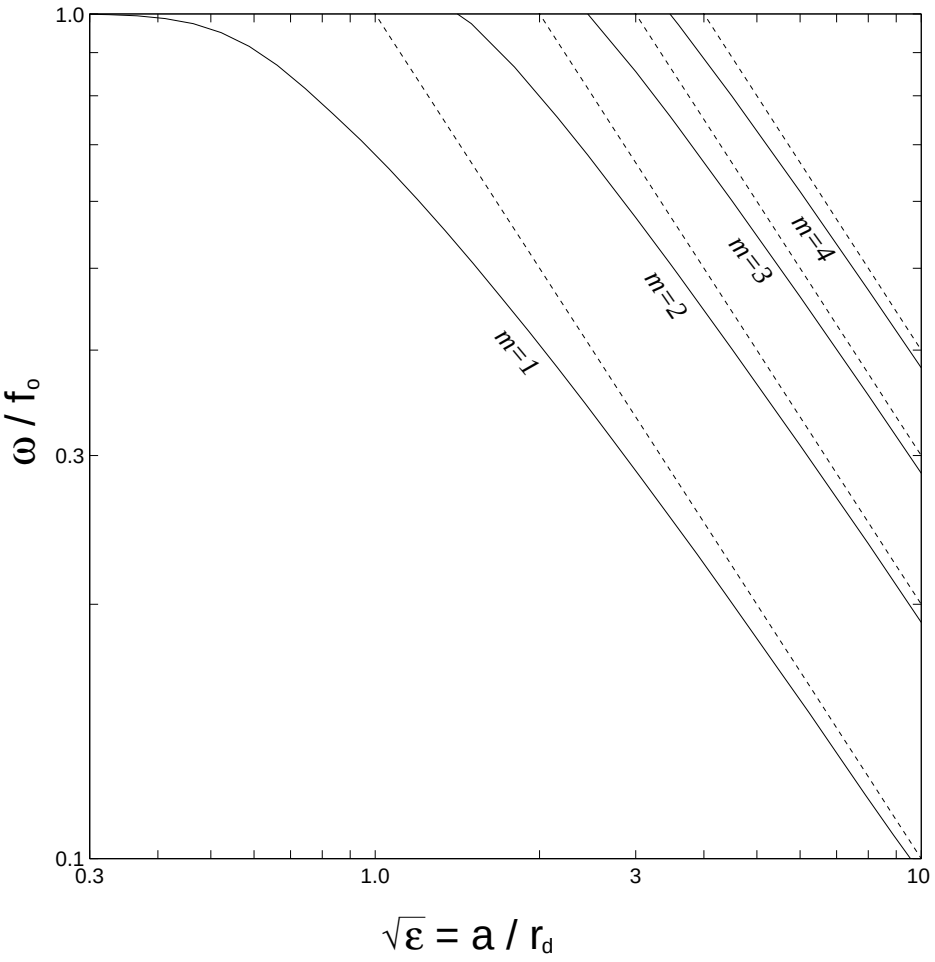

Figure 3: Dispersion curves for free subinertial island-trapped waves (solid lines), as derived by LONGUET-HIGGINS [1969] (equivalent to his Fig. 2). Azimuthal modes $m = 1$ through $m = 4$ are shown. Dispersion curves for Kelvin waves of the same wavelength along a straight coast are dashed. The first azimuthal mode exists for arbitrarily small ε (arbitrarily small island radius), while the higher modes have a "cut-off" frequency given by (2.10).

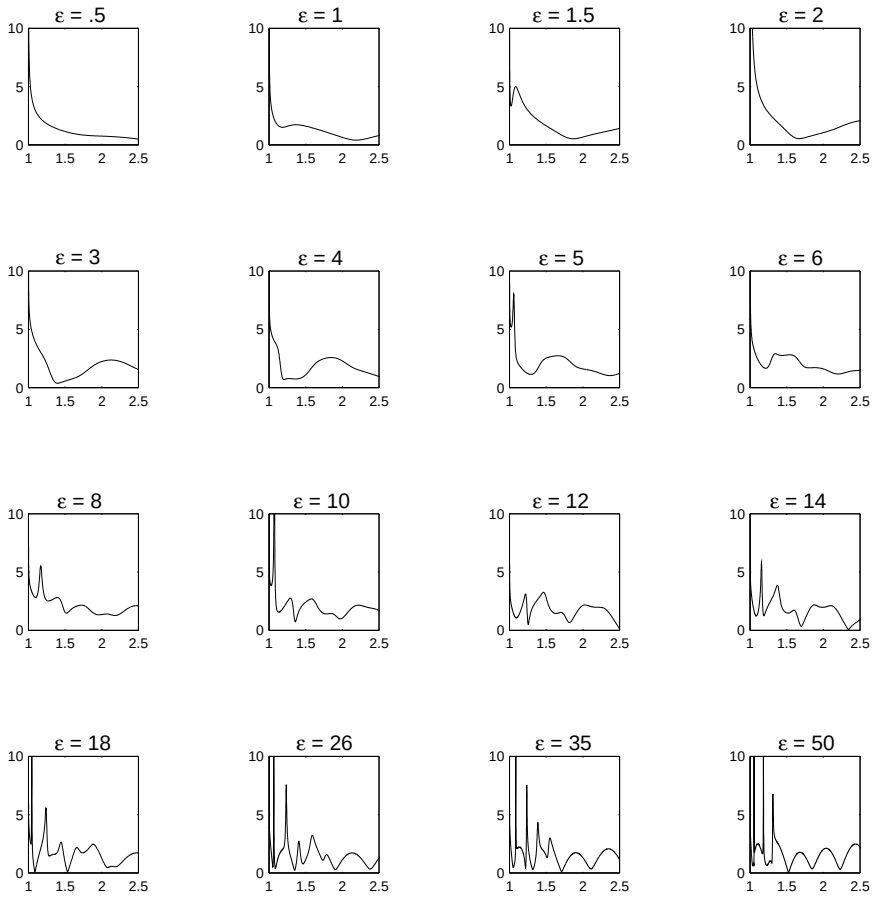

Figure 4: Plots of $|p(r = a, \theta = 0, t = 0; n)|$ (vertical axis) vs. ω/f_o (horizontal axis) for various values of the nondimensional parameter ε (see equation 2.20). As ε increases (i.e. as the island radius increases compared to the deformation radius), pseudo-resonant peaks appear at increasing values of ω/f_o. Each peak is dominated by a single anticyclonic azimuthal mode; for example, the peak at $\varepsilon = 8$ and $\varepsilon = 10$ is the contribution of the fourth azimuthal mode. Adapted from WUNSCH [1972], Fig. 7.

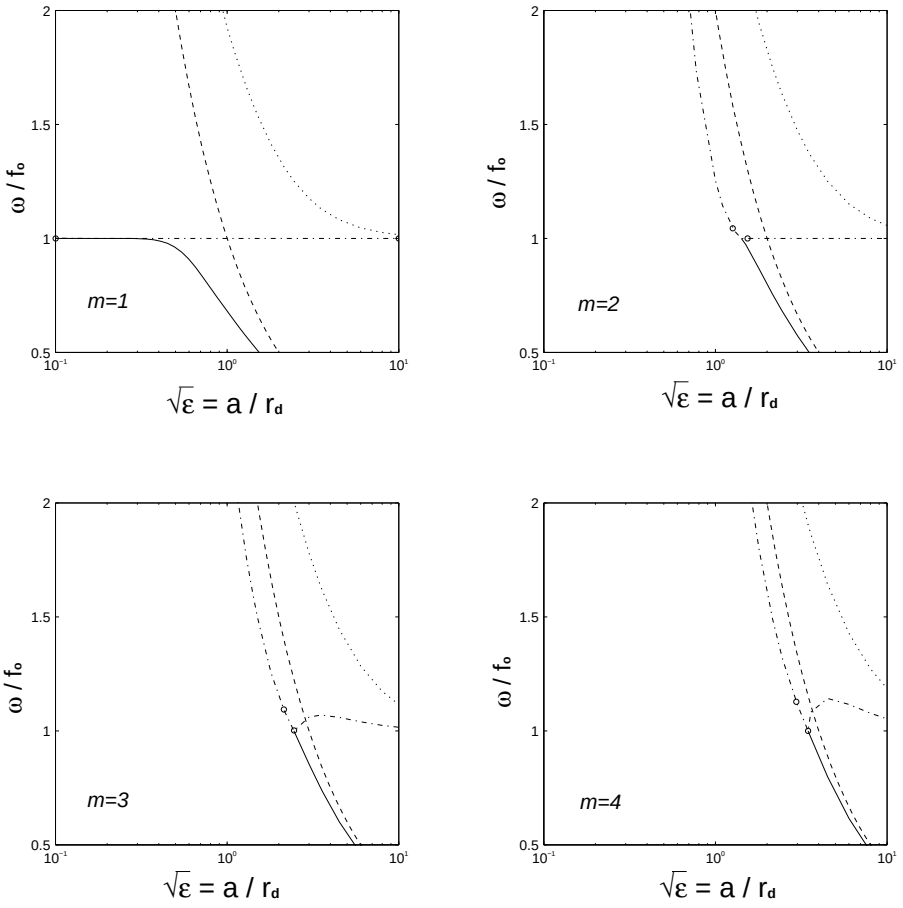

Figure 5: Dispersion curves for the first four subinertial azimuthal island-trapped waves (solid) and for straight-coast Kelvin waves of the same wavenumbers (dashed) as derived by LONGUET-HIGGINS [1969]. Azimuthal modes $m = 1$ through $m = 4$ are plotted separately. Minimum values of (2.21) in the superinertial regime are plotted for the cyclonic (dotted) and the anticyclonic (dot-dash) solutions. Pseudo-resonance, as defined by (2.22), occurs along the line segment marked by circles.

Chapter 3

Data and methods

Sources of sea level and current meter time series are described, and the data analysis methods are outlined.

3.1 Sea level

Three-hourly sea level records derived from the hourly data used by Luther [1985] were obtained for this study. The data were corrected for the inverse barometer effect using air pressure from nearby meteorological stations to yield adjusted sea level (ASL). A subset of these data was chosen for analysis, spanning 1 January 1966 to 31 December 1974 and free of gaps greater than a few hours. This allowed examination of coherent motions between the islands of Hawaii and the Maui group.

An additional source of data is recent National Oceanographic Data Center (NODC) hourly sea level measurements published on CD-ROM [NODC, 1994]. Records used from this source are summarized in Table 3.1.

Table 3.1: NODC (1994) sea level stations in the Hawaiian Islands (see Fig. 1).

Island	Sea level station	Years
Kauai	Nawiliwili	1973–1993
	Port Allen	1989–1993
Oahu	Honolulu	1973–1993
	Moku o Loe (Coconut Is.)	1981–1993
Maui	Kahului	1973–1993
Hawaii	Hilo	1973–1993
	Kawaihae	1989–1993

3.2 Air pressure

Hourly air pressure records were obtained from the Western Regional Climate Center and used to correct for the inverse barometer effect in the NODC sea level records. Time series were obtained for the period 1 January 1984 to 31 December 1993 at Hilo (Hawaii), Kahului (Maui), Honolulu (Oahu) and Lihue (Kauai). Amplitudes of neighboring stations (such as Hilo/Kahului) were highly coherent at periods larger than the semidiurnal, with similar energy density levels.

3.3 Currents

A number of current meters have been deployed for appreciable durations near the Hawaiian Islands, funded by private companies such as Ed Noda and Associates and by University of Hawaii projects such as the Deep Undersea Muon And Neutrino Detector (DUMAND) project. The sites chosen for analysis in this study are summarized in Tables 3.2 and 3.3 and discussed below.

Table 3.2: Current meter sites near Oahu (see Fig. 1). All instruments listed in this table were Aanderaa RCM-4 current meters.

Array name	Location	Dates	Total depth (m)	Instrument depth (m)
OTEC-4	21° 24.6' N, 158° 15.7' W	6/18/81–	907	43
Kahe	"	12/16/81	"	93
Point	"	"	"	143
	"	"	"	343
	"	"	"	793
TRW	21° 21.0' N, 158° 10.7' W	12/18/83–	762	752
OTEC-2	21° 21.2' N, 158° 9.9' W	3/20/84	610	600
Kahe	21° 21.3' N, 158° 9.3' W	"	396	386
Point	21° 20.9' N, 158° 9.0' W	"	79	41
	21° 21.9' N, 158° 9.1' W	"	78	40
	21° 21.5' N, 158° 8.6' W	"	24	20
	21° 21.0' N, 158° 8.6' W	"	"	"
	21° 21.9' N, 158° 8.8' W	"	"	"

Table 3.3: Current meter sites near Hawaii and the Maui island group (see Fig. 1).

Array name	Location	Dates	Total depth (m)	Instrument type*	Instrument depth (m)
OTEC-1	19° 54.5' N,	12/26/80–3/14/81	1346	A4	54
Keahole	156° 8.5' W	"	"	"	101
Point		"	"	"	151
		"	"	"	363
		"	"	"	771
Alenuihaha	20° 17.3' N,	5/6/84–7/26/84	169	SD	10.7
Seadata	155° 54.0' W	7/31/84–10/14/84	"	"	10
(1–7)		11/26/84–3/31/85	"	"	20
		4/1/85–7/9/85	"	"	10
		7/11/85–10/8/85	"	"	10
		10/8/85–1/23/86	"	"	10
		1/23/86–5/26/86	"	"	10
Lanai	20° 38.3' N,	9/30/91–10/20/91	497	S4	30
mooring	156° 58.0' W	"	"	A7	30
		"	"	"	448
DUMAND	19° 44.8' N,	3/13/92–9/30/92	4775	A7	4475
mooring	156° 19.6' W	"	"	"	4550

* A4=Aanderaa RCM-4, A7=Aanderaa RCM-7, S4=InterOcean S4 electromagnetic current meter, SD=Seadata 635-12 Directional Wave/current meter.

In the 1980's, Ed Noda and Associates conducted the OTEC Environmental Benchmark Survey Program consisting of extensive current measurements off Oahu and Hawaii (Fig. 1). The measurements were taken at depths of 10 to 800 meters with Aanderaa RCM-4 current meters with temperature sensors and with a Sea Data 635-12 Directional Wave/current meter.

The OTEC-1 Keahole Pt. mooring was in operation off the leeward coast of Hawaii from 26 December 1980 to 14 April 1981. It consisted of Aanderaa RCM-4 current meters at depths of 54, 101, 151, 363 and 771 m in water of total depth 1346 m. These meters recorded average water speed and direction every quarter hour. Subsequent

Noda deployments of Aanderaas at 10 m depth (not analyzed in this project) were conducted off Keahole Point in 1983–1985.

The OTEC program was focused off Kahe Pt. (Oahu) from the middle of 1980 until late 1984, with few observations made during the first two-thirds of 1982. Four moorings, each with Aanderaas at five different depths, were deployed in 1980 and 1981 for up to six months in duration. The OTEC-4 mooring, covering 18 June to 16 December 1981, was examined by LIEN [1985] with primary attention paid to the internal wave field. This mooring consisted of Aanderaas at 43, 93, 143, 343 and 793 m in 907 m total depth, with the instruments sampling every 20 minutes. After the hiatus in 1982 (in which two extremely short data sets were collected), the OTEC program continued off Kahu Pt. with a large number of near-bottom Aanderaa deployments at 10 to 800 meter depth for typically one to three months. The TRW OTEC-2 moorings, in operation from 18 December to 20 March 1984, were a subset of this phase of the OTEC program.

As part of the Hawaii Deep Water Cable Program, Noda and Associates measured currents in the Alenuihaha Channel between Hawaii and Maui from 5 May 1984 to 26 May 1986 (additional data has been collected since but is not analyzed here). Noda and Associates used a Sea Data 635-12 Directional Wave/current meter which measured water velocity with a Marsh-McBirney electromagnetic current meter. The instrument collected data over the two-year interval with occasional short breaks required for servicing (these gaps are noted in Table 3.3).

Also included in this data report are the Lanai and DUMAND moorings deployed by the University of Hawaii. The Lanai mooring was in operation from 30 September to 20 October 1991 in 497 m deep water south of Lanai in the Maui island group. It employed a near-surface InterOcean S4 electromagnetic current meter and Aanderaa RCM-7 current meter and a second near-bottom RCM-7. The DUMAND mooring collected data from

13 March to 9 September 1992 in nearly 5 km deep water off Hawaii, near the Keahole Pt. site mentioned above.

Three additional moorings were deployed on 26 September 1994 in the channels between Maui, Molokai and Lanai and will be recovered in the Fall of 1995. The data from the four current meters used in the Maui moorings should relate valuable information on the flow field through the shallow channels of the island group and help quantify the damping effect of these channels on island-trapped waves.

3.4 Methods

3.4.1 Tidal filtering

To reduce side-lobe leakage of the tides in sea level and current spectra, filtering was performed via a least-squares fit of the prominent diurnal and semidiurnal constituents. The frequencies of these constituents were calculated from the Doodson numbers [GODIN, 1972]; the amplitude and phase were determined in the least-squares operation.

The length of the sea level time series allowed a fit of the 49 largest tidal constituents, which lowered the diurnal and semidiurnal spectral peaks to within an order of magnitude of the background energy level. Because the typical record length of current meter series was 120 days, fewer tidal constituents could be successfully filtered. For example, the S_2 and K_2 tides and the K_1 and P_1 tides could not be resolved, as both pairs beat at 183 days. Consequently, six diurnal and semidiurnal constituents were used for filtering the current meter series. The variance of the dominant semidiurnal motion was not reduced by more than a factor of 3, presumably due to drifting phase of the internal tide signal. The technique is sufficient, however, to lower the magnitude of tidal peaks by a factor of two to three and allow examination of intertidal motion.

3.4.2 Spectral analysis

Because island-trapped waves are not stationary (they are event-like and seasonal, LUTHER [1985]), a 10% cosine window was applied to reduce spectral leakage without placing undesired emphasis on the central portion of the time series (the trend and mean were removed before applying this window). The variance and number of degrees of freedom of the spectra were adjusted to compensate for the window.

MATLAB's *FFT* routine was used to calculate the Fourier coefficients. The spectra were pre-whitened by multiplication with ω, smoothed in frequency space, and post-reddened to produce the spectra presented in the figures. Smoothing was conducted as a simple box average, with every other point calculated from independent unsmoothed coefficients. Pre-whitening did not visibly affect the smoothed spectra except for a slight lowering of energy in the lowest few frequency bins.

All spectra were normalized such that the variance σ_x^2 of a stationary random variable $X(t)$ is given by

$$\sigma_x^2 = \int_0^\infty \mathrm{d}\omega \; S_{xx}(\omega) \tag{3.1}$$

where S_{xx} is the spectral energy density. The 95% confidence limits were assigned to the spectra under the assumption that the spectral energy densities follow a chi-squared distribution [BENDAT AND PIERSOL, 1986, eq. 8.159]. The 95% confidence limit for the null hypothesis in coherence amplitude plots was calculated using KOOPMAN's [1974] coherence confidence intervals.

The counter-clockwise and clockwise rotary spectra are

$$S_{CCW} = \frac{1}{2}\left(S_{u_1u_1} + S_{u_2u_2}\right) + Q_{u_1u_2}, \qquad S_{CW} = \frac{1}{2}\left(S_{u_1u_1} + S_{u_2u_2}\right) - Q_{u_1u_2}, \tag{3.2}$$

where $S_{u_iu_i}$ is the autospectrum of velocity component u_i and $Q_{u_iu_j}$ is the quad-spectrum between velocity components u_i and u_j [LIEN, 1985; BENDAT AND PIERSOL, 1986]. It

can be shown [MÜLLER AND SIEDLER, 1976] that the ratio of counter-clockwise to clockwise energy for free linear internal gravity waves obeys the consistency relation

$$\frac{S_{CCW}}{S_{CW}} = \frac{(\omega - f_o)^2}{(\omega + f_o)^2}. \tag{3.3}$$

The 95% confidence limits for the rotary energy ratio estimates were calculated using the F-distribution, as given by LIEN [1985].

Spectrograms of energy density vs. time were created for the current records in order to identify energetic events. These were constructed by dividing the original time series into segments of length 1024 h ($\approx$ 43 days) which overlapped by 93% ($\approx$ 40 days). In order to reduce spectral leakage and emphasize the central portion of the segment, a hanning window was applied to each segment before calculating the spectrum. Energy densities in the spectrograms were gray-scaled from black (low energy) to white (high energy). "Relative amplitude" plots were created identically, except the mean energy from each frequency bin was removed before creating the gray scale image. Because the amplitude of each 1024 h segment is plotted at the central time of the segment, all gray scale images begin 512 h ($\approx$ 21 days) into the total record and stop the same amount of time before the end of the record.

Running coherence plots were created in a similar manner to the spectrograms in order to display the coherence between two sea level stations as a function of time. The length of the subrecords was varied according to the width of the frequency band, with narrow bands requiring longer subrecords for a fixed level of 95% significance. Consecutive subrecords overlapped by 93% of their length. The auto- and cross-spectra were calculated, and spectral coefficients outside the frequency band of interest were discarded. A mean was calculated from the remaining terms, with a 95% confidence level estimated from the number of terms entering the average.

3.4.3 Non-spectral techniques

The air pressure time series contained many gaps of length 1–3 hours, with a few gaps of longer duration. Gaps of 24 h or less were treated by removing the tidal signal and filling the gaps with a linear fit between the endpoints.

Complex demodulations at desired frequencies were performed using a five-point Butterworth IIR filter and MATLAB's efficient *filtfilt* routine. Lowpass filter widths are given in terms of the equivalent bandpass periods in all plots of demodulated amplitude.

A principle component analysis of the currents from the inertial to 3 day periods was performed. The axes of maximum/minimum variance for this subinertial band, which contains the gravest Hawaiian coastal waves, were used to define the local azimuthal (alongshore) and radial (offshore) coordinates. At all current meter sites except the S4 at the Lanai site, where the subinertial motion was nearly circularly polarized, the azimuthal direction aligned very closely with the local isobaths (see Figs. 45, 46).

Chapter 4

Observations of subinertial trapped waves

Resonant periods of subinertial baroclinic coastal waves trapped to the major Hawaiian Islands correspond with peaks in sea level and current meter spectra. Phase information from concurrent sea level series is consistent with the trapped wave description.

4.1 Sea level

Sea level spectra from stations around the Hawaiian Islands contain energetic peaks from the inertial to several days period [Longuet-Higgins, 1969; Miyata and Groves, 1971; Luther, 1985]. Winter and summer month spectra (Figs. 6 and 7) demonstrate the strong seasonality of these peaks [Luther, 1985].

Luther [1985] found that the periods of these peaks were in close agreement with the theoretical resonant periods of low vertical mode trapped waves, all of azimuthal mode one (calculated as in Chapter 2). For concurrent series on Oahu, he found a phase difference in the subinertial band appropriate for an azimuthal mode one wave.

Since 1985, concurrent sea level records have been collected on Kauai, Oahu and Hawaii (see Table 3.1). Spectral peaks and phases are consistent with Luther's [1985] conclusion that resonant baroclinic coastal waves exist at each of the major Hawaiian Islands.

Spectral peaks believed to be associated with trapped waves are summarized in Table 4.1 and discussed on an island-by-island basis below.

4.1.1 Kauai

Concurrent sea level measurements at Port Allen and Nawiliwili date from 1989. Spectra of the two time series (Fig. 8) have a significant peak at 1.55 days period. A coherence amplitude greater than 0.9 is found between the two records in this band (Fig. 9). The azimuthal distance from Nawiliwili to Port Allen is roughly 1/5 the circumference of

Table 4.1: Island-trapped waves observed in sea level spectra (adapted from LUTHER [1985], Table 2). Theoretical phase shifts are calculated from the separation distance of the sea level stations and the equivalent circumference of the islands (values from LUTHER [1985]). A "N/A" appears for observations made while only one station was in operation on that island.

	INERTIAL	TRAPPED WAVE	OBSERVED		THEORETICAL CW	
	PERIOD	PERIOD	COHERENCE[1]		AZIMUTHAL MODES:	
ISLAND	(days)	(days)	AMP.	PHASE	$m = 1$	$m = 2$
Kauai	1.33	1.56	0.9	73° ± 22°	70°	140°
Oahu	1.36	2.0	0.8	148° ± 22°	104°	-152°
		1.5	0.8	127° ± 21°	104°	-152°
Maui	1.40	1.69	(std. dev.=4 h)[2]		N/A	N/A
group		2.62	(std. dev.=4.2 h)[2]		N/A	N/A
Hawaii	1.50	2.47	0.9	120° ± 17°	112°	-136°
		2.51	(std. dev.=1.4 h)[3]		N/A	N/A

(1) Station pairs for each island are given in Table 2.1.
(2) Calculated from periods of peaks in Kahului ASL spectra, 1966–1974 (winter months).
(3) Calculated from periods of peaks in Hilo ASL spectra, 1966–1974 (winter months).

Kauai, such that the observed phase shift is consistent with a clockwise azimuthal mode one trapped wave (Table 4.1).

The 1.55 day peak may be identified as the first baroclinic, first azimuthal island-trapped wave (theoretical period 1.37 days). Although the theoretical and observed peaks are significantly different, this identification is supported by the period of the autospectral and coherence peaks and the phase (appropriate for the first azimuthal mode). Kauai's geometry is relatively simple; the error is probably not in the estimate of the equivalent radius. As demonstrated by HOGG [1980], the effect of bottom slope should be a lowering of the eigenfrequency, perhaps explaining the larger observed period.

4.1.2 Oahu

Spectral peaks at 1.44–1.48 and 1.93–2.01 days period (Fig. 10) correspond closely to the theoretical periods of 1.46 and 2.1 days for the first and second baroclinic, first azimuthal trapped waves in an ocean of constant stratification [LUTHER, 1985]. The peak corresponding to the second baroclinic mode is especially prominent in the Moku o Loe spectrum. The coherence amplitude and phase (Fig. 11) between the ASL time series are not qualitatively different from those obtained by LUTHER [1985], indicating that a first azimuthal structure is consistent with the observations (although the azimuthal distance between Moku o Loe and Honolulu may have been underestimated; see Table 4.1).

4.1.3 Hawaii

Sea level spectra from Hilo and Kawaihae on the island of Hawaii contain an energetic peak consistent with the gravest mode of the baroclinic trapped wave model (Fig. 12). Peaks exist at 2.47 days period in both spectra. The coherence amplitude is greater than 0.9 from 2.50 to 2.58 days period, with the appropriate phase shift for an azimuthal mode one wave (Fig. 13, Table 4.1).

4.1.4 Maui group

LUTHER [1985] noted that the islands of Maui, Molokai, Lanai and Kahoolawe are separated by shallow channels and appear to be a single island below the base of the thermocline (see Fig. 1). Due to the irregular geometry of the Maui island group (which includes the shallow Penguin Bank), Luther offered two possibilities for the appropriate equivalent radius. The larger of the two radii (85.5 km, used in the calculations presented in Table 2.1), resulted in a theoretical period closest to the observed 2.61 day peak in the Kahului spectrum (Fig. 7).

Peaks in the Kahului ASL spectrum at around 1.7 days period (Fig. 7), not mentioned by LUTHER [1985], occur near the theoretical period of the first baroclinic, second azimuthal Maui group trapped wave. Additional sea level records, such as data collected at the Pacific Tsunami Warning Center site on the north shore of Molokai (not obtained for this analysis), must be used to test the phase prediction of this identification. LUTHER [1985] argued that odd azimuthal modes would be preferentially excited by spatially homogeneous wind forcing. The complicated geometry of the Maui group, however, may result in displacements on opposite sides of the group projecting onto the gravest even and odd modes without appreciable bias when mapped onto a cylinder of appropriate radius (evidence of this may be seen in the coherence between ASL and the north wind at Kahului; Fig. 39). Thus, the existence of an energetic second azimuthal mode in the Kahului spectrum is not particularly anomalous.

While a wave trapped solely around Maui (rather than the entire group) would have a near-inertial period in theory, its trapping scale would be much greater than the radius of deformation. Due to the proximity of neighboring islands in the Maui group, such a wave cannot account for the energetic 1.7 day peak seen in Fig. 7.

4.2 Currents

4.2.1 Kahe Pt. (Oahu)

None of the OTEC Kahe Pt. current meter and temperature spectra examined in this study contains significant energetic peaks at the island-trapped wave eigenfrequencies. The OTEC-4 mooring was in operation during summer and fall months, perhaps explaining why LIEN (1985) did not observe a strong trapped wave signal (the focus of his study was freely-propagating internal waves). Later in the OTEC program, Kahe Point current meters were placed near the bottom in all seasons (see Table 3.2). Some spectral peaks from these moorings suggest trapped wave activity (Fig. 14), but none

offer dramatic evidence for the existence of resonant coastal waves. An examination of the vertical structure of baroclinic trapped waves on a sloping bottom may clarify why subinertial peaks are not a stronger feature of these data.

4.2.2 Alenuihaha Seadata site (Hawaii)

Current meter spectra from the Alenuihaha Seadata site are examined in Chapter 6 in a comparison with the output of a wind-forced model. Spectral peaks in the subinertial band are suggestive of higher baroclinic mode trapped waves (see Fig. 32). In the winter of 1984–1985, alongshore currents at this site reached $O(50)$ cm/s in the gravest trapped wave frequency band (see Fig. 43).

4.2.3 Keahole Pt. (Hawaii)

Azimuthal velocity spectra from the Keahole Pt. Aanderaas (Fig. 15) contain the peaks listed in Table 4.2. Significant peaks at 2.75 and 4.44 days period may be identified as the first azimuthal, first baroclinic trapped wave (theoretical period 2.50 days period) and the first azimuthal, second baroclinic trapped wave (theoretical period 4.29 days period). Furthermore, a peak appears in all spectra at 2.24 days period, close to the theoretical period of 2.16 days for the second baroclinic, second azimuthal trapped wave. These peaks indicate that a suite of resonant coastal waves exists around Hawaii, particularly in the winter months in which the gravest mode is a strong signature of the sea level records. Due to the persistence of the peaks at 2.75 days, 2.24 days and 1.5–1.6 days period, the vertical structure of this motion may be examined from the spectral estimates (Fig. 16).

The spectrum of Hilo sea level (not shown) concurrent with the Keahole Pt. record has a significant peak at 2.79 days period. Interpreting this peak and the 2.75 day peaks in the current spectra as signatures of the gravest mode trapped wave presents

Table 4.2: Spectral peaks in the alongshore velocity at the OTEC-1 Keahole Pt. mooring.

Depth (m)	Period	rms azimuthal velocity
54	2.75 days	2.06 cm/s
	2.24 days	1.37 cm/s
	1.64 days	1.21 cm/s
101	2.75 days	1.75 cm/s
	2.24 days	1.60 cm/s
	1.57 days	1.36 cm/s
151	2.75 days	2.10 cm/s
	2.24 days	1.69 cm/s
	1.71 days	1.40 cm/s
	1.50 days	1.00 cm/s
363	3.96 days	0.62 cm/s
	2.76 days	1.35 cm/s
	2.25 days	0.79 cm/s
	1.89 days	0.52 cm/s
771	4.44 days	0.66 cm/s
	2.24 days	0.35 cm/s
	1.56 days	0.40 cm/s

a conundrum: the equivalent depth for the first baroclinic mode must be 0.65 m to result in a theoretical trapped wave period of 2.75 days (keeping all other parameters fixed). This equivalent depth is significantly shallower than the range of annual variation tabulated by Luther [1985]. In order to examine this discrepancy, a future project could compare a time series of the theoretical first baroclinic equivalent depth, obtained from subinertial peaks in Hilo sea level spectra, with the equivalent depth calculated from *in situ* measurements of the stratification near Hawaii. If time series of stratification variability can be derived from sea level records, such a project would reap beneficial results for future studies of internal motion near the Hawaiian Islands.

Upon calculating coherence between the 54 m record and lower records, it became clear from phase wrapping that the record had been offset by an appreciable lag/lead. In order to evaluate the true start time for the data, the correlation coefficients were calculated between all five records for the azimuthal velocity and the azimuthal tidal currents (band-passed from 10 to 14 h and from 20 to 28 h). The azimuthal direction was fixed at 27.3° from true north for all three records. Results from this analysis suggested that the upper record leads the 101 m record by 27.5 h, and leads the 151 m record by 27.75 h. After correcting for these offsets, phase wrapping was no longer apparent in the coherence phases, and phase lags for the semidiurnal coherence peaks were close to zero.

Significant coherence peaks between the top three current meters of the Keahole mooring are listed in Table 4.3. The subinertial peaks correspond to the first and second baroclinic, first azimuthal trapped waves mentioned earlier. There is a significant coherence peak at approximately 20 h period, although there are no significant autospectral peaks for any of the spectra at 20 h. Coherence peaks at the semidiurnal period (and its first harmonic, not listed in Table 4.3) are a clear feature of the cross-spectra. A near-inertial coherence peak between the 54 m and 101 m record is barely significant at the 95% confidence level; phase resolution is not sufficient to verify that the motion corresponds to downward-propagating near-inertial internal waves.

In order to expand our understanding of the trapped waves captured in these time series, a future study needs to examine the structure and natural periods of trapped waves on a steep slope, combined with the hydrography of the Keahole Pt. site. This project, which will require an appreciable synthesis of theory and observation, will also demand the development of a forced trapped wave model beyond the scope of the model presented in Chapter 6.

Table 4.3: Coherence peaks between the top three Aanderaas of the Keahole Pt. mooring.

Coherence peaks between 54 m and 101 m			
Period	Amplitude	Phase	(pos.=101 m leads)
4.18 days	0.87	-25°± 42°	
2.34 days	0.92	-3°± 40°	
1.15 days	0.65	-19°± 59°	
20.9 h	0.78	7°± 43°	
11.97 h	0.93	6°± 27°	
Coherence peaks between 101 m and 151 m			
Period	Amplitude	Phase	(pos.=151 m leads)
4.26 days	0.78	34°± 48°	
2.39 days	0.85	-16°± 43°	
12.76 h	0.61	-4°± 46°	
Coherence peaks between 54 m and 151 m			
Period	Amplitude	Phase	(pos.=151 m leads)
4.17 days	0.68	-1°± 59°	
2.34 days	0.94	-17°± 39°	
19.2 h	0.52	-19°± 90°	
12.49 h	0.63	-6°± 44°	

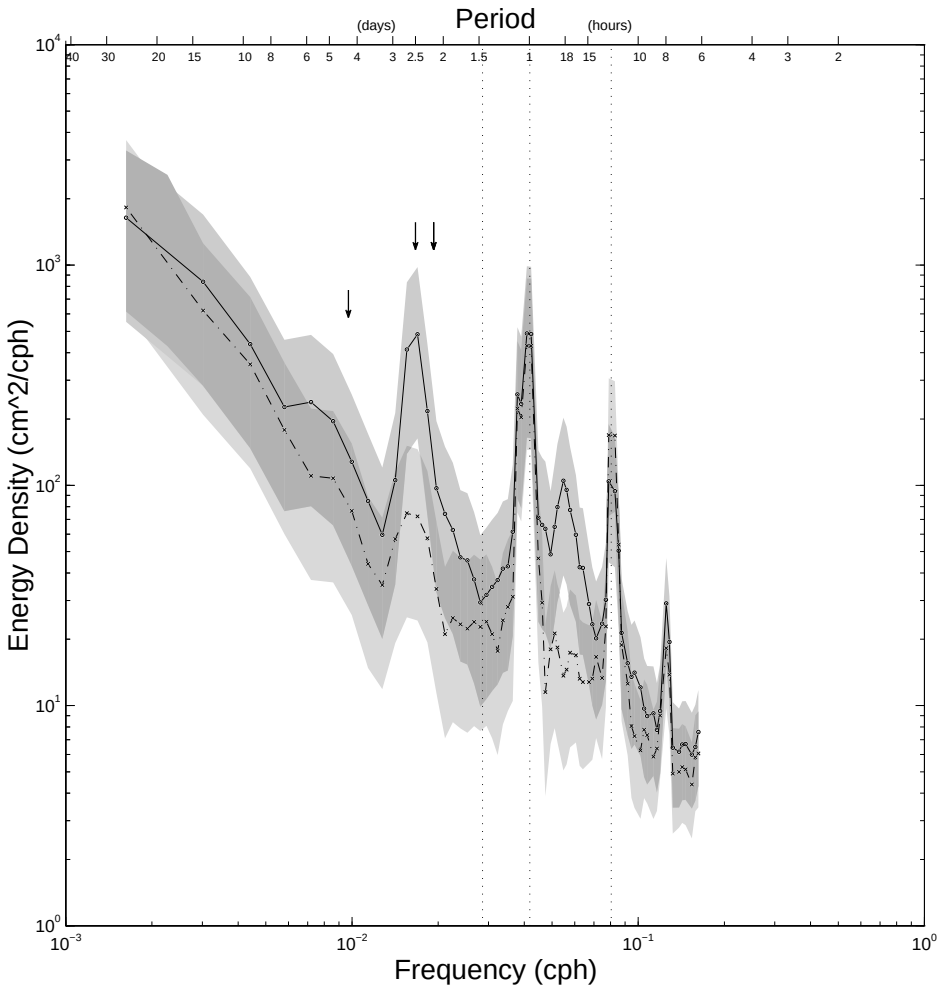

Figure 6: Winter (solid, darker confidence interval shading) and summer (dot-dash, lighter confidence interval shading) spectra of adjusted sea level at Hilo (Hawaii), 1966–1974. Inertial, diurnal and semidiurnal periods are marked by vertical dotted lines. Arrows indicate the theoretical periods of the first baroclinic, first azimuthal (center) and second baroclinic, first (left) and second (right) azimuthal trapped waves. The prominent subinertial peak in the winter spectrum is centered at 2.5 days period. The superinertial peak is centered at 18 h period.

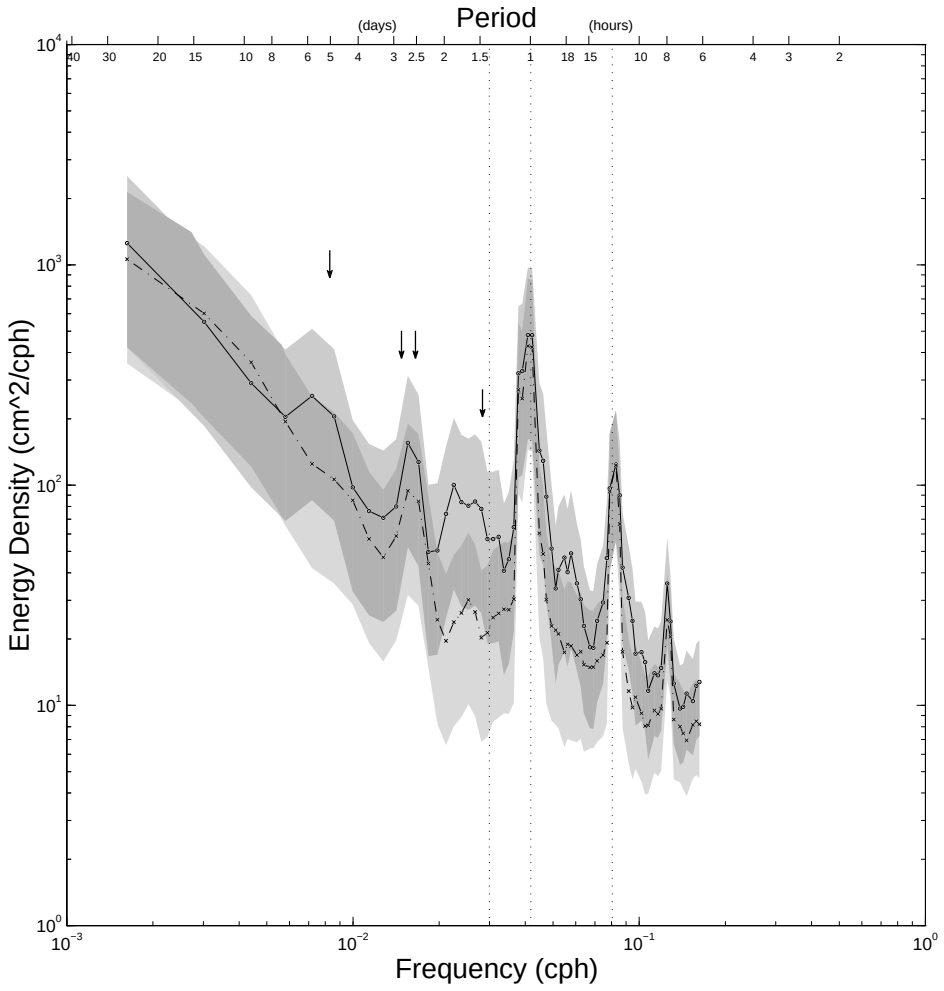

Figure 7: Winter (solid, darker confidence interval shading) and summer (dot-dash, lighter confidence interval shading) spectra of adjusted sea level at Kahului (Maui), 1966–1974. Arrows indicate the theoretical periods of the first and second baroclinic, first and second azimuthal trapped waves (see Table 2.1). There is a prominent subinertial peak at 2.61 days period. A secondary subinertial peak reaches a maximum at 1.85 days period. The intertidal peak in the winter spectrum has a maximum at 17.5-18.0 h period. The diurnal, semidiurnal and local inertial periods are marked by vertical dotted lines.

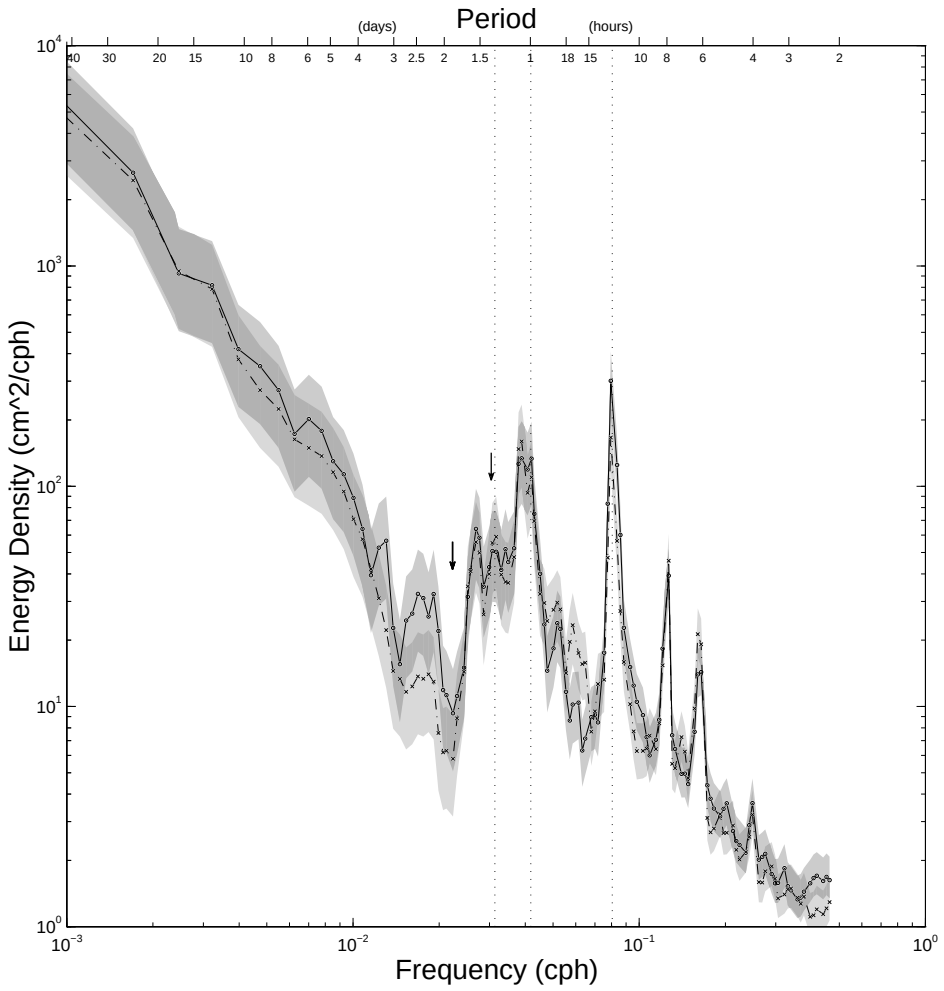

Figure 8: Adjusted sea level spectra for Nawiliwili (dot-dash) and Port Allen (solid) for the winters of 1990–1994. Arrows indicate the theoretical period of the first (right) and second (left) baroclinic, first azimuthal trapped waves. Both spectra have subinertial peaks at 1.55 days period (the local inertial period is 1.33 days). The Port Allen spectrum has a peak at 2.5–2.75 days period which is not significant in the Nawiliwili spectrum. A superinertial peak exists at 19.4 h period in both records. A second superinertial peak, or a continuation of the general increase in intertidal energy, occurs at 16.3 h period in the Nawiliwili record.

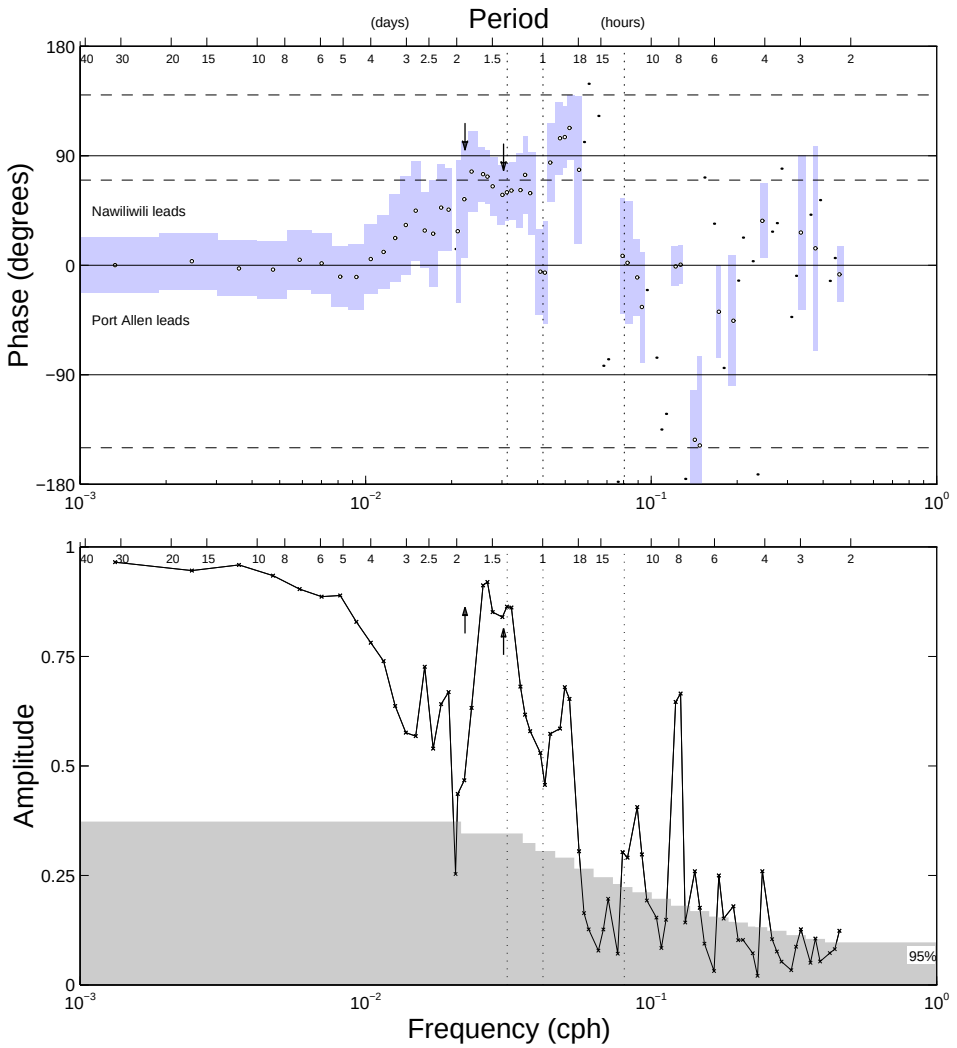

Figure 9: Coherence amplitude and phase between Nawiliwili and Port Allen adjusted sea level for the winter months of 1990–1993. Arrows indicate the theoretical period of the first (right) and second (left) baroclinic, first azimuthal trapped waves. Dashed lines in the phase plot indicate the theoretical shift of a first (70°), second (140°) and third (-150°) clockwise-propagating azimuthal wave. The coherence has an peak amplitude of 0.92 at 1.56 days period, phase 73° ± 22°. In the intertidal band, the coherence peaks at an amplitude of 0.65 at 19.3 h period, phase 113° ± 26°.

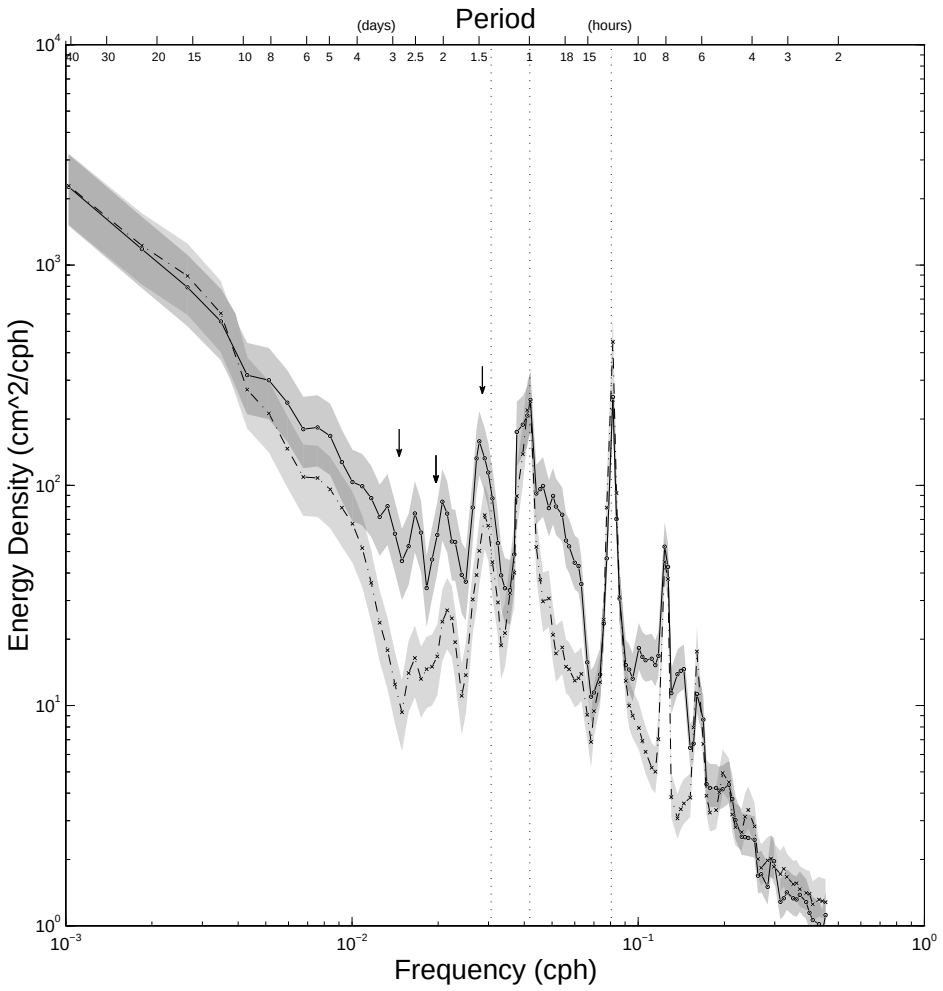

Figure 10: Adjusted sea level spectra for Honolulu (dot-dash) and Moku o Loe (solid) for the winter months of 1984–1994. The winter of 1991–1992 has not been included due to a gap in the Moku o Loe record. Arrows indicate the theoretical periods for the first (right), second (center) and third (left) baroclinic, first azimuthal trapped waves. The prominent subinertial peak in the Honolulu spectrum is at 1.44 days period (the local inertial period is 1.36 days). A secondary peak is at 1.93 days period. The Moku o Loe spectrum contains subinertial peaks at 1.48, 2.01, and 2.52 days period.

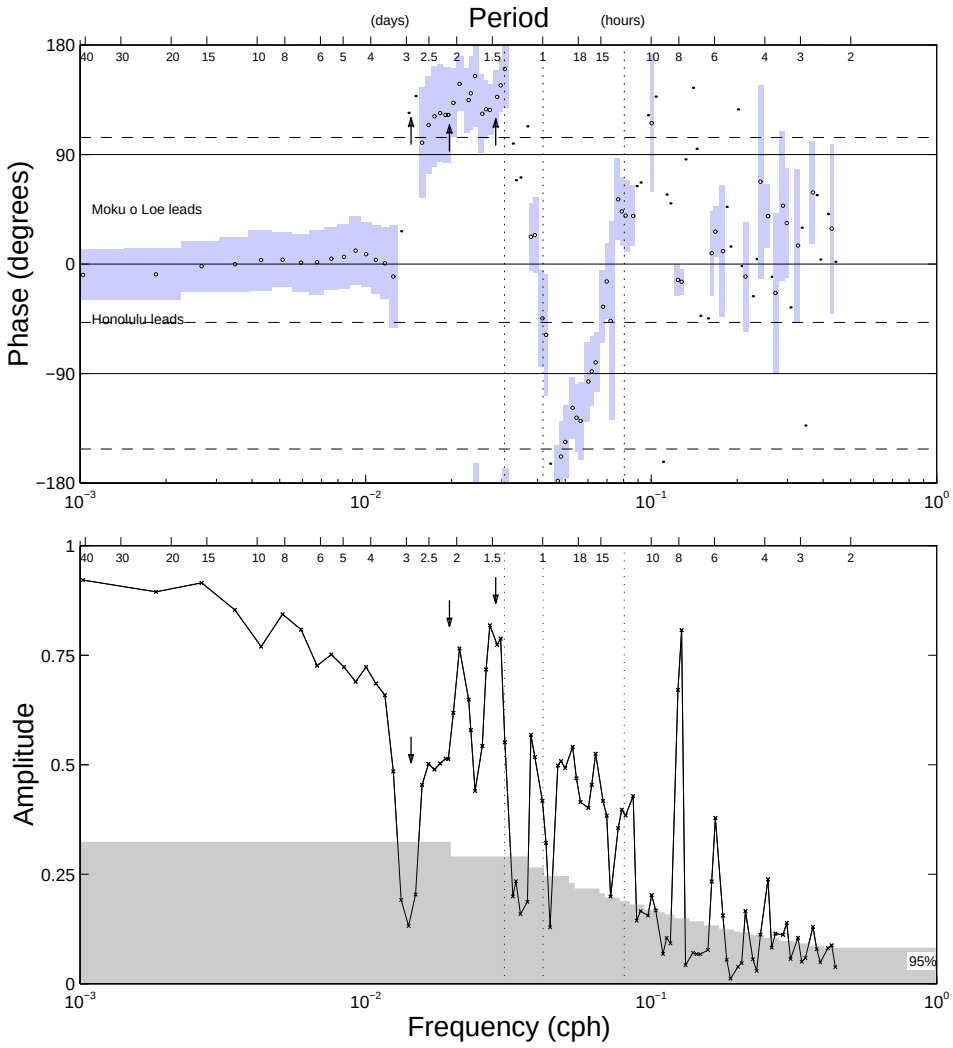

Figure 11: Coherence amplitude and phase between Honolulu and Moku o Loe adjusted sea level for the winter months of 1984–1994. Dashed lines in the phase plot indicate the theoretical shift of a first (104°), second (-152°) and third (-48°) clockwise-propagating azimuthal wave. A coherence peak of amplitude 0.82 is at 1.53 days period, phase 127° ± 21°. A peak of amplitude 0.77 is at 1.96 days period, phase 148° ± 22°. In the intertidal band, a coherence maximum of 0.54 occurs at 18.8 h period, with a phase shift of -118° ± 25°. A secondary peak at 15.6 hours period has a phase shift of -80° ± 24°.

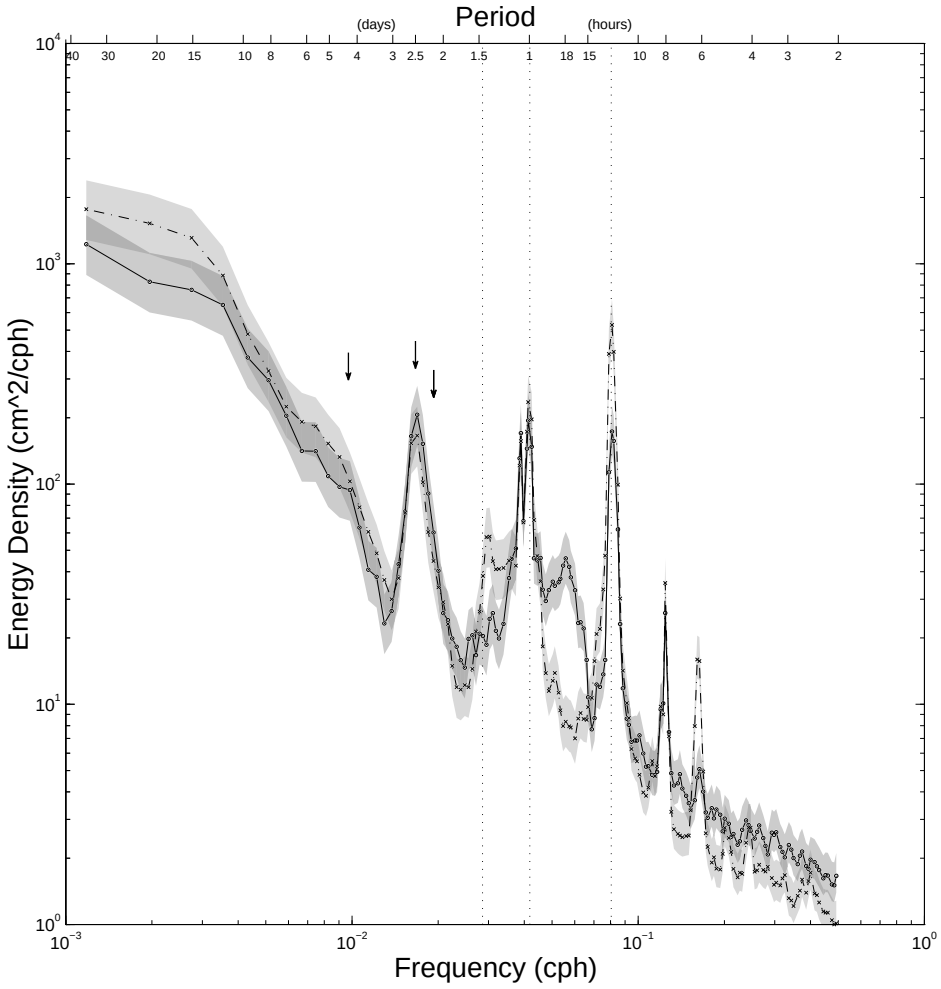

Figure 12: Adjusted sea level spectra for Hilo (solid) and Kawaihae (dot-dash) for 5 May 1990 to 20 November 1993. Due to numerous gaps in the Kawaihae record, the spectra of 24 subrecords of length 53 days were averaged to produce those appearing here. Arrows indicate the theoretical periods of the first baroclinic, first azimuthal (center) and second baroclinic, first azimuthal (left) and second azimuthal (right) trapped waves. Both spectra have an impressive subinertial peak centered at 2.47 days period, corresponding to the gravest mode island-trapped wave. The Kawaihae record has a near-inertial (superinertial) peak at 1.38 days period; an intertidal peak in the Hilo spectrum reaches its maximum at 17.9 h.

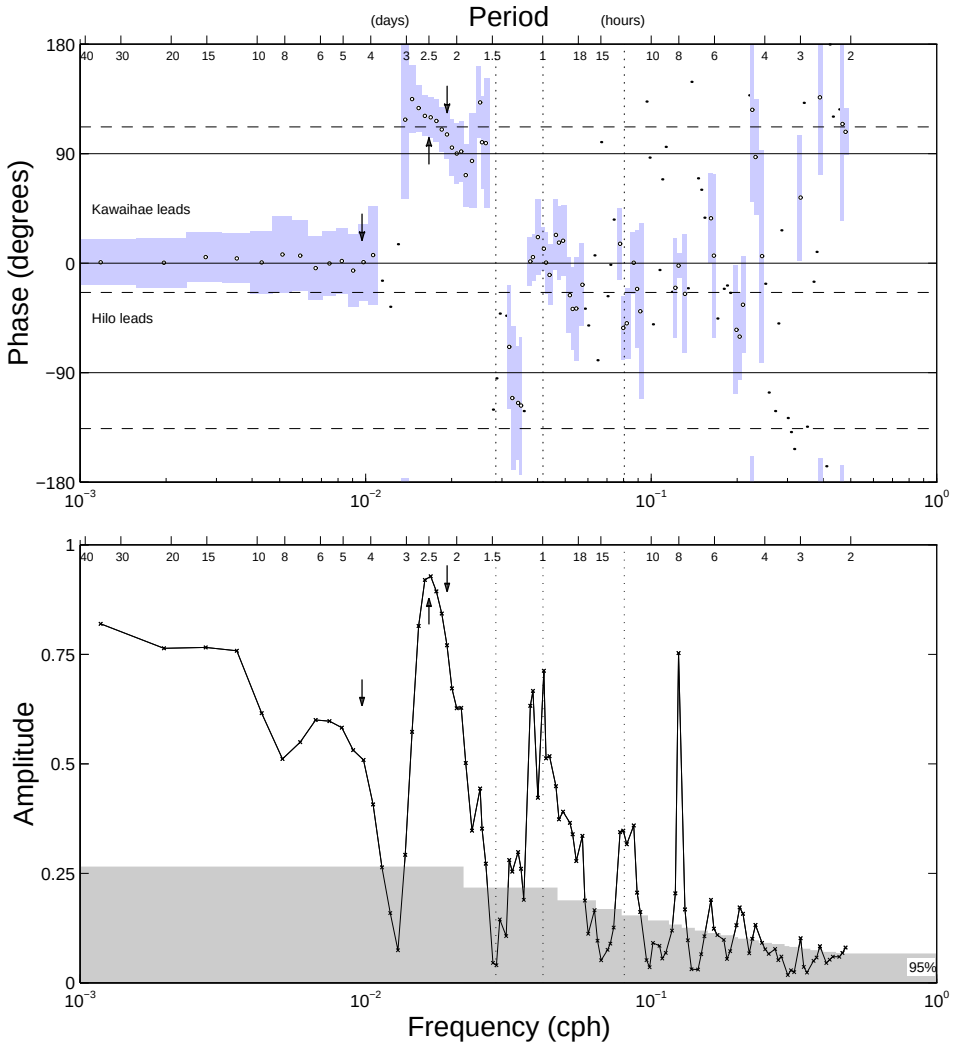

Figure 13: Coherence amplitude and phase between Hilo and Kawaihae adjusted sea level for 5 May 1990 to 20 November 1993. Dashed lines in the phase plot indicate the theoretical shift of a first (112°), second (-136°) and third (-24°) clockwise-propagating azimuthal wave. The subinertial coherence peak of amplitude 0.93 occurs at 2.47 days period, associated with a phase shift of 120° ± 17°. At 19 h period, the coherence amplitude is 0.37 with a phase of -26° ± 31°. At 17.4 h, the coherence amplitude is 0.34 with a phase shift of -18° ± 34°. The intertidal coherence falls beneath the 95% level of significance at 16.7 h period.

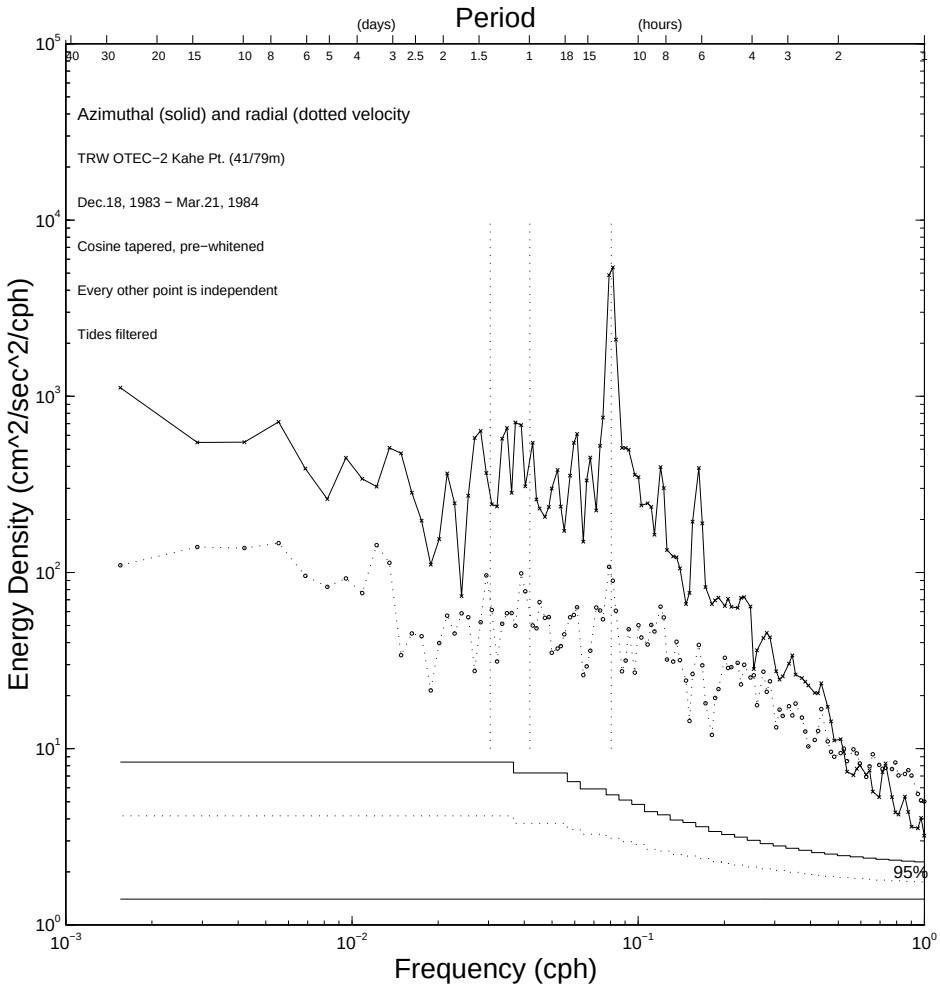

Figure 14: Spectra of the azimuthal (solid line) and radial (dotted line) currents at the TRW OTEC-2 Kahe Pt. site. The Aanderaa which obtained these records was at 41 m depth in water of total depth 79 m. Subinertial peaks in the azimuthal velocity are at 1.48 days period (corresponding to the gravest trapped wave mode), 1.94 days period, and 2.5–3 days period. Peaks in the radial velocity are at 1.41 and 2.75–3.5 days period. The local inertial period is 1.37 days.

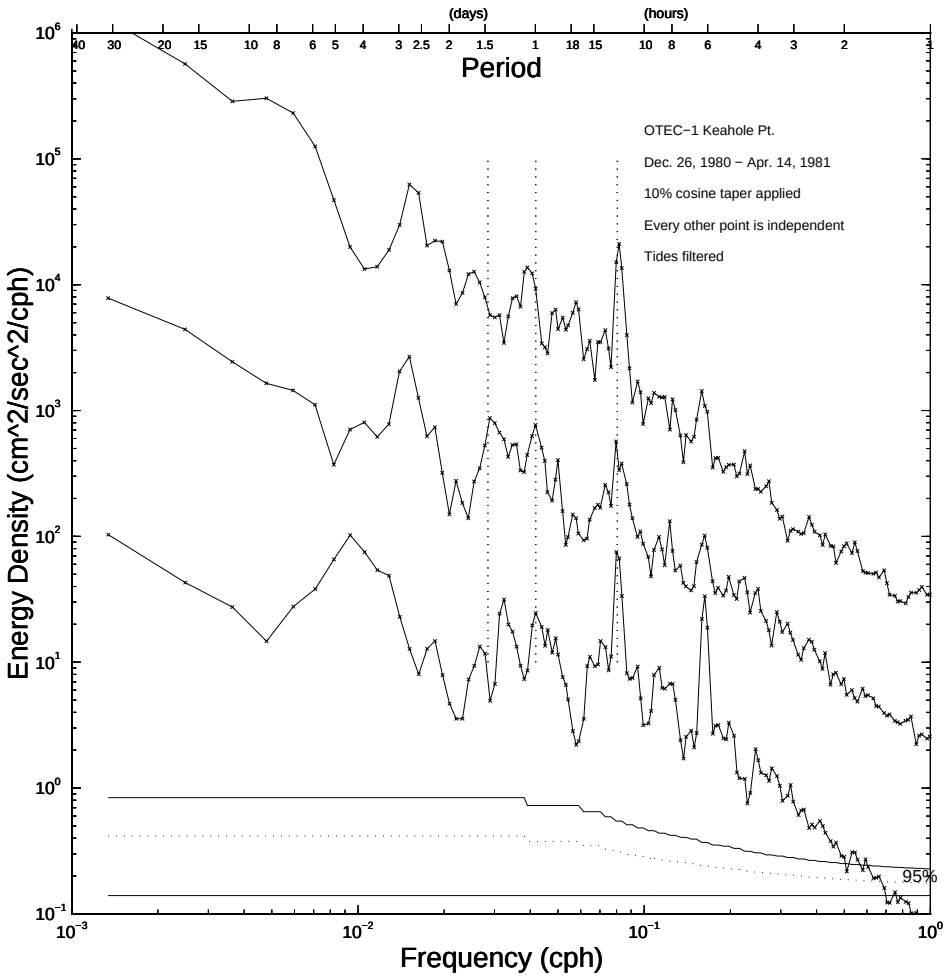

Figure 15: Azimuthal velocity spectra at the Keahole Pt. OTEC-1 site: 54 m (top), 363 m (middle) and 771 m (bottom). The 54 m/771 m spectra have been displaced up/down one decade for viewing convenience. The subinertial peaks in the 54 m spectrum are at 2.75, 2.24 and 1.64 days period. Peaks in the 363 m spectrum are at 3.96, 2.76, 2.24 and 1.89 days period. The 771 m spectrum peaks at 4.44, 2.24 and 1.56 days period.

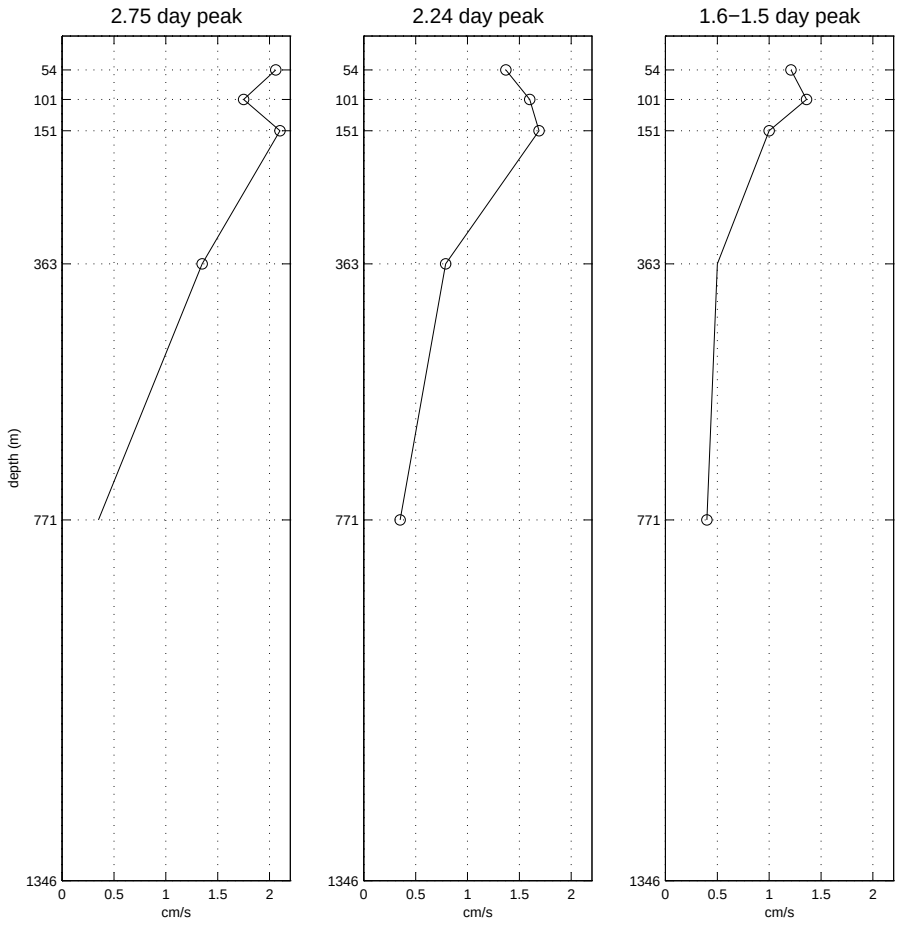

Figure 16: The vertical structure of trapped waves, derived from spectral peaks of alongshore current at the Keahole Pt. site. Circles indicate the presence of significant spectral peaks within the periods given in the titles.

Chapter 5

Superinertial oscillations

Superinertial peaks in sea level autospectra and cross-spectral coherence are examined. The peaks are not present in the current meter or subsurface temperature records. Hypotheses for the motion are examined.

5.1 Sea level observations

Luther [1985] noted energetic intertidal (17 to 20 h period) peaks in the autospectra of several sea level stations. This feature is especially prominent in the Hilo (Hawaii) spectrum, which peaks at 18 h period (see Fig. 6). Superinertial peaks may also be seen at Kahului (Maui) (Fig. 7) and Moku o Loe (Oahu) (Fig. 10).

The demodulated amplitude of the subinertial and superinertial, intertidal motion at Hilo (Fig. 17) reveals no apparent correlation between the two signals. The subinertial and superinertial peaks reach their maximum energy in different winters, suggesting that different dynamics are at work in the two frequency bands.

A significantly nonzero phase between Honolulu and Moku o Loe (both on Oahu) in the intertidal band led Luther [1985] to propose that the peaks indicate the presence of trapped waves. Coherence peaks and the accompanying phases for concurrent NODC sea level records are listed in Table 5.1.

5.1.1 Kauai

Spectra of adjusted sea level at Nawiliwili and Port Allen (Fig. 8) do not contain dramatic peaks in the intertidal band, although a slight peak at 19.4 h period is present in both records. The coherence between these time series has a peak of amplitude 0.65 at 19.3 h period (Fig. 9). The phase roughly doubles between the azimuthal mode one subinertial peak and the peak at 19.3 h period, suggesting the presence of an azimuthal mode two clockwise-propagating wave.

Table 5.1: Superinertial coherence peaks observed in sea level cross-spectra (adapted from LUTHER [1985], Table 2). Theoretical phase shifts are calculated from the separation distance of the sea level stations and the equivalent circumference of the islands (values from LUTHER [1985]).

	INERTIAL	PERIOD OF	OBSERVED		THEORETICAL CW[2]		
	PERIOD	COHERENCE	COHERENCE[1]		AZIMUTHAL MODES:		
ISLAND	(hours)	PEAK (hours)	AMP.	PHASE	$m = 1$	$m = 2$	$m = 3$
Kauai	31.9	19.3	0.6	113° ± 26°	70°	140°	-150°
Oahu	32.6	18.8	0.5	-118° ± 25°	104°	-152°	-48°
		15.6	0.5	-80° ± 24°	104°	-152°	-48°
Hawaii	36.0	19.0	0.4	-26° ± 31°	112°	-136°	-24°
		17.4	0.3	-18° ± 34°	112°	-136°	-24°

(1) Station pairs for each island are given in Table 2.1.

(2) The sign of the phase shift is opposite for a counter-clockwise mode.

5.1.2 Oahu

LUTHER [1985] noted evidence of a trapped wave of period 17 to 20 h at Oahu, with a phase shift indicating a low azimuthal mode structure. Spectra of the NODC data (Figs. 10, 11) are consistent with this interpretation.

Rather than an isolated intertidal peak in the Moku o Loe spectrum, there is elevated energy across the intertidal band. Furthermore, there is not a significant peak in the intertidal band of the Honolulu spectrum. However, a band of significant coherence between Honolulu and Moku o Loe, associated with a nonzero phase shift, suggests the presence of a propagating signal in both records. This phase shift is consistent with a mode one counter-clockwise propagating structure [LUTHER, 1985], although there is no clear dynamical reason to anticipate the presence of such a wave.

5.1.3 Hawaii

Hilo and Kawaihae sea level spectra (Fig. 12) appear qualitatively similar to those of Honolulu and Moku o Loe in the intertidal band; in all four records, there is little energy

at the leeward stations and elevated energy at the windward stations. However, the phase between the Hawaii stations (Fig. 13) does not have an intertidal coherence peak with a significantly nonzero phase. Hilo and Kawaihae ASL is coherent from the diurnal to 16.7 h period. Within this band, the coherence amplitude drops from a maximum of 0.5 at the diurnal period. The phase is relatively steady at $\approx$ -20° $\pm$ 30° (averaging from 17.6 to 21.0 h period produces a phase of -17° $\pm$ 20° with an amplitude of 0.28). This phase difference may result from an azimuthal mode three clockwise-propagating wave (see Table 5.1).

5.2 Currents in the intertidal band

An examination of current and temperature spectra at the Kahe Pt., Alenuihaha Channel, DUMAND and Lanai sites did not reveal any significant intertidal peaks. Only at one site, discussed below, did a spectrum strongly differ from the GM shape between the tidal peaks.

The spectrogram for the azimuthal current of the 54 m Aanderaa at the OTEC-1 Keahole Pt. mooring (Fig. 18) reveals an intensification of energy at 18 h period between days 80 to 85 of the record (time measured from beginning of data acquisition, 26 December 1980, 14:07 HST). A spectrum of this time series from days 70 to 109 has a sharp peak at 18 h period (Fig. 19). This peak also appears in the azimuthal velocity spectrum of the 101 m instrument, although it is much weaker. The deeper instruments of the mooring do not have significant intertidal peaks. The spectrum of temperature fluctuations at the 54 m instrument does not contain a significant intertidal peak.

As will be shown in Appendix A, the Keahole Point 54 m Aanderaa measured a counterclockwise to clockwise energy ratio in excess of that expected for free internal waves in the 15–17 h period band. However, the CCW to CW energy ratio of the record

from days 70 to 109 does not significantly differ from that of the entire record. Thus, the energy ratio anomaly is not solely associated with the event discussed here.

There was no significant peak in Hilo sea level in the intertidal band during days 70–109 of the Keahole record. Instead, the demodulated amplitude of Hilo sea level in this band peaks at days 50–60. The spectrum of the Hilo sea level collected during this time (not shown) has peaks at 17 and 19 h period, with a minimum at 18 h. The coherence between Hilo sea level and Keahole Point azimuthal velocity reaches maximum amplitudes of 0.7 at 19.5 and 15 h period for the entire record; coherence in the intertidal band falls below the 95% confidence level for days 70–109. Thus, there appears to be no relationship between this 18 h current peak and the intertidal sea level peak which is so energetic in the Hilo record.

5.3 Possible explanations

For the subinertial oscillations, it was shown that energetic peaks existed in the sea level spectra of station pairs on several islands. These autospectral peaks corresponded to coherence peaks with significantly nonzero phase. Combined with a dynamical model which predicts the observed peaks and the phase shift between the stations, the trapped wave interpretation is solidly supported. Observations of subinertial trapped waves in currents demonstrated that the baroclinic waves can reach appreciable magnitudes.

In the intertidal band, some observations suggest the presence of trapped waves. However, it is not clear that the coherence peaks and phase shifts observed in the concurrent sea level records correspond with the intertidal autospectral peaks. Although the Hilo ASL spectrum has a relatively sharp peak at 17.9 h period, the coherence between Hilo and Kawaihae falls from a maximum at the diurnal period to the 95% level of no significance at 16.7 h period. Nothing distinguishes 18 h within this band.

Furthermore, the intertidal energy gap in the leeward stations (Honolulu, Kawaihae) is puzzling in the context of an island-trapped interpretation. While the energy level of the subinertial trapped waves in the Honolulu spectrum is lower than that of the Moku o Loe spectrum (Fig. 10), the signature of the gravest mode is clear in both spectra.

LUTHER [1985] noted that there was significant coherence between Hilo (Hawaii) and Honolulu (Oahu) sea level at 16–20 h period. This led him to suggest that a resonant mode around Hawaii may be leaking energy across the island chain. However, the coherence between Hilo and Nawiliwili (Kauai) ASL is significant from the diurnal to 16 h period, with a peak amplitude of 0.6 at 19.9 h (Fig. 20). The phase of this signal is $44^\circ \pm 20^\circ$ (Hilo leads). Unless the trapping scale of the waves is very large, leakage cannot explain this coherence peak. The Kauai Channel separates Kauai from Oahu by a horizontal distance of 115 km, reaching depths in excess of 3 km.

What physical phenomenon is causing the 17–20 hour peaks in the sea level spectra and the coherence peaks in the cross-spectra? A number of possibilities merit consideration and are discussed here. While no definite conclusions can be made without further study, some previously considered explanations for the intertidal peak may be reevaluated in light of the work presented in Chapter 2. The observed features of the intertidal peaks are:

- Sea level autospectral peaks at 17–20 h period,
- No corresponding peaks in current spectra,
- No significant coherence with the local winds in the intertidal band [LUTHER, 1985],
- Phase consistent with a low azimuthal mode structure at Kauai and Oahu,
- No evidence of phase propagation around Hawaii (or possibly a mode three structure),
- Significant coherence between Hilo and Nawiliwili at 16–24 h period, with a peak at 19.9 h.

A minimum criterion for any model of the intertidal motion is that it explains the presence of sea surface displacements without corresponding velocity fluctuations at the locations examined here.

5.3.1 "Trapped-leaky" refraction

LUTHER [1985] discussed superinertial waves nearly trapped to a steeply-sloping island flank by refraction. Waves of this sort would have extremely short alongshore wavelengths for the Hawaiian Islands. Furthermore, their resonant frequencies are a strong function of the geometry and slope of the island. Because of the varying geometries of the islands and the suggestion of a low azimuthal wavenumber at Oahu, LUTHER [1985] did not feel that refraction could yield results consistent with the observations.

5.3.2 Seiche eigenfrequency of a harbor

Hilo and Kawaihae are coherent in the intertidal band, although weakly so. Could a large-scale background signal be producing the coherence (amplitude ≈ 0.5 at 20 h), while a phenomenon localized to Hilo creates the 18 h autospectral peak? A possible source of this peak is seiche resonance within Hilo harbor.

Hilo harbor is an L-shaped channel of depth 12 m and length (from the right-angle turn to the end) of approximately 3.5 km. The lowest eigenfrequency of the harbor will have a period of order

$$O\left(\frac{2 \cdot 3.5 \times 10^3 \text{ m}}{\sqrt{9.81 \text{ m/s}^2 \cdot 12 \text{ m}}}\right) \approx 11 \text{ minutes.} \tag{5.1}$$

This period is orders of magnitude away from that of the intertidal peak. Sampling this signal at one hour intervals could produce an aliased peak in the intertidal range, but the energy of the seiche motion would have to be quite large for this to be an important effect.

5.3.3 Harmonics of lower frequency motion

There are no harmonics of the diurnal or semidiurnal tides falling in the intertidal band. However, the first harmonic of inertial or near-inertial motion would fall at 17–18 h period. The lack of significant coherence with the local winds at intertidal frequencies is consistent with the intertidal peak being a harmonic of lower-frequency motion.

A complex demodulation of the near-inertial and intertidal signals at Moku o Loe (Oahu) and Hilo (Hawaii) does not reveal a strong visual correlation between peaks in the inertial and intertidal bands (Fig. 21). A seasonal signal is seen in both signals at Moku o Loe (where the near-inertial band encompasses the gravest subinertial Oahu trapped wave), but maxima occur in different winters. As was the case at Hawaii (see Fig. 17), the sub- and superinertial peaks appear to be unrelated. At Hilo, there is only weak activity in the near-inertial band (see Fig. 12); what near-inertial peaks exist in the demodulated signal do not seem to correspond to the intertidal peaks.

However, it is not clear that near-inertial baroclinic motion would produce appreciable sea level displacements. Perhaps understanding the nature of the near-inertial, superinertial peak in the Kawaihae spectrum (Fig. 12) may give insight on the dynamics of the intertidal oscillations.

5.3.4 Pseudo-resonant scattering of the internal wave field

The pseudo-resonant scattering phenomenon described by WUNSCH [1972] predicts near-inertial spectral peaks composed of a mix of higher azimuthal modes. As discussed by LUTHER [1985], such a mix of modes would not produce the high coherence amplitudes and nonzero phase shifts of the intertidal signals seen at Oahu and Kauai. Furthermore, the pseudo-resonant peaks shown in Fig. 4 do not occur at the nondimensional frequency $\omega/f_o \approx 2$ (appropriate for an 18 h peak at Hawaii) up to values of ε corresponding to

very high baroclinic modes. Thus, pseudo-resonance is not believed to offer an adequate explanation of the observations.

5.3.5 Von Karman vortex forcing

A well-known feature of large Reynolds number flow past a cylindrical obstacle is the formation and shedding of counter-rotating vortices in the lee of the cylinder. The characteristic frequency of these von Karman vortices is given by the empirical law

$$\frac{\omega}{2\pi} = S_t \frac{U_\infty}{a}, \tag{5.2}$$

where the Strouhdal number S_t is approximately 0.21 for a large range of Reynolds numbers, U_∞ is the upstream velocity of the flow, and a is the radius of the cylinder [KUNDU, 1990].

In Fig. 22, a dramatic example of these vortices is seen in the lee of Kauai in an AVHRR image from 8 February 1995. The wind at the time was from the north at 5 to 10 mph ($\approx$2.25–4.5 m/s), yielding vortices of period

$$\frac{2\pi}{\omega} \approx \frac{25 \times 10^3 \text{ m}}{0.21 \cdot (2.25 - 4.5) \text{ m/s}} \approx 15 - 7.5 \text{ hours}. \tag{5.3}$$

Thus, the pressure fluctuations associated with the vortices should force motion with a characteristic period not significantly below the observed intertidal peak.

Could forcing of this nature excite superinertial motion along the leeward side of Kauai, yielding a clockwise-propagating azimuthal mode two wave? A major shortcoming of this hypothesis is the broad-band nature of the forcing: because the von Karman period depends on both the wind speed and the island radius, it is hard to imagine this phenomenon producing the tight coherence peak observed between Nawiliwili and Port Allen. The correction to sea level for isostatic pressure at Lihue (Kauai) in the winter months of 1984–1994 (Fig. 23) does not have a significant spectral peak in the intertidal band.

5.3.6 Pacific basin eigenmode

The high coherence between Hilo (Hawaii) and Nawiliwili (Kauai) at 20 h period (Fig. 20) suggests that at least part of the intertidal signal may be composed of motion with a scale much larger than the trapped waves composing the focus of this study. Large-scale sea level displacements would have weak horizontal gradients, perhaps explaining the lack of intertidal peaks in current spectra. Furthermore, one would not expect significant coherence between a large-scale phenomenon and the local weather.

In their numerical study of oceanic normal modes, PLATZMAN *et al.* [1981] identified several basin-scale gravity modes with periods in the intertidal band. Of particular interest for the present discussion is their Mode 19 "Pacific wave," with a natural period of 21.2 h and maximum amplitudes extending from the northwest coast of North America into the central Pacific (a map of this mode appears in Fig. 17 of PLATZMAN *et al.*, [1981]).

A line of constant phase for the Mode 19 wave runs roughly parallel to the Hawaiian Island chain as it proceeds cyclonically around an amphidrome at $\approx 30^\circ$ N, 160° E. Thus, the nonzero phase shifts observed at the Kauai and Oahu stations are inconsistent with this hypothesis. Furthermore, the difference in energy levels between closely-spaced sea level stations (such as Moku o Loe and Honolulu) suggests motion of small scale.

Sea level at Midway Island and Johnston Atoll are not significantly coherent with Hilo sea level in the intertidal band, although the demodulated amplitude of 20 h motion at these stations (Fig. 24) suggests that large-scale processes may determine the amount of energy within this band. It is conceivable that excitation of a slightly-damped Pacific basin-scale mode may be adding a weak but coherent signal to the data. Superimposed upon this motion may be truly trapped waves (as suggested by the Oahu and Kauai phases).

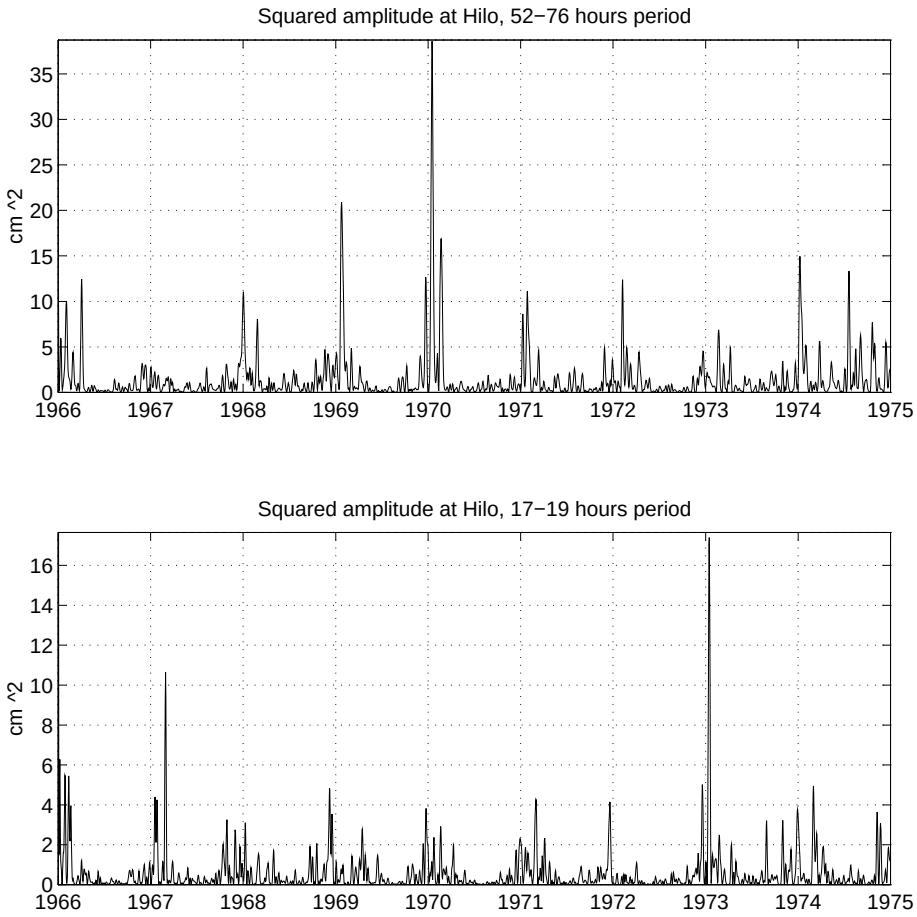

Figure 17: Squared amplitude of adjusted sea level at Hilo, 1966-1974. The complex demodulation used a 5-point Butterworth IIR filter with a cutoff frequency yielding the equivalent bandpasses given in the titles.

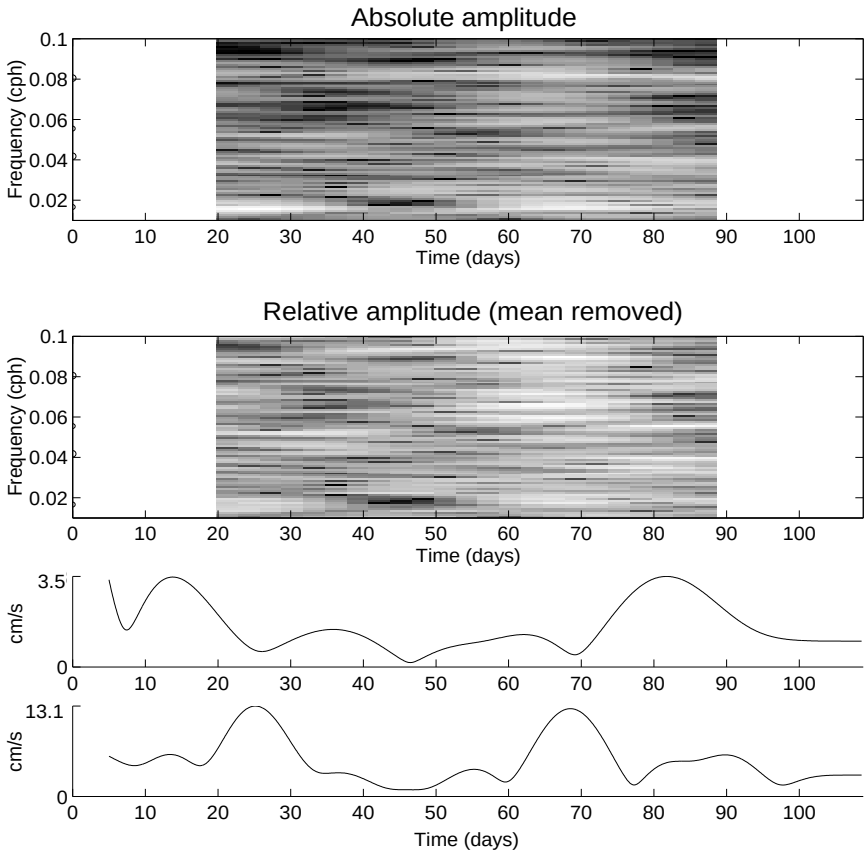

Figure 18: Spectrograms of the azimuthal velocity at the Keahole Pt. OTEC-1 site (54 m depth). Top spectrogram is the absolute velocity; bottom is the relative change within each frequency bin. Larger amplitudes are lighter in shading. Large circles on the frequency axis mark the M_2 and K_1 frequencies; smaller circles mark 1/18 and 1/60 cph. Beneath the spectrograms, the amplitude of the 18 h (top) and 2.50 days (bottom) motion is shown. The complex demodulation used for these calculations employed a 5-point Butterworth IIR lowpass filter; the lowpass cutoff was chosen such that the equivalent bandpass is from 17.6–18.6 h period (top) and 2.17–2.88 days period (bottom). The beginning of day 0 corresponds to 26 December 1980, 14:07 HST (time as given by Noda and Associates).

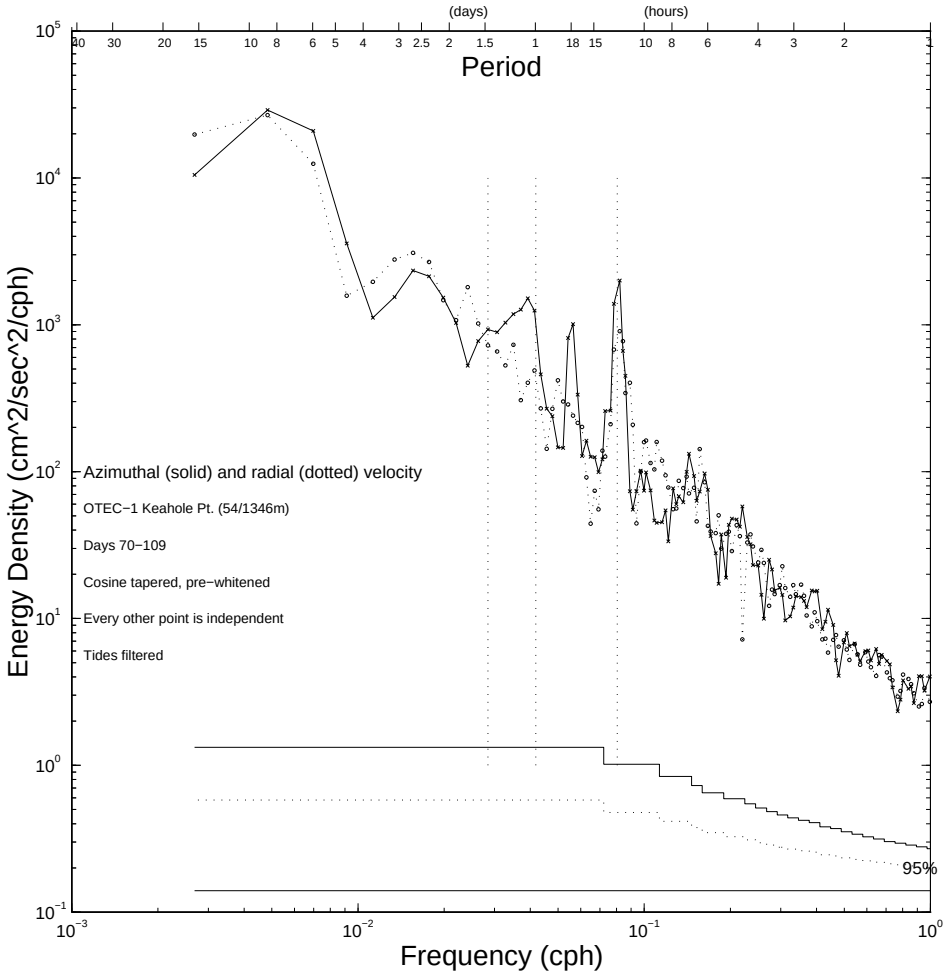

Figure 19: Spectra of the azimuthal (solid) and radial (dotted) velocity at the Keahole Point OTEC-1 mooring (54 m depth) for days 70-109 of the time series. A significant intertidal peak is at 18.1 h period in the azimuthal velocity.

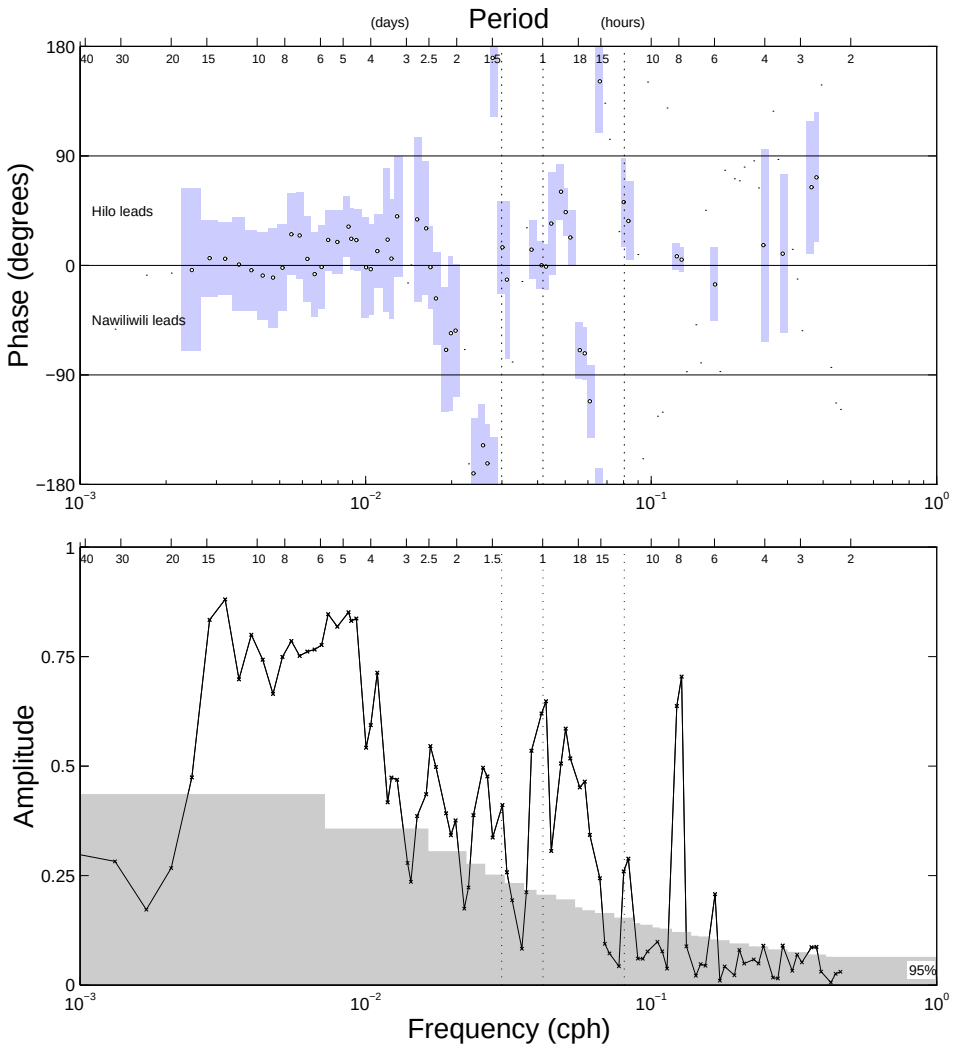

Figure 20: Coherence amplitude and phase between Hilo (Hawaii) and Nawiliwili (Kauai) adjusted sea level for the winter months of 1984-1994. The intertidal coherence peak has a maximum amplitude of 0.59 at 19.9 h period, phase 44° ± 20° (Hilo leads). Subinertial coherence peaks of amplitude 0.55 and 0.50 are at 2.47 and 1.62 days period, with phase shifts of -1° ± 34° and -148° ± 34°, respectively.

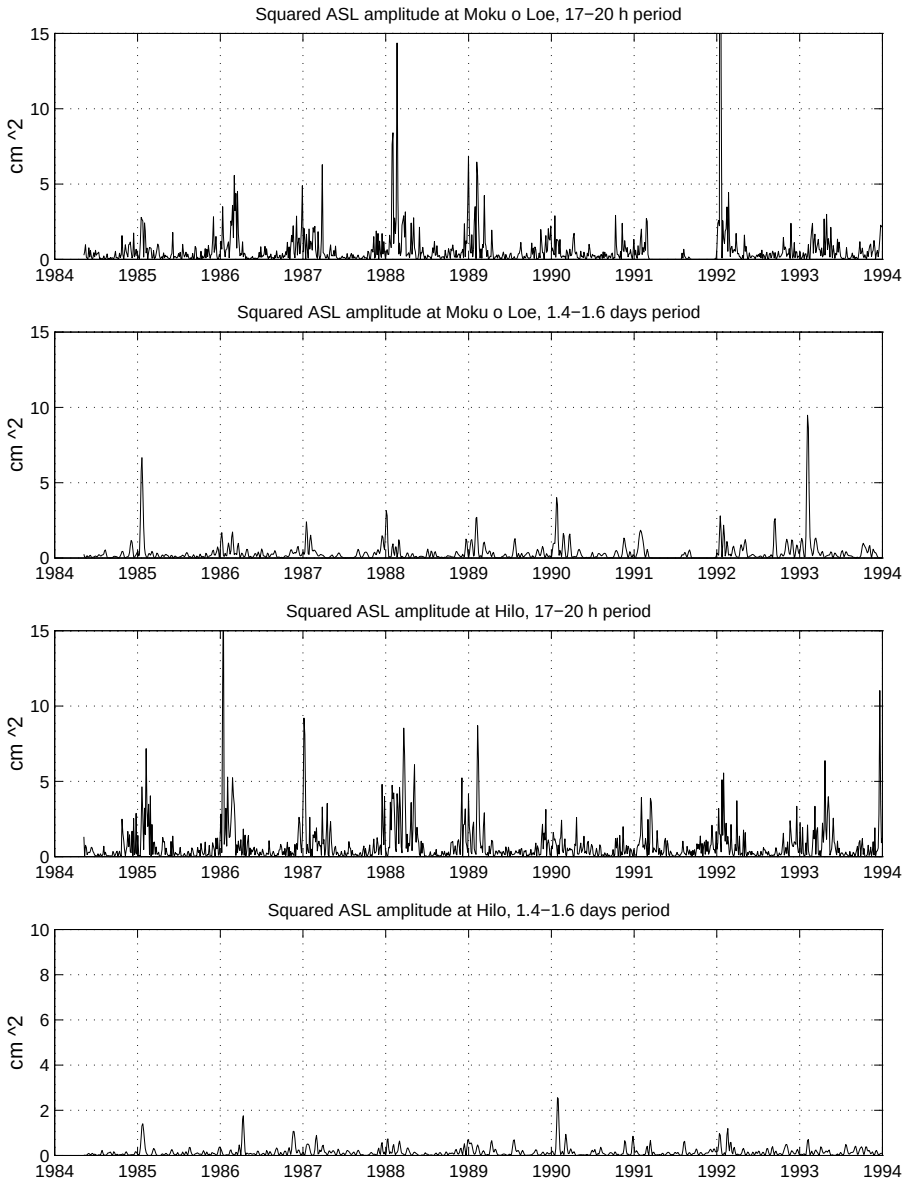

Figure 21: Squared amplitude of the near-inertial and intertidal signals at Moku o Loe (Oahu) and Hilo (Hawaii).

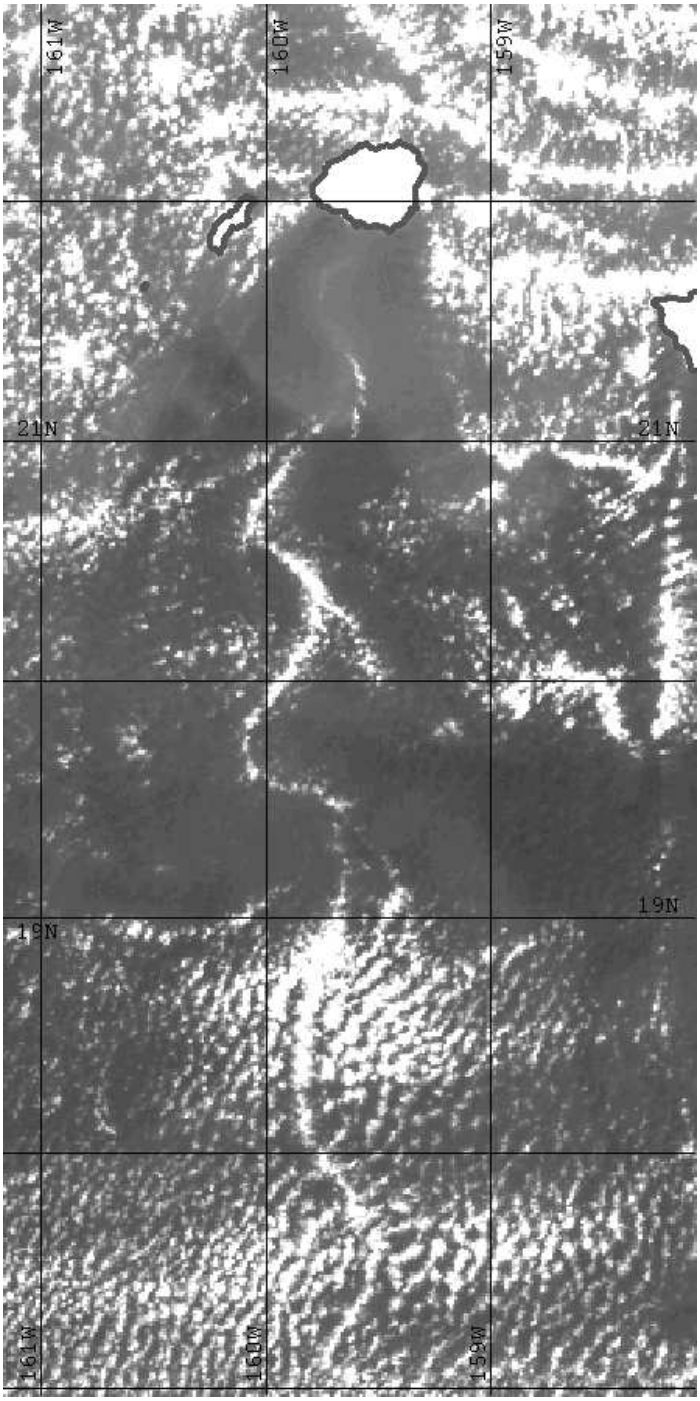

Figure 22: A von Karman vortex street in the lee of Kauai. AVHRR thermal infrared image from 8 February 1995.

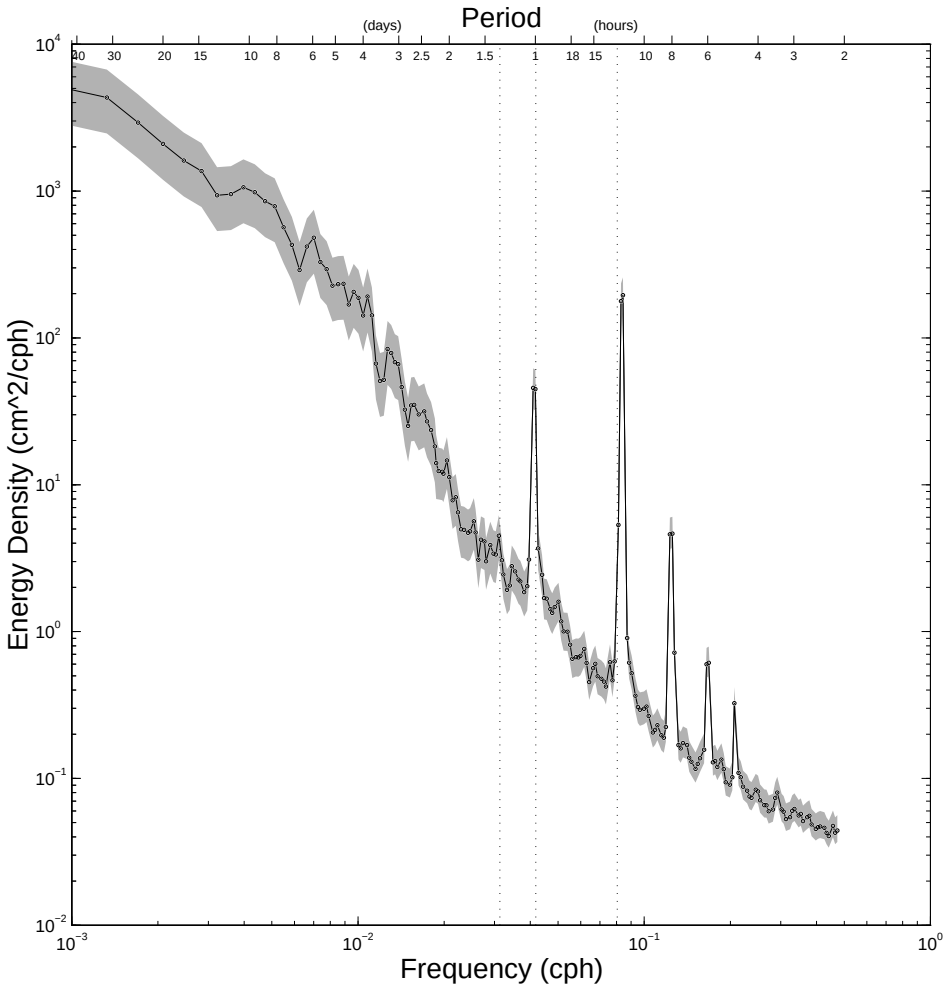

Figure 23: Spectrum of correction to sea level for isostatic air pressure forcing at Lihue (Kauai) for the winter months of 1984–1994.

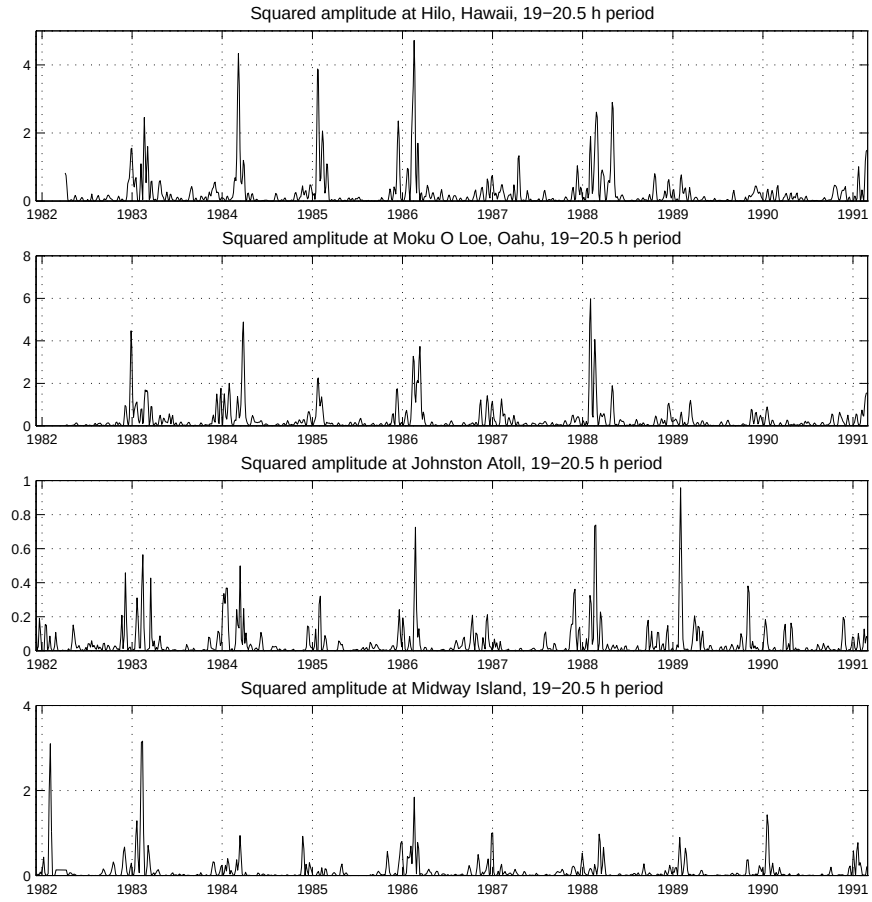

Figure 24: Sea level energy at Hilo (Hawaii, top), Moku o Loe (Oahu, second from top), Johnston Atoll (second from bottom) and Midway Island (bottom). The complex demodulation used a lowpass filter with an equivalent bandpass of 19 to 20.5 h period. Similar time series of squared amplitude from 14 to 18.5 h have been subtracted from each record, resulting in arbitrary units on the y-axes.

Chapter 6

Forcing mechanisms

A directly wind-forced trapped wave model is examined. The model's output is shown to be of the same order as observed trapped waves, although differences in the balance of kinetic and potential energy are noted. Evidence of trapped-wave leakage from Hawaii to Maui is demonstrated in a multiple regression analysis of Kahului sea level onto Hilo sea level and the local winds at Kahului.

6.1 Direct wind forcing of island-trapped waves

Subinertial peaks in temperature [Wunsch, 1972], current [Hogg, 1980] and sea level spectra [Luther, 1985] indicate that trapped waves represent a significant part of the motion near islands. Several mechanisms for generating these waves have been suggested, including direct wind forcing [Hogg, 1980] and transfer of energy from remote wind forcing via surface waves [Luther, 1985].

There is considerable evidence that direct atmospheric forcing plays a significant role in resonant coastal wave excitation. Hogg [1980] identified a 26.1 h peak in current and temperature spectra as Bermuda's gravest subinertial trapped wave. At this period, he found a coherence peak of amplitude 0.65, accompanied by a 180° phase jump, between temperature at 700 m depth and north surface wind stress. Miyata and Groves [1971] noted a prominent 2.5 day peak in Hilo, Hawaii sea level – later identified by Luther [1985] as Hawaii's gravest subinertial trapped wave – and found it was coherent with both local and distant weather. Luther [1985] also found weak coherence between Hilo sea level and meridional wind in this band; however, he noted that a large phase jump accompanied the coherence peak and suggested that the inverse barometer effect from air pressure forcing may be contaminating the signal (for adjusted sea level, a larger coherence amplitude is found: see Fig. 25).

It has been proposed [LUTHER, 1985] that an effective mechanism for island-trapped wave generation would be a spatially homogeneous wind blowing over an island, oscillating at or near a trapped wave eigenfrequency. This would produce a pattern of Ekman-driven convergence and divergence appropriate for the excitation of odd azimuthal modes trapped waves. In order to explore the possibility that such direct forcing may play an active role in generating observed coastal waves, this model is developed and examined here. The focus of this work is to explore the order-of-magnitude trapped wave response for a simple cylindrical island rather than an in-depth examination of the vertical structure and exact eigenfrequencies for an actual island. Future modeling, possibly executed as an extension of numerical studies of seamount-trapped waves [BRINK, 1989; BRINK, 1990], should deal with these issues and be compared to existing data sets in the spirit of NOBLE, BRINK AND ERIKSEN [1994].

6.1.1 Formulation of the model

The relevant governing equations for examining island-trapped waves are the Boussinesq, hydrostatic, linearized momentum and continuity equations on an f-plane. A length scale independent linear dissipation (Rayleigh damping) may be assumed of time scale μ^{-1}, where $\mu/f_o \ll 1$:

$$(\partial_t + \mu)u_\alpha - f_o \varepsilon_{\alpha\beta} u_\beta + \partial_\alpha p = F_\alpha, \tag{6.1a}$$

$$N^2 \eta + \partial_3 p = 0, \tag{6.1b}$$

$$(\partial_t + \mu)\eta - u_3 = 0, \tag{6.1c}$$

$$\partial_\alpha u_\alpha + \partial_3 u_3 = 0. \tag{6.1d}$$

Greek subscripts represent components in the horizontal directions x_1 and x_2. Summation convention is implied for all vector indices. The vector $\boldsymbol{u}$ is the velocity of the fluid. The perturbation pressure p describes deviations from the background hydrostatic

balance. The vertical displacement of a fluid particle from a state of rest is described by η. The buoyancy and inertial frequencies are N and f_o, respectively.

Wind forcing is parameterized as a horizontally homogeneous body force acting in the north-south direction on a thin surface layer of width h_{mix} [GILL AND CLARKE, 1974]. One Fourier component of frequency ω will be dealt with explicitly:

$$F_1 = 0, \qquad F_2 = \begin{cases} \frac{\tau_o}{\rho_o h_{mix}} \, \mathrm{e}^{-i\omega t}, & -h_{mix} \leq x_3 \leq 0, \\ 0, & -h_0 \leq x_3 < -h_{mix}. \end{cases} \tag{6.2}$$

A more general wind field may be constructed by integrating over a wind spectrum $\tau_o(\omega)$; the goal of this analysis is simply to observe the response of the system as a function of forcing frequency.

The total depth h_0 is assumed to be constant. Because the motion of interest is the baroclinic response to this forcing in the presence of an island [WUNSCH, 1972], the depth average of $\boldsymbol{F}$ is neglected. Barotropic subinertial resonant frequencies for the Hawaiian Islands are indistinguishable from the inertial [LONGUET-HIGGINS, 1969] and substantially alter the response only if $\omega/f_o \approx 1$. Assuming a rigid lid and flat bottom, the vertical boundary conditions are

$$u_3 = 0 \quad \text{at} \quad x_3 = 0, -h_0. \tag{6.3}$$

A cylindrical island of radius a, centered at $r = 0$ and extending from the bottom to the rigid lid, imposes the boundary condition

$$u_r = 0 \quad \text{at} \quad r = a, \tag{6.4}$$

where u_r is the radial component of the velocity. The velocity and perturbation pressure fields must also satisfy

$$\boldsymbol{u}, p \text{ remain finite as } r \to \infty \tag{6.5}$$

if the motion is trapped, or outward-radiating energy only as $r \to \infty$ if the motion is freely-propagating.

Before proceeding, three geometrical approximations for the island merit some discussion. The first involves mapping the coastline of an actual island onto a cylinder of some "equivalent" radius. LUTHER [1985] argued that this approximation may be justified for subinertial Kelvin-like waves on the grounds that the net ray path is not effected by random irregularities smaller than the deformation radius; larger asymmetries must be mapped onto the equivalent radius to produce a ray path of similar length.

The second geometrical approximation made here is that the island walls are purely vertical. Retention of vertical separability motivates this approximation, which may justified for the baroclinic modes with deformation radii much larger than the horizontal scale of the island shelf [LUTHER, 1985]. If these scales are comparable, the motion will feel the slope and resemble the low-frequency shelf waves of RHINES [1970]. Consequently, the penetration scales of the higher modes will be unrealistically large in this model. The radial structure of these higher modes may actually resemble those found by BRINK [1989] in his numerical study of seamount-trapped waves.

The third approximation made in this model is that the wind stress is spatially homogeneous. Large topographic features, such as Mauna Kea and Mauna Loa on the island of Hawaii, disrupt the spatial homogeneity of the wind field and produce shear zones in the lee of the island, essentially increasing the area of convergence/divergence regions and possibly magnifying trapped wave generation. Furthermore, winds encountering an island with significant vertical relief would be intensified around the sides of the island, thus increasing the magnitude of the Ekman pumping [LUTHER, 1985].

Under the approximations described above, the vertical dependence may be separated by assuming

$$\begin{pmatrix} u_1 \\ u_2 \\ p \\ F_2 \end{pmatrix} = \sum_n \begin{pmatrix} \hat{U}_1 \\ \hat{U}_2 \\ P \\ T \end{pmatrix} (x_1, x_2; n)\ \mathrm{e}^{-i\omega t}\ \phi(x_3; n), \tag{6.6a}$$

$$\begin{pmatrix} u_3 \\ \eta \end{pmatrix} = \sum_n \begin{pmatrix} U_3 \\ E \end{pmatrix} (x_1, x_2; n)\ \mathrm{e}^{-i\omega t}\ \varphi(x_3; n) \tag{6.6b}$$

[FJELDSTAD, 1933]. The separation constant is formulated in terms of the equivalent depth:

$$\tfrac{\mathrm{d}}{\mathrm{d}x_3}\left(\tfrac{1}{N^2}\tfrac{\mathrm{d}}{\mathrm{d}x_3}\phi_n\right) + \tfrac{1}{gh_n}\phi_n = 0, \tag{6.7a}$$

$$\tfrac{\mathrm{d}}{\mathrm{d}x_3}\phi_n = 0 \quad \text{at} \quad x_3 = 0, -h_0, \tag{6.7b}$$

$$(-i\omega + \mu)P + gh_n\ \partial_\alpha \hat{U}_\alpha = 0. \tag{6.8}$$

The vertical structure functions are related according to

$$\varphi_n \propto \frac{\mathrm{d}}{\mathrm{d}x_3}\phi_n. \tag{6.9}$$

Assuming a constant buoyancy frequency N_o, the solutions to (6.7a) satisfying the vertical boundary conditions are

$$\phi_n = \cos\left(n\pi\frac{x_3}{h_0}\right), \tag{6.10}$$

with equivalent depths for $n \geq 1$ given by

$$h_n = \frac{1}{g}\left(\frac{N_o h_0}{n\pi}\right)^2. \tag{6.11}$$

The forcing projects onto these modes such that

$$T_n = \tfrac{2\tau_o}{\rho_o h_0}\ \mathrm{sinc}\left(n\pi\tfrac{h_{mix}}{h_0}\right). \tag{6.12}$$

For $N_o = 2.99 \times 10^{-3}$ s^{-1}, $f_o = 4.88 \times 10^{-5}$ s^{-1} and $h_0 = 3.0 \times 10^3$ m, one finds that $h_n = .83n^{-2}$ m and mode $n = 6$ has a radius of adjustment smaller than 10 km. Because this is approximately the width of the island flank for Hawaii, only the lowest few baroclinic modes should feel the actual island as vertically-walled.

For each vertical mode (dropping the subscript n),

$$\begin{aligned}(-i\omega+\mu)\hat{U}_1 - f_o\hat{U}_2 + \partial_1 P &= 0, &(6.13a)\\ (-i\omega+\mu)\hat{U}_2 + f_o\hat{U}_1 + \partial_2 P &= T, &(6.13b)\\ (-i\omega+\mu)P + gh\partial_\alpha\hat{U}_\alpha &= 0. &(6.13c)\end{aligned}$$

Assume

$$\hat{U}_\alpha = \overline{U}_\alpha(n) + U_\alpha(x_1, x_2; n), \tag{6.14}$$

where the barred components of the velocity represent the horizontally homogeneous forced solution in the absence of the island (the "far-field," BRINK [1990]) and U_1, U_2 are the island-associated parts of the velocity field which act to satisfy the boundary condition at $r = a$. By definition,

$$\begin{aligned}(-i\omega+\mu)\,\overline{U}_1 - f_o\overline{U}_2 &= 0, &(6.15a)\\ (-i\omega+\mu)\,\overline{U}_2 + f_o\overline{U}_1 &= T. &(6.15b)\end{aligned}$$

The particular solution to these equations is the Ekman flow

$$\begin{aligned}\overline{U}_1 \mathrm{e}^{-i\omega t} &= 2U_o\left(1-\sigma^2\right)^{-1}\mathrm{e}^{-i\omega t}, &(6.16a)\\ \overline{U}_2 \mathrm{e}^{-i\omega t} &= -2iU_o\left(1-\sigma^2\right)^{-1}\sigma\mathrm{e}^{-i\omega t}, &(6.16b)\end{aligned}$$

where

$$\begin{aligned}\sigma &= \frac{\omega+i\mu}{f_o}, &(6.17a)\\ U_o &= \frac{T}{2f_o}. &(6.17b)\end{aligned}$$

The radial component of this is

$$\begin{aligned}\overline{U}_r \mathrm{e}^{-i\omega t} &= \left(\overline{U}_1\cos\theta + \overline{U}_2\sin\theta\right)\mathrm{e}^{-i\omega t}\\ &= U_o\left(1-\sigma^2\right)^{-1}\left[(1-\sigma)\mathrm{e}^{i(\theta-\omega t)} + (1+\sigma)\mathrm{e}^{-i(\theta+\omega t)}\right].\end{aligned} \tag{6.18}$$

Homogeneous wind forcing in the absence of relief and complicated geometry projects solely onto the first azimuthal mode. Assuming ω, $f_o > 0$, the clockwise part of (6.18) is resonant for $\omega = f_o$ apart from any island-associated effect.

The governing equations for the island-associated field are

$$-if_o\sigma U_\alpha - f_o\varepsilon_{\alpha\beta}U_\beta + \partial_\alpha P = 0, \tag{6.19a}$$

$$-if_o\sigma P + gh\partial_\alpha U_\alpha = 0. \tag{6.19b}$$

By eliminating U_1 and U_2, one finds

$$r_d^2\,\partial_\alpha\partial_\alpha P - (1-\sigma^2)P = 0, \qquad r_d = \frac{\sqrt{gh}}{f_o}. \tag{6.20}$$

The horizontal velocity components are related to P according to

$$f_o(1-\sigma^2)U_r = i\sigma\partial_r P - \frac{1}{r}\partial_\theta P, \tag{6.21a}$$

$$f_o(1-\sigma^2)U_\theta = \partial_r P + \frac{i}{r}\sigma\partial_\theta P. \tag{6.21b}$$

In order to satisfy the radial boundary condition (6.4),

$$U_r = -\overline{U}_r \quad \text{at} \quad r = a. \tag{6.22}$$

This boundary condition may expressed in terms of P as

$$i\sigma\partial_r P - \frac{1}{r}\partial_\theta P = -\frac{T}{2}\left[(1-\sigma)\mathrm{e}^{i\theta} + (1+\sigma)\mathrm{e}^{-i\theta}\right] \quad \text{at} \quad r = a. \tag{6.23}$$

Solutions to (6.23) may be found of the form

$$P\mathrm{e}^{-i\omega t} = iP_o\frac{R(r)}{R(a)}\left[\xi_{ccw}\mathrm{e}^{i(\theta-\omega t)} + \xi_{cw}\mathrm{e}^{-i(\theta+\omega t)}\right], \tag{6.24}$$

where

$$P_o = \frac{aT}{2}, \tag{6.25a}$$

$$\xi_{ccw} = (1-\sigma)\left(\sigma\frac{a\partial_r R(a)}{R(a)} - 1\right)^{-1}, \tag{6.25b}$$

$$\xi_{cw} = (1+\sigma)\left(\sigma\frac{a\partial_r R(a)}{R(a)} + 1\right)^{-1}. \tag{6.25c}$$

In terms of these parameters, the velocity components of the island-associated field are

$$U_\theta \mathrm{e}^{-i\omega t} = i\tfrac{U_o}{R(a)}(1-\sigma^2)^{-1} \left\{ \left[a\partial_r R(r) - \sigma \frac{a}{r} R(r) \right] \xi_{ccw} \mathrm{e}^{i(\theta-\omega t)} + \left[a\partial_r R(r) + \sigma \frac{a}{r} R(r) \right] \xi_{cw} \mathrm{e}^{-i(\theta+\omega t)} \right\}, \quad (6.26a)$$

$$U_r \mathrm{e}^{-i\omega t} = \tfrac{U_o}{R(a)}(1-\sigma^2)^{-1} \left\{ \left[\frac{a}{r} R(r) - \sigma a\partial_r R(r) \right] \xi_{ccw} \mathrm{e}^{i(\theta-\omega t)} - \left[\frac{a}{r} R(r) + \sigma a\partial_r R(r) \right] \xi_{cw} \mathrm{e}^{-i(\theta+\omega t)} \right\}. \quad (6.26b)$$

The radial structure function R must satisfy

$$r^2\partial_r^2 R + r\partial_r R - \left[1 + \varepsilon \frac{r^2}{a^2} \left(1-\sigma^2 \right) \right] R = 0, \quad (6.27)$$

where the nondimensional parameter ε is

$$\varepsilon = \left(\frac{a}{r_d} \right)^2 = \frac{a^2 f_o^2}{g h_n} \quad (6.28)$$

[Longuet-Higgins, 1969].

If the forcing is subinertial, one may define

$$\kappa = \frac{1}{r_d}\sqrt{1-\sigma^2} = \frac{1}{a}\sqrt{\varepsilon\,(1-\sigma^2)}. \quad (6.29)$$

Subinertial solutions to (6.27) are the modified Bessel functions

$$R = \begin{cases} K_1(\kappa r), \\ I_1(\kappa r). \end{cases} \quad (6.30)$$

The K solution is the island-trapped solution of interest; $I(\kappa r)$ becomes infinite as $r \to \infty$ and is therefore discarded. For the radial structure function $K_1(\kappa r)$,

$$a\partial_r R(r) = \kappa a K_1'(\kappa r) = -\kappa a K_0(\kappa r) - \frac{a}{r} K_1(\kappa r). \quad (6.31)$$

According to (6.25b) and (6.25c), there is an infinite response if $\mu = 0$ and

$$\frac{K_1(\kappa a)}{\kappa a K_1'(\kappa a)} = \pm \frac{\omega}{f_o}. \quad (6.32)$$

This expression, identical to (2.7) with $m = 1$, determines the natural frequencies of the free system [LONGUET-HIGGINS, 1969].

If the forcing is superinertial, one may define

$$k = \frac{1}{r_d}\sqrt{\sigma^2 - 1} = \frac{1}{a}\sqrt{\varepsilon\left(\sigma^2 - 1\right)} \tag{6.33}$$

to find solutions of (6.27) of the form

$$R = \begin{cases} H_1^{(1)}(kr), \\ H_1^{(2)}(kr). \end{cases} \tag{6.34}$$

For outgoing phase only at $r \to \infty$, the solution $H_1^{(2)}$ must be rejected, because

$$H^{(1)}(kr)\mathrm{e}^{-i\omega t} \quad \propto \quad \mathrm{e}^{i(kr-\omega t)}, \tag{6.35a}$$

$$H^{(2)}(kr)\mathrm{e}^{-i\omega t} \quad \propto \quad \mathrm{e}^{-i(kr+\omega t)} \tag{6.35b}$$

as $r \to \infty$. Far away from the island, energy radiates outward at the phase speed $\sqrt{gh_n}$ for each mode. The radial structure function obeys

$$a\partial_r R(r) = kaH_1'^{(1)}(kr) = kaH_0^{(1)}(kr) - \frac{a}{r}H_1^{(1)}(kr). \tag{6.36}$$

From (6.25b) and (6.25c), maximum pressure disturbances occur for minimum values of

$$\left| kaH_1'^{(1)}(ka) \pm \frac{f_o}{\omega}H_1^{(1)}(ka) \right| \tag{6.37}$$

if $\mu = 0$. Minimum values of this expression, equivalent to (2.22) with $m = 1$, give the pseudo-resonant scattering peaks considered by WUNSCH [1972].

6.1.2 Magnitude of the model output

The radial structure of subinertial motion is described by the modified Bessel function K of complex argument κr. For $\mu/f_o = 0.015$ (shown later to be a reasonable choice), the imaginary part of κ remains negligible unless ω is very close to f_o:

ω/f_o	$\arg(\kappa)$ (rad)	$(\lvert\kappa\rvert\, r_d)^{-1}$
.90	-.0705	2.28
.95	-.1419	3.13
.99	-.4876	5.28
1.00	-.7816	5.77

Presumably, the near-inertial solutions are described by a mix of the trapped K_1 and freely-propagating $H_1^{(1)}$ structure functions. This complication exists outside the frequency band of interest for the baroclinic coastal wave system and will not be dealt with here. Consequently, the near-inertial response of this model ($0.9 \geq \omega/f_o \geq 1.1$ for damping of order $\mu/f_o < 0.03$) must not be seriously considered.

Values of the physical parameters were chosen to model trapped waves at the island of Hawaii [LUTHER, 1985] for all model runs except those otherwise specified:

PARAMETER	SYMBOL	VALUE
Island radius	a	70.3×10^3 m
Inertial frequency	f_o	4.88×10^{-5} s^{-1}
Buoyancy frequency	N	2.99×10^{-3} s^{-1}
Total depth	h_0	3.0×10^3 m
Mixed layer depth	h_{mix}	90 m

These values yield a first baroclinic deformation radius of 58.5 km. The total depth was chosen so that the equivalent depth of baroclinic mode n is $h_n = .83/n^2$ m, for consistency with LUTHER [1985]. A surface wind stress of 0.1 N/m^2 was chosen to force the model [GILL AND CLARKE, 1974].

An equivalent sea surface displacement $\eta_{\rm eq}$ may be defined from the perturbation pressure at the rigid lid as

$$\eta_{\rm eq} = g^{-1} p|_{x3=0}. \tag{6.38}$$

A plot of the mean-square $\eta_{\rm eq}$ for $\mu/f_o = 0, 0.015$ and 0.03 appears as Fig. 26, where

$$\begin{aligned} \text{ms}\ \eta_{\rm eq} &= \tfrac{1}{4\pi^2}\int_0^{2\pi} \mathrm{d}\theta \int_0^{2\pi} \mathrm{d}(\omega t)\ \ \mathrm{Re}(\eta_{\rm eq})^2 \\ &= \tfrac{1}{2g^2}\sum_{n,m} P_o^n P_o^m \left[\alpha_1^n \alpha_1^m \cos\left(\psi_1^n - \psi_1^m\right) + \alpha_2^n \alpha_2^m \cos\left(\psi_2^n - \psi_2^m\right)\right] \end{aligned} \tag{6.39}$$

and

$$\alpha_1 e^{i\psi_1} = i\frac{R(r)}{R(a)}\xi_{ccw}, \qquad \alpha_2 e^{i\psi_2} = i\frac{R(r)}{R(a)}\xi_{cw}, \qquad \alpha_{1,2} \text{ real.} \tag{6.40}$$

The phase Φ plotted in Fig. 26 is defined by

$$\Phi = \text{Arg}\left\{\eta_{\text{eq}}(t=0,\theta=0)\right\} = \text{Arg}\left\{\frac{i}{g}\sum_n P_o \frac{R(r)}{R(a)}\left(\xi_{ccw}+\xi_{cw}\right)\right\}. \tag{6.41}$$

Resonance is apparent at the subinertial eigenfrequencies, and is accompanied by a phase shift which approaches 180° for low baroclinic modes and low dissipation. There is a peak at $\omega = f_o$ caused by resonance of the Ekman-driven far field. The superinertial response falls off very rapidly with increasing frequency; there is no sign of the pseudo-resonant superinertial peaks of WUNSCH [1972]. This result is not surprising, as the off-inertial pseudo-resonant peaks are formed by the higher azimuthal modes (note the range of pseudo-resonance shown for the first four azimuthal modes in Fig. 5). Due to the lack of resonance or pseudo-resonance in the superinertial response of the system, only the subinertial response will be subsequently examined.

Adjusted sea level records at Hilo, Hawaii reveal a strong seasonality in the amplitude of the gravest subinertial coastal wave [LUTHER, 1985] (see Fig. 17). The Q (defined as the peak frequency divided by the half-power bandwidth) and rms amplitudes of some strong winter events are listed below:

WINTER	Q	rms η (cm)
1967–1968	13.3	1.3
1968–1969	8.8	1.4
1969–1970	10.7	1.7
1971–1972	16.7	1.3
1974–1975	10.7	1.1
(MEAN)	12.0	1.4

For $\mu/f_o = 0.015$ (damping time scale $\approx$ 15.8 days), τ_o=0.1 N/m^2 and ρ_o=1024 kg/m^3, the dimensional values of rms $\eta_{\text{eq}}(r=a)$ and rms $u_\theta(x_3=0, r=a)$ at the first baroclinic trapped wave eigenfrequency are 1.1 cm and 6.0 cm/s, with a Q (for the mean-square

$\eta_{\rm eq}/\omega$ plotted in Fig. 26) of 13.8. Thus, according to this model, a typical oceanic wind stress distributed over a large region should lead to an observable trapped wave signal. While island-trapped waves an order of magnitude larger are observed in the Alenuihaha Seadata record, these results suggest that local wind forcing may play a major role in subinertial wave generation at the island of Hawaii.

The currents forced at the first baroclinic eigenfrequency with $\mu/f_o = 0.015$ are shown in Fig. 27. This snapshot of the flow field is taken at $t = 0$, and at four depths in the water column. The vertical mode sum has been over the first 100 modes. The resulting motion is dominated by the $\cos(n\pi x_3/h_0)$ structure of the resonantly-forced gravest mode. At $t = 0$, the wind is at its northward magnitude, with a resulting far-field current nearly eastward (a slight northward component is caused by the lag introduced by dissipation). The convergence/divergence on the western/eastern side of the island results in downward/upward isopycnal displacements, which have their maximum amplitude of 16 m at $x_3/h_0 = -0.5$. These displacements lead to the geostrophically balanced (in the radial direction) flow of vertical mode one visible below the mixed layer in Fig. 27. The model effectively demonstrates that coastal wave dynamics produce motion well below the mixed layer.

The currents shown in Fig. 27 rotate clockwise around the island due to the dominance of the clockwise part of the island-associated field. This rotation of the dissipationless system at near-resonant forcing is shown in the top half of Fig. 28, where the sum over the vertical modes has only been taken to the first term (the gravest baroclinic mode). While the maximum northward to eastward far field velocity in the dissipationless system scales as

$$\overline{U}_2(\max)/\overline{U}_1(\max) = \omega/f_o, \tag{6.42}$$

chosen in Fig. 28 to be 0.55, the island-associated azimuthal velocity maxima (separated by a quarter of a period) have a ratio greater than 0.9 (bottom half of Fig. 28). Thus, the near-resonant response to a north-south wind displays considerable azimuthal symmetry.

An interesting result obtained from this model is that the amplitude of the gravest subinertial trapped wave is not a function of the island radius a for a wide range of values. For example, if Hawaii values of all parameters except island radius a are fixed and the model is forced with a wind stress of 0.1 N/m^2 and dissipation $\mu/f_o = 0.015$, the root-mean-square equivalent surface displacement at the first baroclinic eigenfrequency is:

ISLAND RADIUS a (m)	1st baroclinic eigenfrequency (ω/f_o)	rms η_{eq} (cm)
4.69×10^4	0.78	1.06
7.03×10^4	0.60	1.08
1.05×10^5	0.44	1.08

Sea level observations indicate that first azimuthal, first baroclinic coastal waves around the island of Hawaii are much more energetic on average than those around the Maui group or Oahu. Two mechanisms may explain this observation. First, the geometric complications of the Maui group, including the channels which could act to relax surface displacements, and the many sharp turns in the ray path, may damp trapped wave energy at that island. At Oahu, less energetic sea level displacements may follow from trapping of the waves' energy on the shallower topographic slope. Alternatively, the forcing may be enhanced at Hawaii due to the significant vertical relief of the island more so than at Oahu and at Maui, where lee enhancement of Ekman pumping behind Haleakala may fall within the shallow channels of the island group.

The model equivalent surface displacement response displays a prominent peak at near-inertial forcing frequencies (see Fig. 26). This peak, which dominates the model's near-inertial current field, is not a feature of observed sea level or current spectra.

This may reflect the approximations (ignoring the barotropic part of the field and the complex part of the offshore wavenumber) which are not appropriate for near-inertial forcing. In any event, the inertial peak is the result of direct resonance of the far field to the forcing, independent of the island-trapped wave dynamics of interest here. Thus, a normalization of the model output was desired which would minimize this feature. This normalization was conducted by dividing the energy of the model output by the averaged far-field kinetic energy $\bar{e}_k$, defined as

$$\bar{e}_k = \frac{1}{2}\,\mathrm{Re}(\bar{u}_\alpha)\,\mathrm{Re}(\bar{u}_\alpha). \tag{6.43}$$

This far-field kinetic energy may be averaged to obtain

$$\langle \bar{e}_k \rangle = \frac{1}{4}\frac{h_{mix}}{h_0}\left(\frac{\tau_o}{f_o \rho_o h_{mix}}\right)^2 \left(\left| \frac{1}{1-\sigma^2} \right|^2 + \left| \frac{\sigma}{1-\sigma^2} \right|^2 \right), \tag{6.44}$$

where $\langle\ \rangle$ is the operator

$$\langle\ \rangle = \frac{1}{h_0}\int_{-h_0}^{0} \mathrm{d}x_3\ \frac{1}{4\pi^2}\int_0^{2\pi} \mathrm{d}\theta\ \int_0^{2\pi} \mathrm{d}(\omega t)\ . \tag{6.45}$$

The specific potential and kinetic energy is

$$e_p = \frac{1}{2}N^2\,\mathrm{Re}(\eta)^2 = \frac{1}{2N^2}\,\mathrm{Re}\left(\partial_3 p\right)^2, \tag{6.46a}$$

$$e_k = \frac{1}{2}\,\mathrm{Re}\left(u_\alpha\right)\,\mathrm{Re}\left(u_\alpha\right), \tag{6.46b}$$

where u_1, u_2 are composed of both the directly-forced far-field and the island-associated field.

A plot of $\langle e_k + e_p \rangle / \langle \bar{e}_k \rangle$ vs. ω/f_o for varying μ/f_o at $r/a = 1.25$ (Fig. 29) demonstrates how damping affects the resonant peaks. For dissipation time scales as long as 7.9 days ($\mu/f_o = 0.03$), resonant peaks past the third baroclinic mode no longer appear in the response. By plotting $\langle e_k + e_p \rangle / \langle \bar{e}_k \rangle$ vs. ω/f_o for values of r/a from 1 to 3 (Fig. 30), one sees that the low-frequency response of the system is tightly trapped to

the island. This is because the trapping scale κ_n^{-1} for baroclinic mode n is proportional to n^{-1} in the constant N^2 model; actual trapping scales would decay more rapidly with increasing n due to the influence of the island flanks [HOGG, 1980]. Beyond $r/a = 1.75$, the response of a baroclinic mode higher than the third is limited to the projection of the Ekman-driven mixed layer motion onto that mode.

6.1.3 Comparison with observations

How closely does the normalized model output compare with observed resonant coastal waves at Hawaii? Data chosen for this comparison were Hilo sea level and azimuthal velocity measured at the Alenuihaha Seadata site. Seadata sets 3–7 were chosen due to the short lengths of sets 1 and 2; these data cover the period 26 November 1984 to 26 May 1986 (see Table 3.3).

All model spectra were normalized by multiplication with the quantity

$$\frac{u_o^2}{\langle \bar{e}_k \rangle}, \tag{6.47}$$

where $\langle \bar{e}_k \rangle$ is given in (6.44). The constant u_o was chosen such that the energy level of the first baroclinic peak in the graph of

$$\frac{2\pi}{\omega} \frac{u_o^2}{\langle \bar{e}_k \rangle} \text{ ms } \eta_{\text{eq}} \tag{6.48}$$

(ms = mean-square) matched the observed spectral energy (Fig. 31). In order to achieve the close fit shown in the figure, $\mu/f_o = 0.03$ and $u_o = 1.7$ cm/s. The radial distance r/a for Fig. 31 is 1.0.

Given these choices of parameters, a plot of

$$\frac{2\pi}{\omega} \frac{u_o^2}{\langle \bar{e}_k \rangle} \text{ ms } u_\theta \tag{6.49}$$

and the observed azimuthal velocity at the Seadata site appear as Fig. 32. The radial distance r/a was chosen as 1.1; the mean-square azimuthal velocity at depths of 50 m

(dotted) and 100 m (dashed) were computed to represent the model results within and below the mixed layer (total depth 90 m). The model underestimates the spectral density at the first baroclinic peak, while overestimating the energy level of the higher peaks. In addition, the model spectrum is redder than the observations.

The major discrepancy between the model and the observations is the presence of sharp resonant peaks at the higher mode eigenfrequencies. It would be a straightforward extension of this model to admit scale-dependent dissipation; because the higher modes are described by smaller scales vertically and radially, the extended model could then match the energy level and Q of the gravest peak while dropping the energy levels of the higher peaks. Essentially, of course, this extension adds an additional, "tunable" parameter resulting in a higher correspondence between the model output and the observations. Thus, while scale-dependent damping may be argued on a physical basis, our dynamical understanding of island-trapped waves would not be significantly enhanced by this exercise.

A second explanation for the reduced energy of the observed higher peaks may lie in the geometrical approximations made for the model island. Numerical studies indicate that higher-radial mode trapped waves around a seamount are tightly trapped to the seamount flank [Brink, 1990]. As argued earlier, the baroclinic modes of the model must exceed the horizontal scale of the island flank to justify the vertically-walled cylinder model of the island. For Hawaii values of f_o, $h_n = .83/n^2$ and a typical flank scale of 5–10 km, the approximation is no longer valid for modes 5 to 10. Because baroclinic mode 2 has a deformation radius to island flank ratio of 3 to 6, the vertically-walled approximation is qualitatively applicable to this mode and cannot be used to explain the discrepancies between the model and the observations at the first few baroclinic mode eigenfrequencies. This mechanism may play an important role for the lower

frequency, higher baroclinic modes, which are overestimated in the model azimuthal velocity response (see Fig. 32).

Future models of forced waves trapped around islands must address some of the geometrical and/or topographic complexities not dealt with in this study. Two possible extensions to the model which may retain analytical tractability are enhancement of the Ekman pumping regions due to a wind shadow and leakage of energy from one closely-spaced island to another. Numerical work, especially comparing existing data sets of currents and sea level with the predictions of a modified version of BRINK's [1990] seamount-trapped wave model in the presence of scale-dependent damping, offers a promising path for future research.

6.2 Leakage of trapped wave energy

The 2.5 day coastal wave at Hawaii has a trapping scale κ^{-1} of approximately 72 km according to (2.8) and the parameters given in Table 2.1. The distance from Hawaii to Maui is approximately 40 km. Because isopycnal displacements associated with island-trapped waves have a radial structure of the form $K_m(\kappa r)$, Hawaii's gravest wave will be felt at Maui reduced by a factor of

$$\frac{K_1[1.38 \times 10^{-5}\ \mathrm{m}^{-1}\ \cdot (7.03 \times 10^4\ \mathrm{m}\ + 4 \times 10^4\ \mathrm{m})]}{K_1(1.38 \times 10^{-5}\ \mathrm{m}^{-1}\ \cdot 7.03 \times 10^4\ \mathrm{m})} \approx 0.4. \tag{6.50}$$

The gravest coastal wave at Hawaii is energetic, particularly in the winter months (see Fig. 17). During energetic trapped wave events at Hawaii, appreciable vertical displacements should be felt at the southeastern side of the Maui island group. The relaxation of these displacements would then lead to the generation of trapped waves around the Maui island group [LUTHER, 1985]. In theory, this remote forcing mechanism is particularly effective for Hawaii and Maui; the eigenfrequencies of these islands are close enough to allow for co-resonant leakage.

6.2.1 Evidence of leakage

LUTHER [1985] noted that a coherence peak between sea level at Hilo and Kahului occurs near the eigenfrequencies of Hawaii and the Maui group (Fig. 33). Because the trapped waves at Hilo are much more energetic on average than those at Kahului, this coherence peak suggests that the trapped wave at Hawaii may be leaking energy onto the Maui island group [LUTHER, 1985]. A running coherence between the two ASL records from 1966 to 1974, band-passed from 2.5 days to 2.83 days period (Fig. 34), reveals that energetic events in the Hilo record are often mirrored by peaks in the Kahului record. For several events, these concurrent peaks are accompanied and an increase in the coherence amplitude between the band-passed signals. This is especially evident during the most energetic event in the record, which occurred in the winter of 1969–1970 (Fig. 35). Kahului leads Hilo by 20° to 40° during many of these coherent events. It must be noted, however, that not all energetic events in the Hilo trapped wave band correspond to coherent events between the two records; an example of this occurs in the winter of 1973–1974 (see Fig. 34).

The demodulated amplitude of Kahului ASL shown in Fig. 34 peaks in the summer of 1971, during which no energetic trapped waves appear in the Hilo record. Spectra of the two ASL records during this summer (Fig. 36) reinforce the fact that the islands can be excited independently, and that the Maui group can support resonant coastal waves without leakage from Hawaii. Nevertheless, energetic events in the Hilo record often accompany coherent events between the two islands, suggesting that leakage is a significant forcing mechanism for the Maui trapped waves.

The spectra of Kahului and Hilo ASL in the winter of 1969–1970 (not shown) both have peaks at 2.51 days period. Leakage, rather than simultaneous wind forcing, is the most likely explanation for the Kahului spectrum peaking at this period. This is

because the theoretical natural periods of the two islands are significantly different (see Table 2.1), and should respond most strongly at these different periods in the presence of broad-band forcing. It should be noted that the spectrum of the wind at Kahului during this winter (not shown) does not contain any peaks in the 2 to 3 day period band.

The periods of peaks in the trapped wave band at Hilo may be plotted vs. those at Kahului for the entire 1966–1974 record (Fig. 37) to reveal that concurrent peaks fall into two regimes. In the "coupled" regime indicated in Fig. 37, energy peaks occur at the same period in the two records. In the "uncoupled" regime, the period of the wave at Kahului falls near the theoretical value for the Maui group, while the peak at Hawaii is at the slightly smaller period for that island. The points which fall in the "coupled" regime correspond to the coherent events shown in Fig. 34.

The intertidal sea level peak at Kahului, with an accompanying coherence peak between Kahului and Hilo ASL (see Fig. 33), was also suspected to be evidence of leakage by LUTHER [1985]. However, the intertidal peak periods at Hilo vs. those at Kahului (not shown) do not tend to fall along the $T_{\mathrm{Hilo}} = T_{\mathrm{Kahului}}$ line, but instead define a random scattering of points. A running coherence of the superinertial motion at Kahului and at Hilo (not shown) reveals an event which is energetic and highly coherent (amplitude greater than 0.9), but also reveals several events which are energetic and not significantly coherent.

Is the phase difference between the Kahului and Hilo records during the coherent events (see Fig. 34) consistent with coastal wave leakage from Hawaii to Maui? If the phase of the first azimuthal mode wave at Hawaii is mapped across the Alenuihaha Channel at the narrowest point between Hawaii and Maui without phase change, Kahului leads Hilo by 35–45° when the Pailolo Channel between Maui and Molokai is included

in the ray path (Fig. 38). If this channel is skipped while mapping the ray path of the coastal wave (which, incidentally, results in a smaller equivalent radius than that given by LUTHER [1985]), Kahului leads by approximately 100°. Due to the complicated geometry of the Maui island group, no definitive statement about the phase shift can be made; it would seem, however, that the observed $\approx 30^\circ$ shift is not inconsistent with the hypothesis of leakage.

6.2.2 Multiple regression analysis of Kahului ASL

It is not immediately obvious from the running coherence of Fig. 34 that simultaneous, direct wind forcing of the two islands' trapped waves does not adequately explain the observations. An argument against this explanation is the fact that the peak periods of the two records are identical during the coherent events, suggesting coupling of the trapped waves at the two islands. However, this argument does not quantify the importance of leakage as a forcing mechanism for the trapped waves observed at Kahului.

In Section 6.1, a large-scale wind field was shown to be an efficient forcing mechanism for island-trapped waves. Evidence for this may be found in the coherence between Hilo ASL and the north wind at Kahului (Fig. 25). The coherence amplitude reaches a peak at 2.6 days period, very near the natural period of the island. This peak is accompanied by a phase shift of nearly 180°, as one would expect for a linear system forced at its eigenfrequency. Interestingly, Hilo ASL is less coherent with the winds measured at Hilo Airport. Perhaps this is due to contamination of the meteorological data by nearby structures or topography, resulting in the Hilo data not accurately reflecting the local winds.

The coherence amplitude between Kahului ASL and north wind at Kahului (Fig. 39) has peaks at 1.9 and 2.7 days period. The latter is at a somewhat larger period than

the Maui island group's natural period. This coherence peak overlaps the peak between Hilo ASL and Kahului ASL (Fig. 33), which has a maximum at 2.56 days period.

In order to separate the effects of direct wind forcing from leakage in Kahului ASL, the multiple regression technique [DAVIS AND BOGDEN, 1989] was employed as outlined below. Consider $\eta_{\mathrm{K}}(t)$, the ASL record at Kahului, forced by three input functions F_i, $i = 1, 2, 3$, where

$$\begin{array}{lcll} F_1 & = & \eta_{\mathrm{H}}(t), & \text{(ASL at Hilo)}, \\ F_2 & = & N(t) & \text{(North wind at Kahului)}, \\ F_3 & = & E(t) & \text{(East wind at Kahului)}. \end{array} \tag{6.51}$$

With the addition of noise representing the variance of η_{K} incoherent with these inputs, the Fourier components of this system are given by

$$\tilde{\eta}_{\mathrm{K}}(\omega) = a_j(\omega)\tilde{F}_j(\omega) + \tilde{n}(\omega). \tag{6.52}$$

Summation convention is implied for repeated vector indices. Because the true transfer functions a_{1-3} are unknown, one may let

$$\hat{\eta}_{\mathrm{K}} = \alpha_j \tilde{F}_j, \tag{6.53}$$

and determine the α's by minimizing

$$\begin{array}{rcl} \tilde{n} & = & \tilde{\eta}_{\mathrm{K}} - \hat{\eta}_{\mathrm{K}} \\ & = & \tilde{\eta}_{\mathrm{K}} - \alpha_j \tilde{F}_j \end{array} \tag{6.54}$$

in a least-square sense [DAVIS AND BOGDEN, 1989]. From (6.54), the autospectrum of the noise is given by

$$S_{\hat{n}\hat{n}} = S_{\eta_{\mathrm{K}}\eta_{\mathrm{K}}} - \alpha_j V_j^* - \alpha_j^* V_j + \alpha_i^* \alpha_j D_{ij}, \tag{6.55}$$

where

$$\boldsymbol{V} = \begin{pmatrix} S_{\eta_{\mathrm{K}}1} \\ S_{\eta_{\mathrm{K}}2} \\ S_{\eta_{\mathrm{K}}3} \end{pmatrix}, \tag{6.56}$$

and

$$\mathbf{D} = \begin{pmatrix} S_{11} & S_{12} & S_{13} \\ S_{21} & S_{22} & S_{23} \\ S_{31} & S_{32} & S_{33} \end{pmatrix}. \tag{6.57}$$

By requiring $\frac{\partial S_{nn}}{\partial \alpha_i^*} = 0$, one finds

$$\alpha_j(\omega) = D_{ij}^{-1} V_i. \tag{6.58}$$

Thus, the estimated transfer functions α_{1-3} may be calculated from the matrix $\mathbf{D}$ formed from the auto- and cross-spectra of the inputs and the vector $\boldsymbol{V}$ formed from cross-spectra of the output with the inputs. The 95% confidence limits on the transfer function estimates may be calculated by doubling the standard error bars given by Davis and Bogden [1989].

The gain and phase of the transfer functions, defined by

$$\alpha_i = G_i(\omega) \mathrm{e}^{i\Phi_i}, \tag{6.59}$$

are shown in Figs. 40 and 41. Within the trapped wave band, the gain for the eastward component of the winds is not significantly greater than zero at the 95% confidence limit. The gain for the north wind is weak but significantly nonzero at 0.5 $\pm$ 0.25 cm per cm/s. The gain for Hilo ASL has a significant peak of 0.85 $\pm$ 0.3 cm per cm at a period of 2.6 days (the period of the observed peak in the Kahului autospectrum). This indicates that remote forcing is the dominant mechanism for generating the most energetic coastal wave at the Maui group.

In order to compare the relative impacts of the forcing inputs upon Kahului ASL, the three-input model described above was compared to regressions using only the local winds and only Hilo ASL as inputs. The total variance of the output for each model which is "predicted" from the input/inputs is

$$\boldsymbol{V}^* \mathbf{D}^{-1} \boldsymbol{V} \tag{6.60}$$

[Davis and Bogden, 1989]. The skill of the model may be defined as this quantity divided by $S_{\eta_K \eta_K}$, such that the skill represents the percent of variance predicted at each frequency [Davis, 1976]. In Fig. 42, the skills are shown for the three-input, two-input (representing local wind forcing), and one-input (representing remote forcing) models. The peak in the skill of the three-input model at 2.6 days period is matched in magnitude by the model with Hilo ASL as the sole forcing term.

For comparison with these results, the same skill calculations were made with Hilo ASL as the output and Kahului ASL and/or the local winds at Kahului as inputs. The skill in the 2.4 to 2.6 day band (not shown) was roughly balanced between the "local" and "remote" terms. Presumably, the skill of the one-input (Kahului ASL) model is due to the large coherence between the islands in this band (see Fig. 33). The observed energy level of the trapped waves at Hilo is much larger than the waves at Kahului during coherent events (see Fig. 34), justifying the assumption of leakage from Hawaii to Maui (rather than the reverse). Simultaneous trapped wave forcing from truly remote sources (such as surface wave set-up/set-down, Luther [1985]) cannot be ruled out by these regression analyses. However, such models fail to account for spectral peaks appearing at the same periods in the two signals (see Fig. 37).

These multiple regression analyses suggest that remote forcing, argued in this chapter to be leakage from the energetic coastal wave around Hawaii, is the dominant forcing mechanism for the observed 2.6 day peak in the Kahului ASL spectrum. Presumably, the effectiveness of this mechanism is enhanced by the proximity of the two islands' eigenfrequencies; an interesting pursuit for future study is to quantify the effectiveness of leakage in terms of the islands' radii and separation distance.

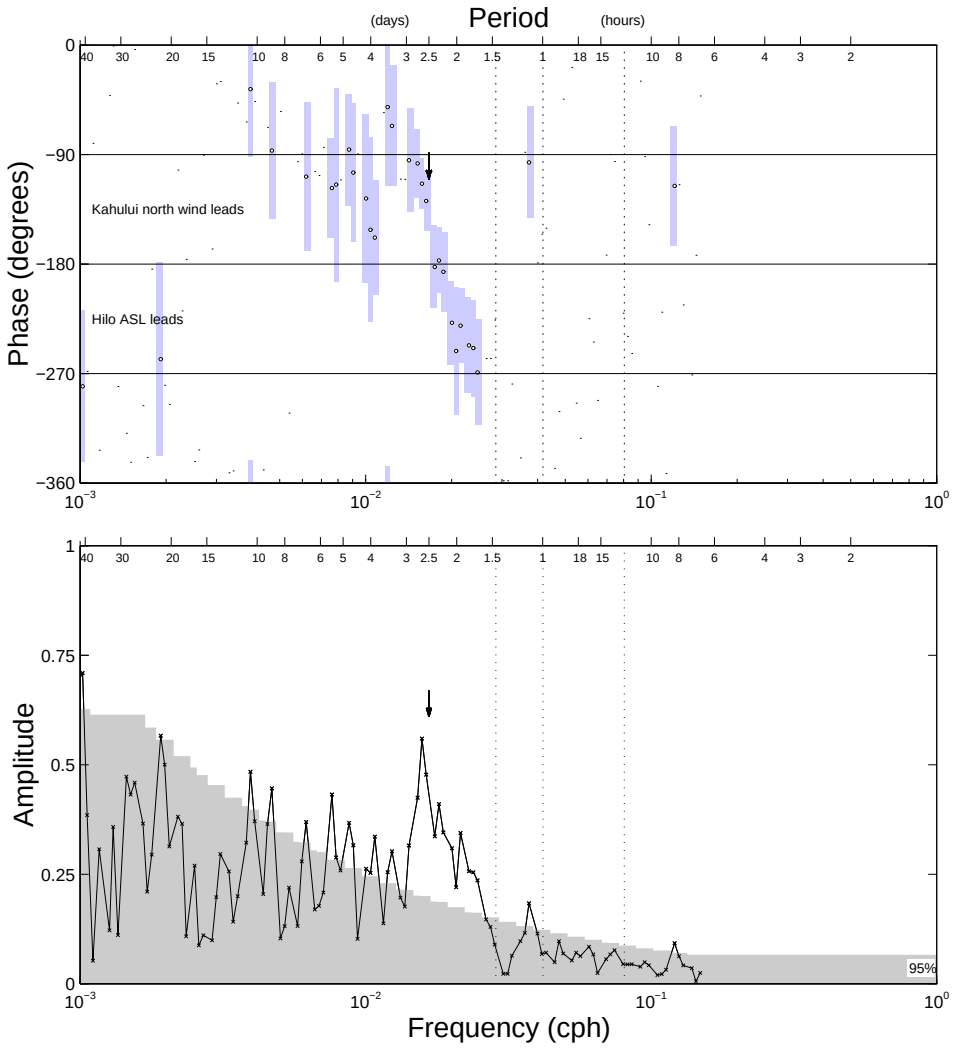

Figure 25: Coherence amplitude and phase between Hilo ASL and north wind at Kahului, 1966-1974. An arrow indicates the theoretical period of the gravest Hawaii trapped wave. Maximum coherence is 0.55 at 2.65 days period, corresponding to a phase shift of -114° ± 21°.

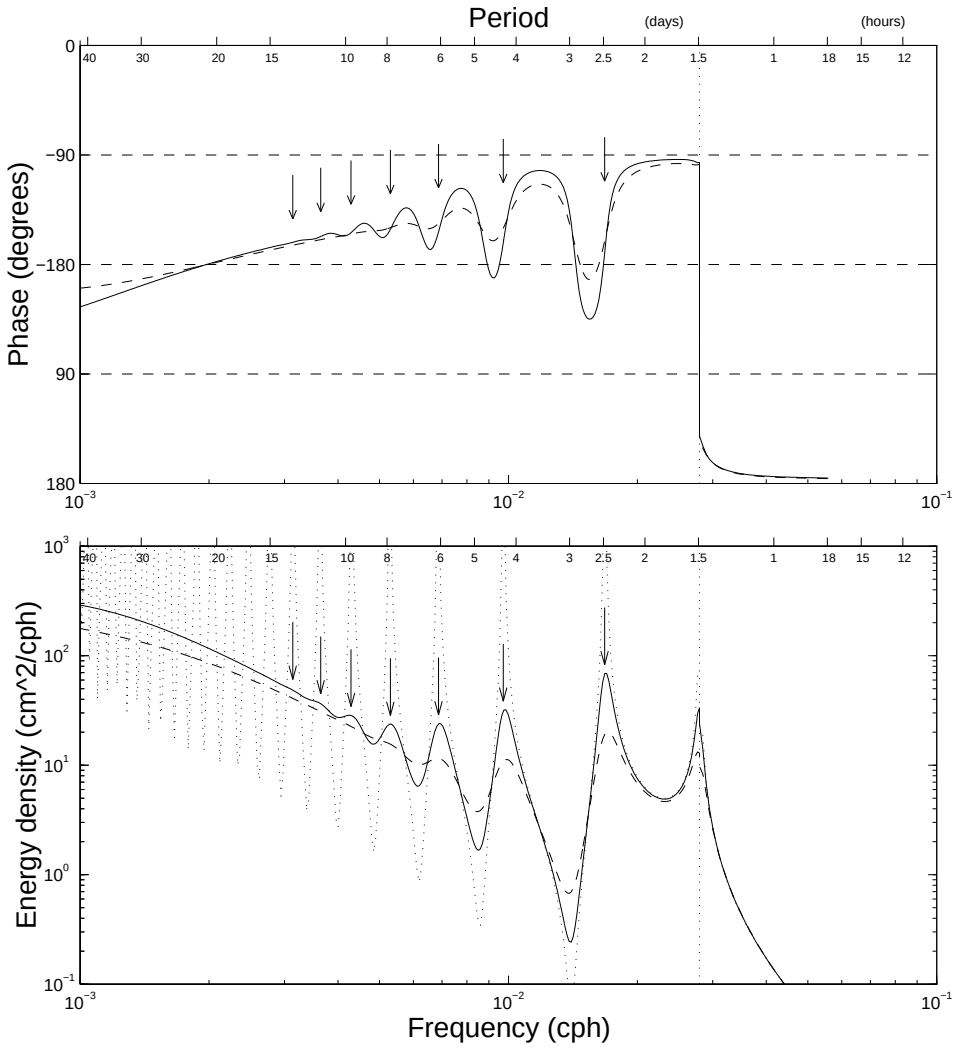

Figure 26: Mean-square equivalent surface displacement $\eta_{\rm eq}$ divided by frequency (in cph) vs. forcing frequency for $\mu/f_o = 0$ (dotted), 0.015 (solid) and 0.03 (dashed) (bottom figure). Phase Φ, plotted at top, is defined for $\eta_{\rm eq}$ at $t, \theta = 0$. Eigenfrequencies of the first seven baroclinic modes are indicated by arrows.

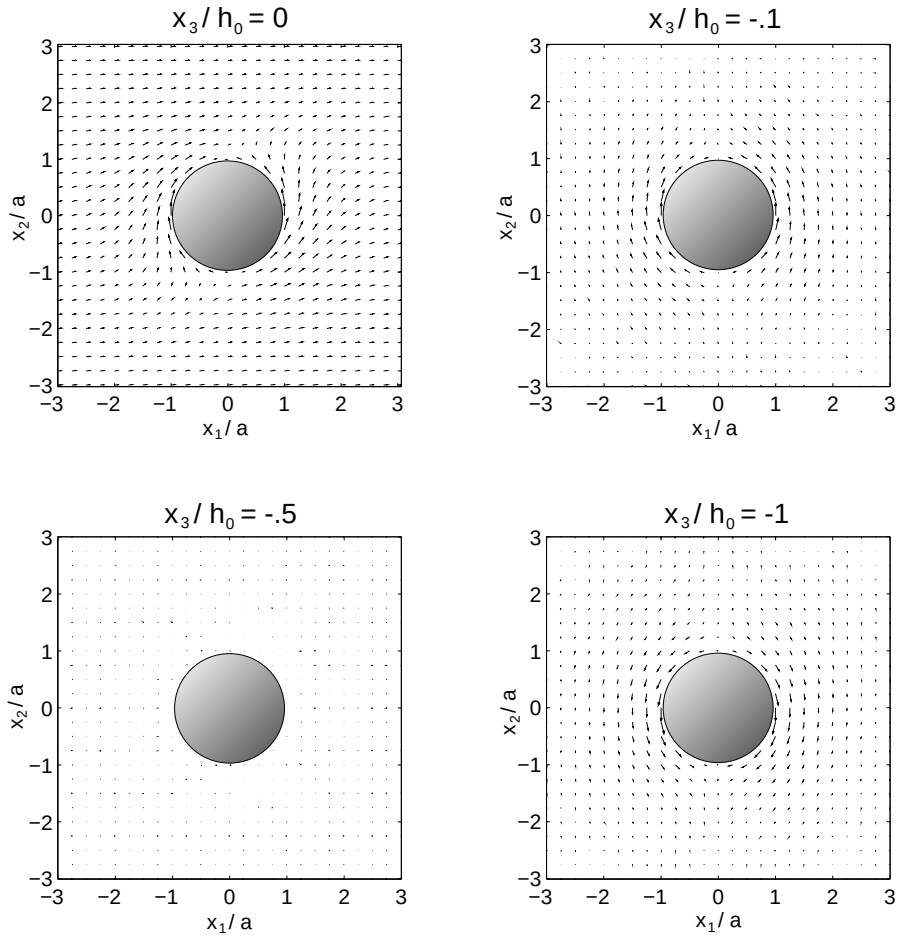

Figure 27: Model currents for Hawaii values of the physical parameters at $t = 0$, forced at $\omega/f_o = 0.60$ (the first baroclinic eigenfrequency) with dissipation $\mu/f_o = 0.015$. The base of the mixed layer is at $x_3/h_0 = -0.03$. For $\tau_o = 0.1$ N/m^2, the largest arrows are of magnitude 7.2 cm/s. The sum over the vertical modes has been carried over the first 100 terms.

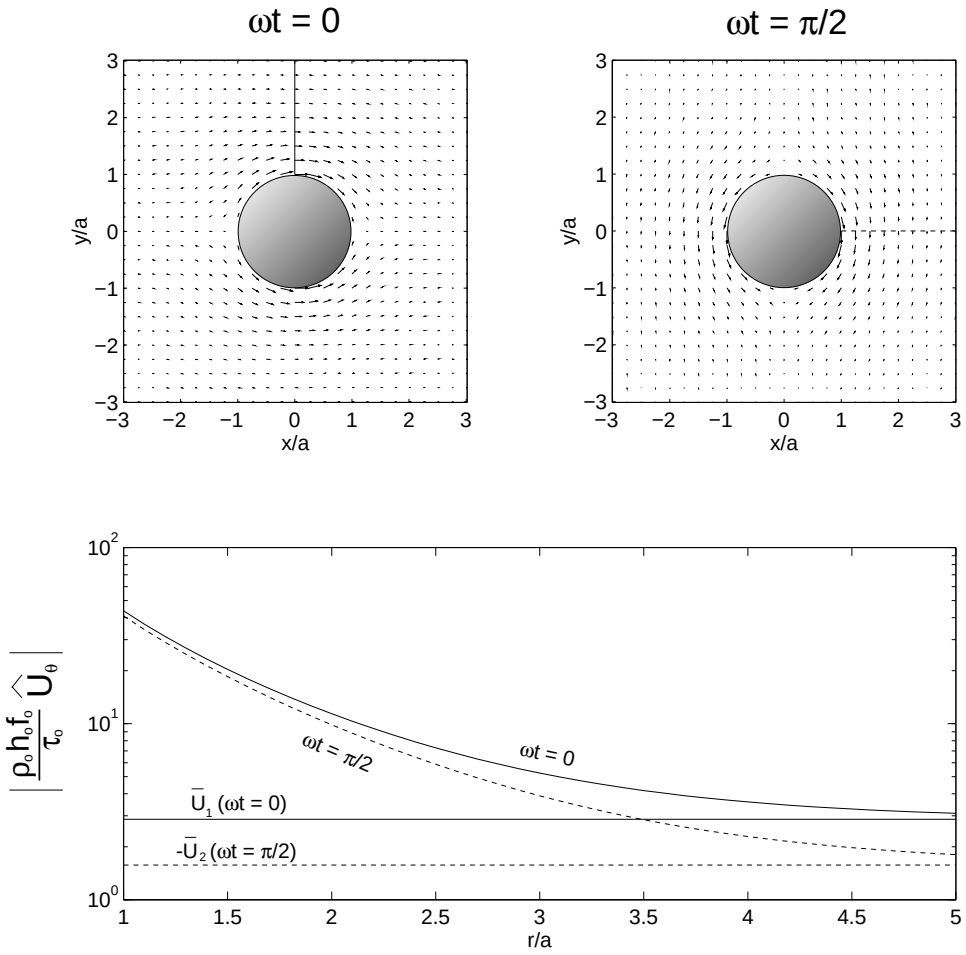

Figure 28: Model currents for Hawaii values of the physical parameters at $\omega t = 0$ and $\omega t = \pi/2$, forced at $\omega/f_o = 0.55$ with no dissipation at $x_3 = 0$. Only the contribution from the first baroclinic mode is shown. The (nondimensionalized) amplitude of the azimuthal velocity along the transects is plotted in the bottom panel, along with the magnitude of the far field velocity. Maximum values of the nondimensionalized azimuthal velocity are 43.7 at $\omega t = 0$, $r = a$ and 40.9 at $\omega t = \pi/2$, $r = a$, indicating the high degree of azimuthal symmetry in the model output.

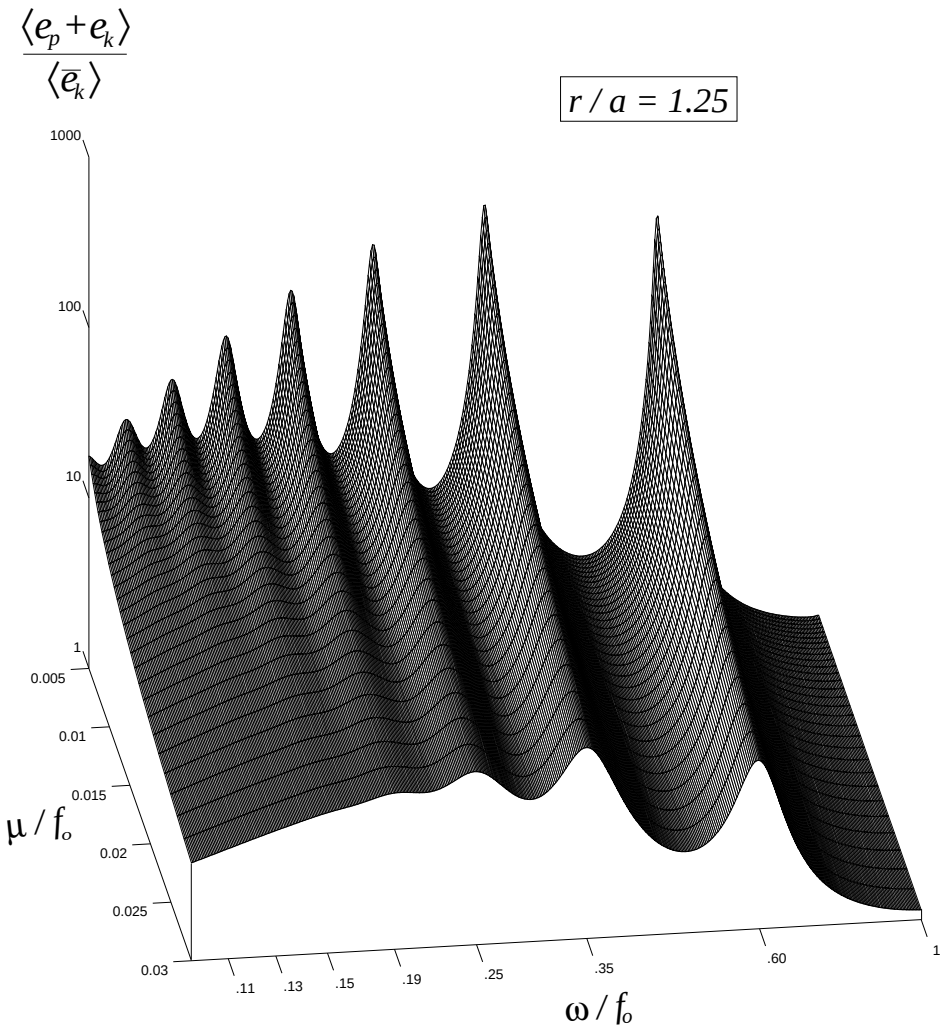

Figure 29: Total mean specific energy divided by mean background specific kinetic energy for the forced island-trapped wave model at $r = 1.25a$. Frequencies from $\omega/f_o = 0.1$ to $\omega/f_o = 1.0$ (inertial) are shown; tick marks are at the inertial frequency and at the baroclinic eigenfrequencies. A range of values for the dissipation parameter μ are plotted. A reasonable value of Q for the first baroclinic peak results from $\mu/f_o = 0.015 - 0.03$, corresponding to dissipation time scales of 7.9–15.8 days.

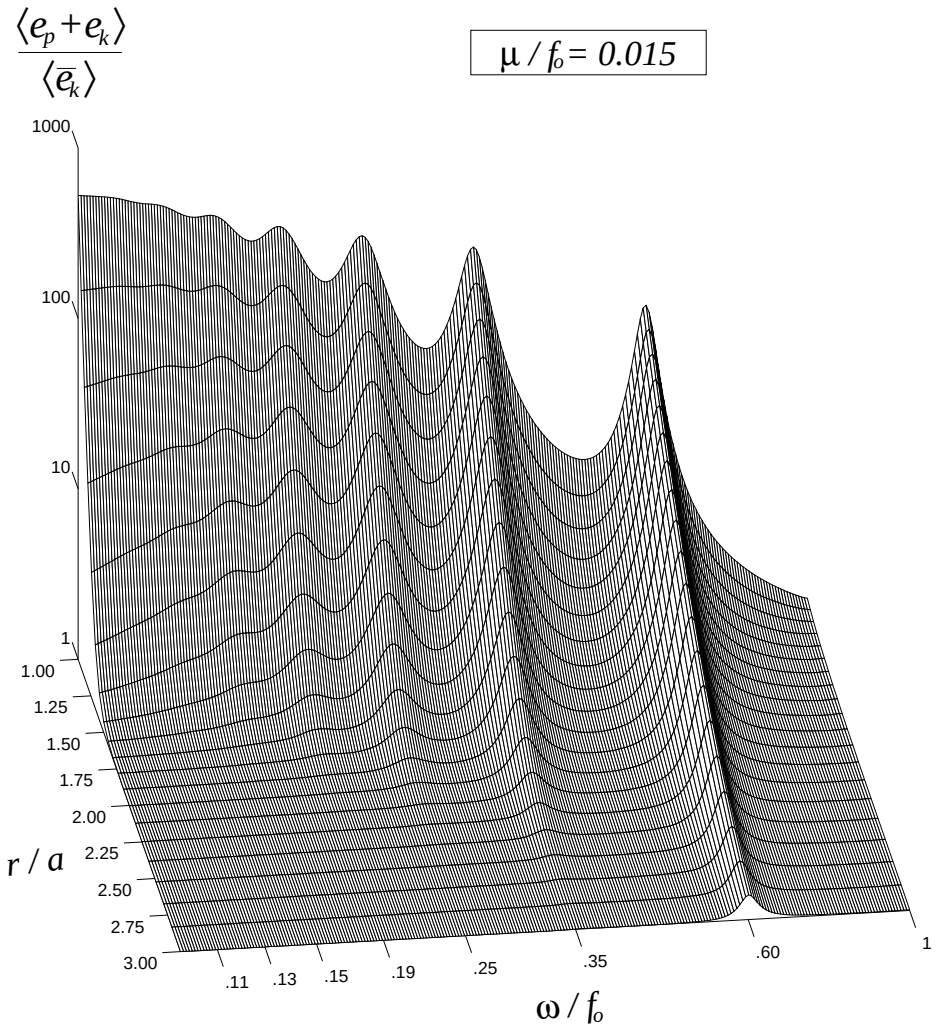

Figure 30: Total mean specific energy divided by mean background specific kinetic energy for the forced island-trapped wave model with dissipation time scale $\mu^{-1} = f_o/0.015$ (≈ 15.8 days). Frequencies from $\omega/f_o = 0.1$ to $\omega/f_o = 1$ (inertial) are shown; tick marks are at the inertial frequency and at the baroclinic eigenfrequencies. The energy ratio is given for radial distance r ranging from the island radius a to $3a$. Note that the trapping scale decreases for increasing baroclinic mode. At the first baroclinic eigenfrequency, the ratio is 78 for $r/a = 1$, composed of 23 parts kinetic and 55 parts potential energy.

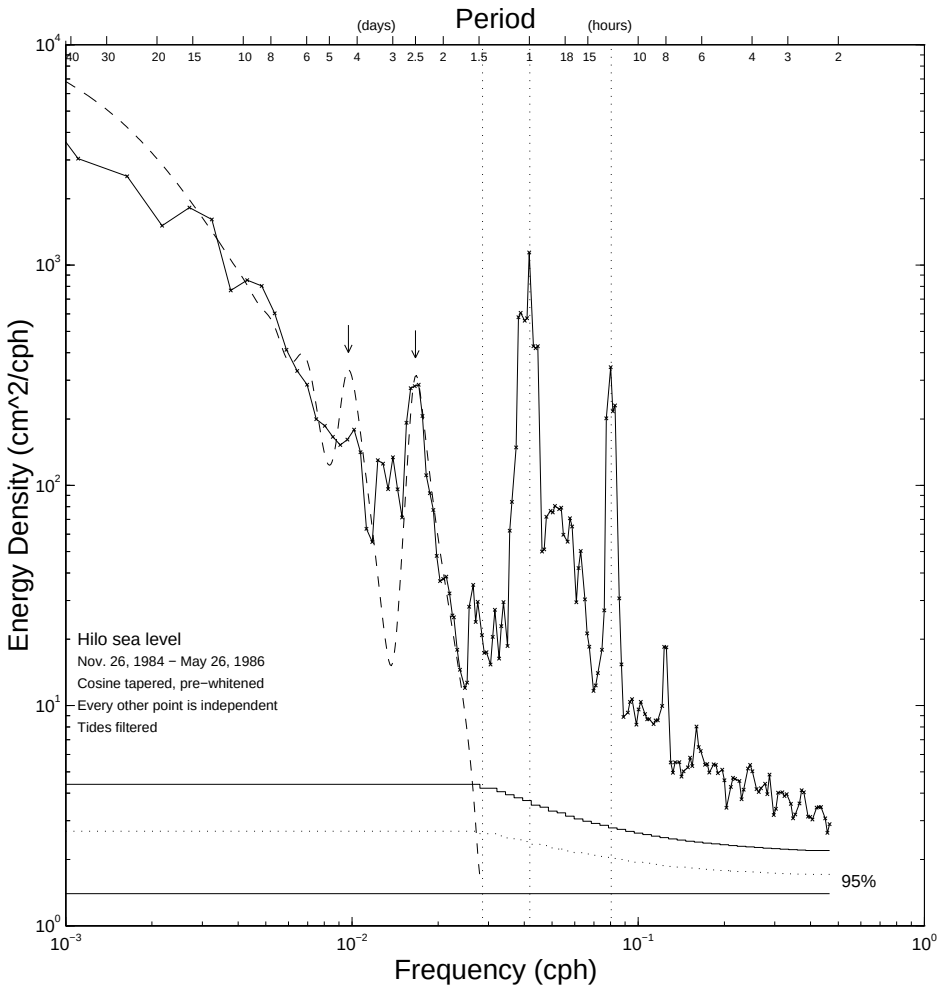

Figure 31: A comparison of Hilo sea level (solid line) with the normalized model mean-square equivalent surface displacement (dashed line). The equivalent depth, dissipation, and normalization constant were chosen to maximize correspondence between the model output and the observed spectral peak at the first baroclinic eigenfrequency (right arrow). The model significantly overrepresents the second baroclinic mode (left arow). The presence of higher azimuthal modes in the data may explain the 3-3.5 day spectral peak.

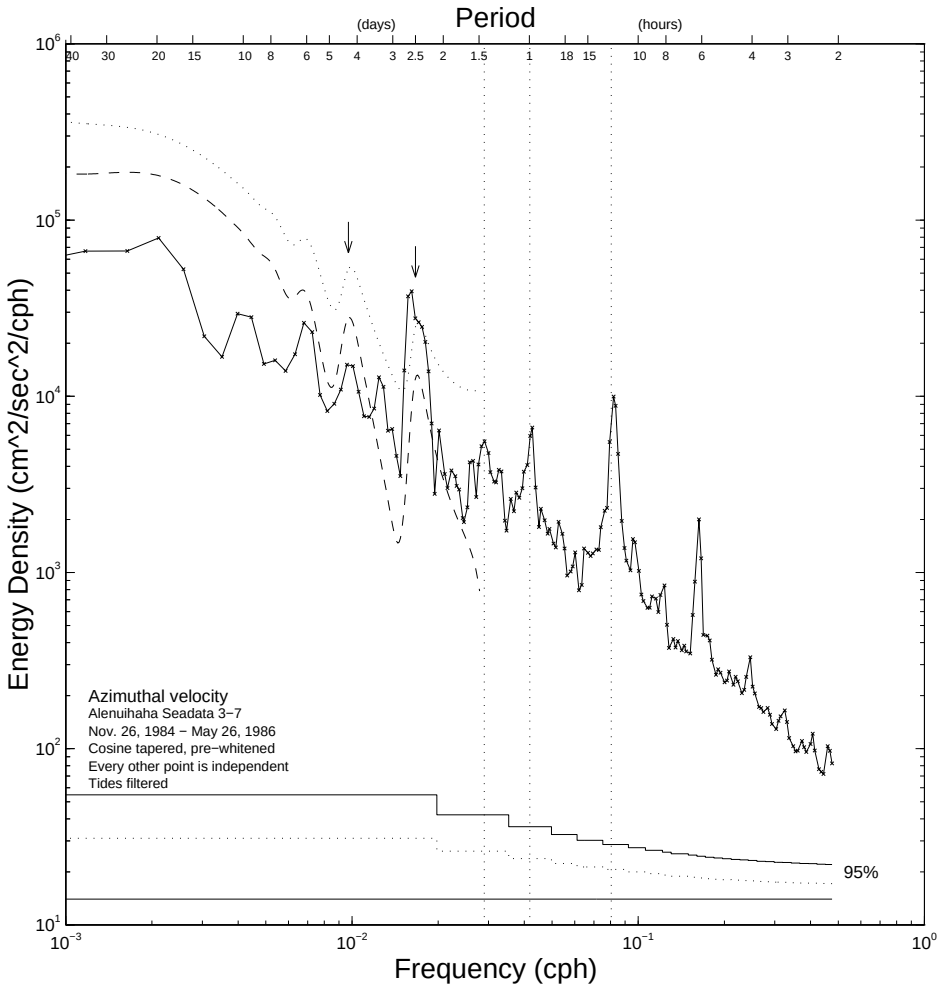

Figure 32: A comparison of azimuthal velocity at the Alenuihaha Seadata site (solid line) with the normalized model mean-square azimuthal velocity at a depth of 50 m (dotted, representing motion within the model mixed layer) and 100 m (dashed, representing motion below the model mixed layer). The model underestimates the spectral density at the first baroclinic eigenfrequency, while overestimating the spectral density at the higher baroclinic eigenfrequencies.

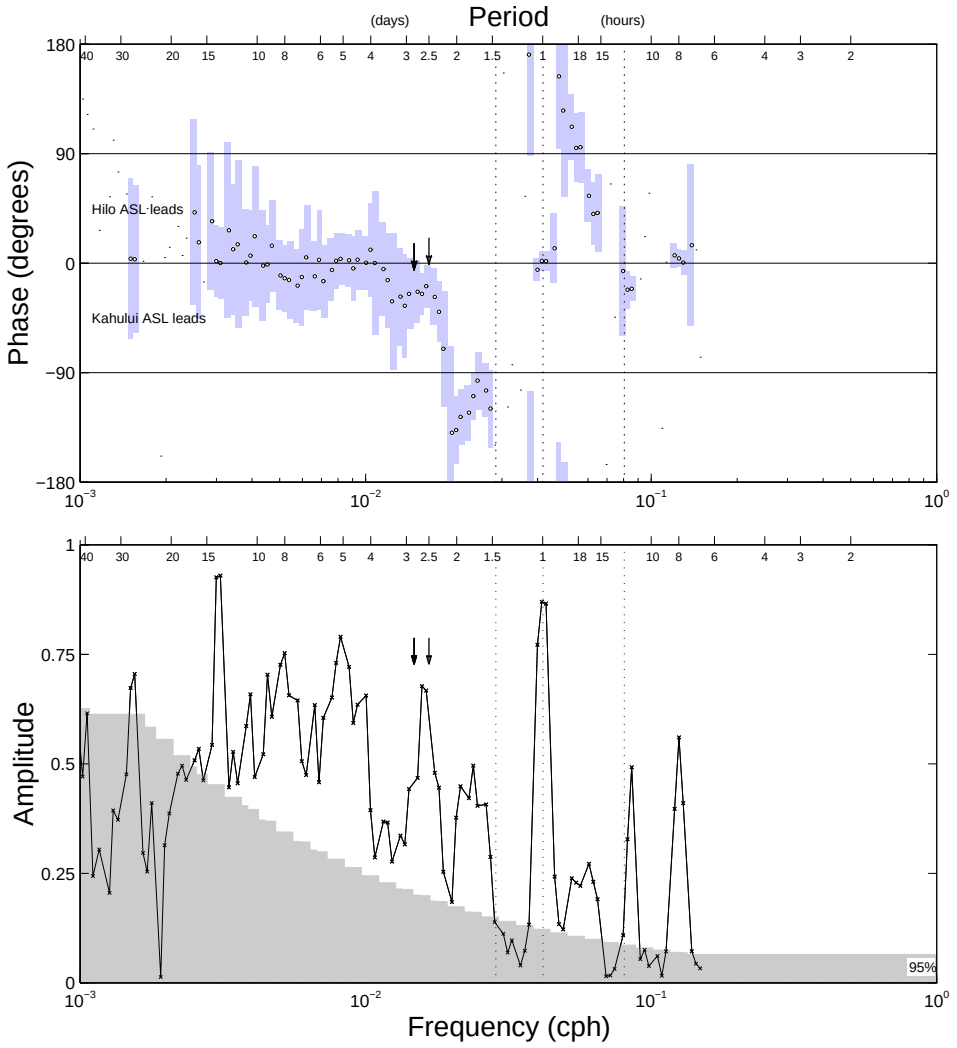

Figure 33: Coherence between Hilo and Kahului ASL, 1966–1974. Vertical lines mark the inertial, diurnal and semidiurnal periods; arrows indicate the theoretical periods of the gravest trapped waves for Hawaii (2.50 days) and the Maui island group (2.82 days). The subinertial coherence peak at 2.56 days period reaches an amplitude of 0.67, with a phase shift of -19° ± 17°. The coherence amplitude in the 1.5 to 2 day band reaches a maximum of 0.50 at 1.74 days period, phase shift -109° ± 19°. Coherence rises above the 95% significance level in the intertidal band, with a peak value of 0.27 at 16.5 h period, corresponding to a phase shift of 56° ± 22°.

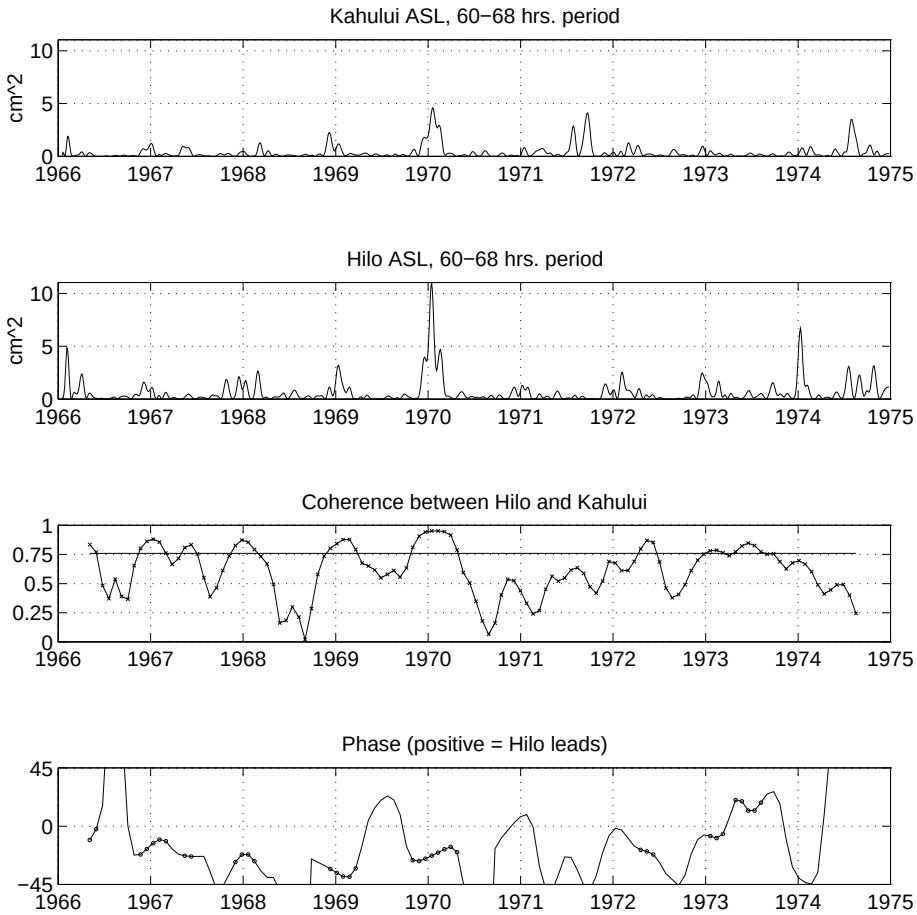

Figure 34: Running coherence amplitude and phase of band-passed ASL at Kahului and Hilo from 2.5 to 2.83 days period. The squared amplitude is plotted for reference; the coherence was calculated from the phase-bearing band-passed signal and not the amplitude envelope. The unchanging line in the coherence amplitude plot indicates the 95% confidence level.

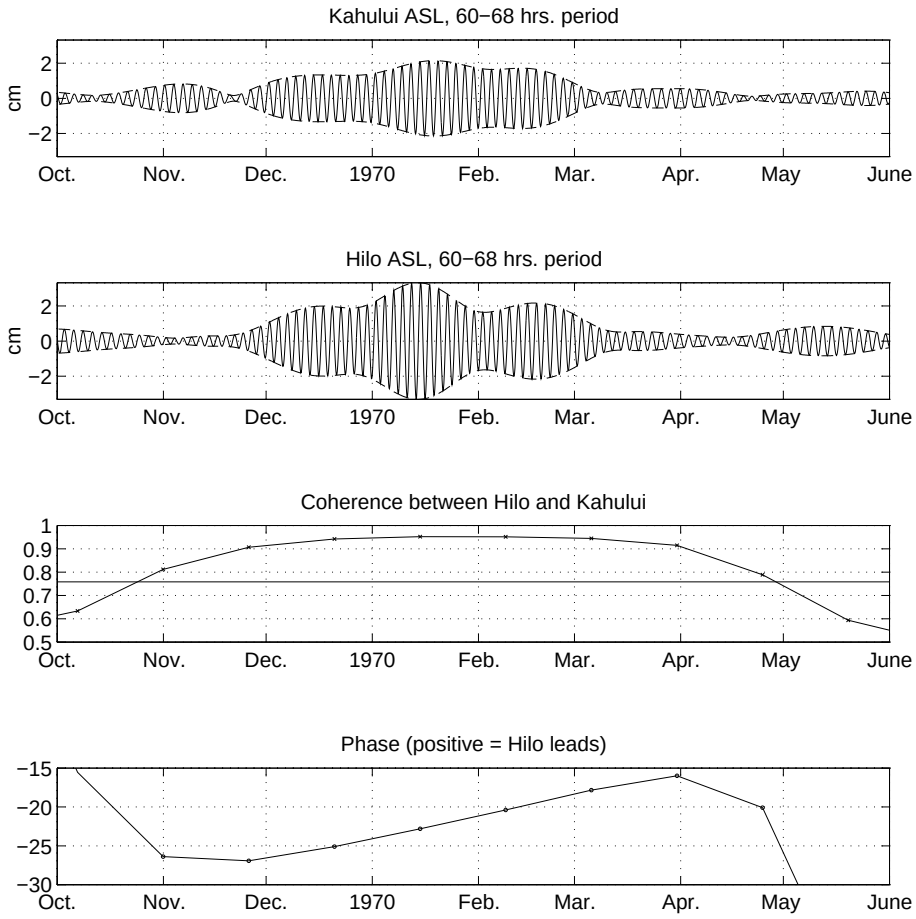

Figure 35: A closeup of the winter of 1969–1970 from the previous figure. The band-passed signals are shown in the top two plots, with dashed lines indicating the amplitude envelope.

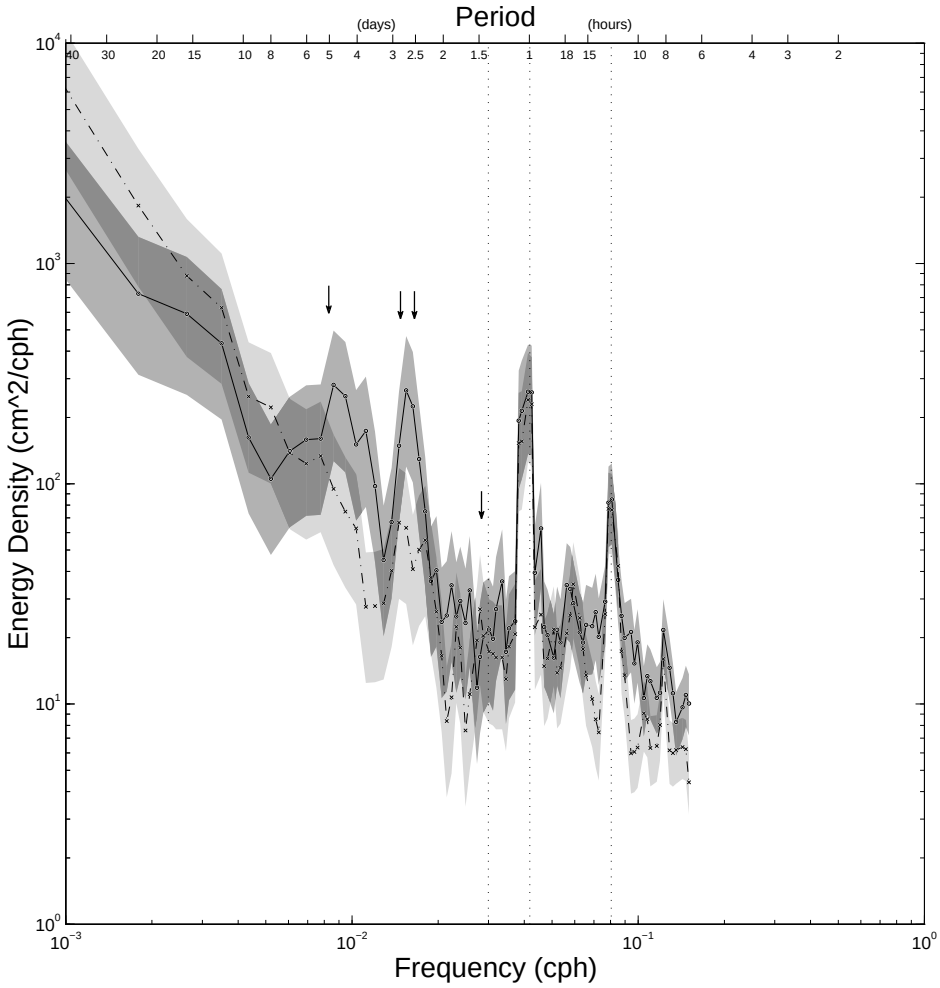

Figure 36: Spectra of Kahului ASL (solid, darker confidence interval shading) and Hilo ASL (dot-dash, lighter confidence interval shading) from 1 April to 1 December 1971. Arrows indicate the theoretical first and second azimuthal, first and second baroclinic trapped wave periods for the Maui island group (see Table 2.1).

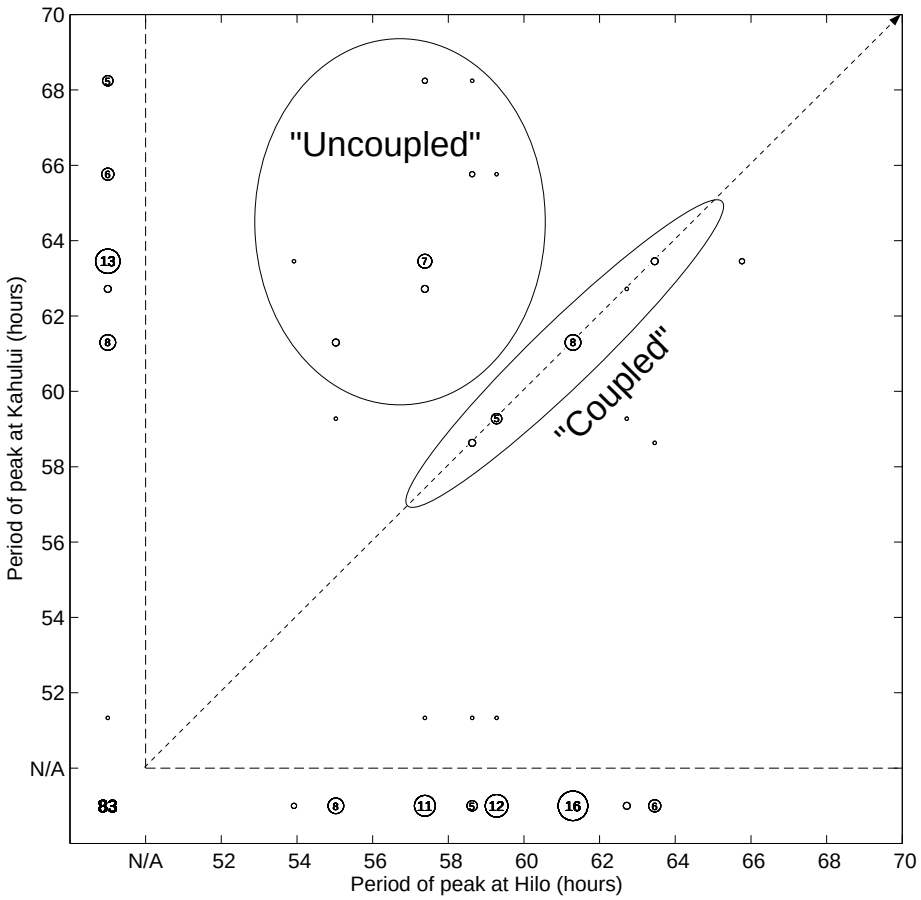

Figure 37: The periods of 52 h (2.17 day) to 70 h (2.92 day) peaks in Hilo ASL vs. those in Kahului ASL, 1966–1974. The circles are proportional in size to the number of observations at that pixel in the period/period array. The number of occurrences is printed if greater than four. Spectra were calculated of subrecords of length 150 days with 15 day overlaps, hanning tapered. Peaks were labeled as "N/A" if the maximum spectral density in the signal band 52-70 h did not rise above the mean density of a "noise" band, 72-90 h, by a factor of 3 (Kahului) or 6 (Hilo). The diagonal dashed line indicates the observations where peak periods are identical in the two records.

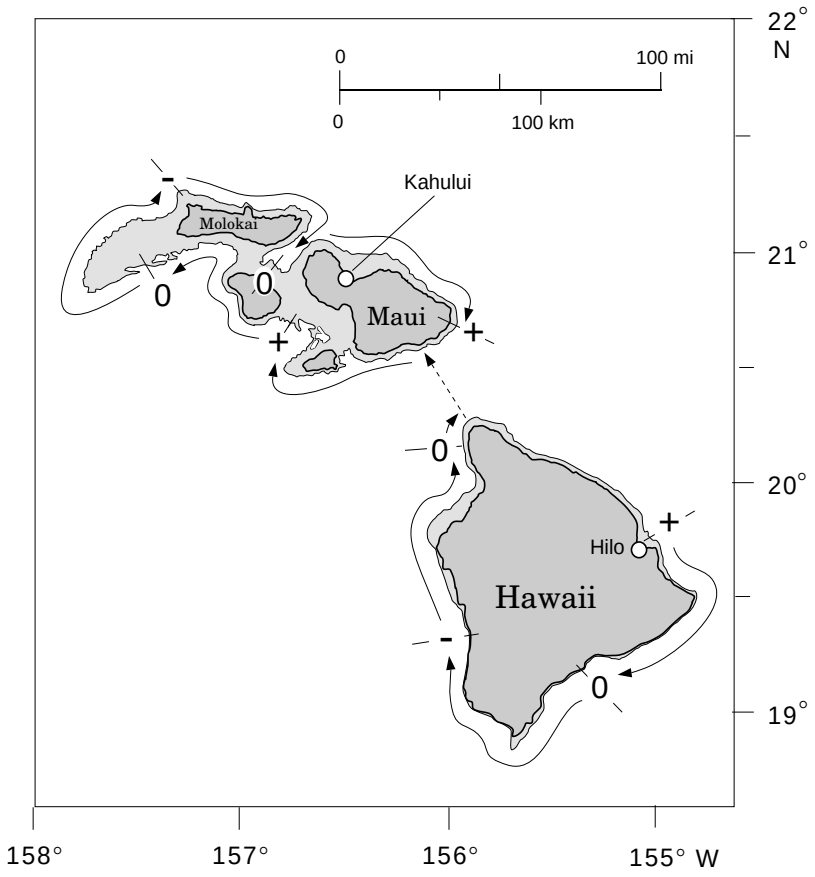

Figure 38: Mapping the phase of a first azimuthal wave of Hawaii onto the Maui island group. The 100 m isobath is shown and used for mapping the ray path. A wavelength is from one + symbol to the next, with 0 indicating 1/4 wavelength and – indicating 1/2 wavelength. Phase does not change in the jump across the Alenuihaha Channel (dotted line), which was arbitrarily chosen at the narrowest point. The Pailolo Channel between Molokai and Maui has been included in the ray path. According to this mapping, Kahului leads Hilo in phase by $\approx$ 35-45°.

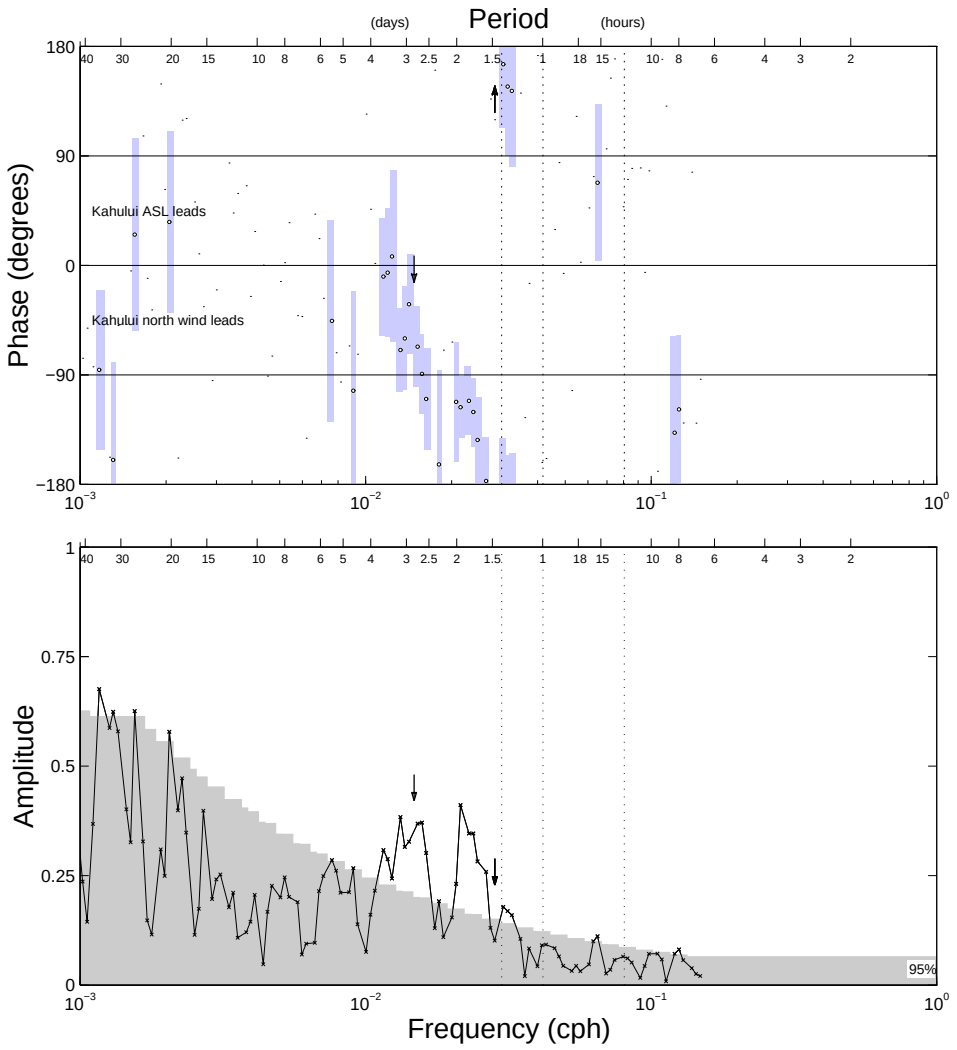

Figure 39: Coherence amplitude and phase between Kahului ASL and north wind at Kahului, 1966-1974. Arrows indicate the theoretical periods of the first (left) and second (right) azimuthal, first baroclinic island-trapped waves for the Maui group. A coherence peak of amplitude 0.37 is at 2.74 days period, with a phase shift of -67° ± 33°. A maximum of 0.41 is at 1.94 days period, phase -116° ± 25°.

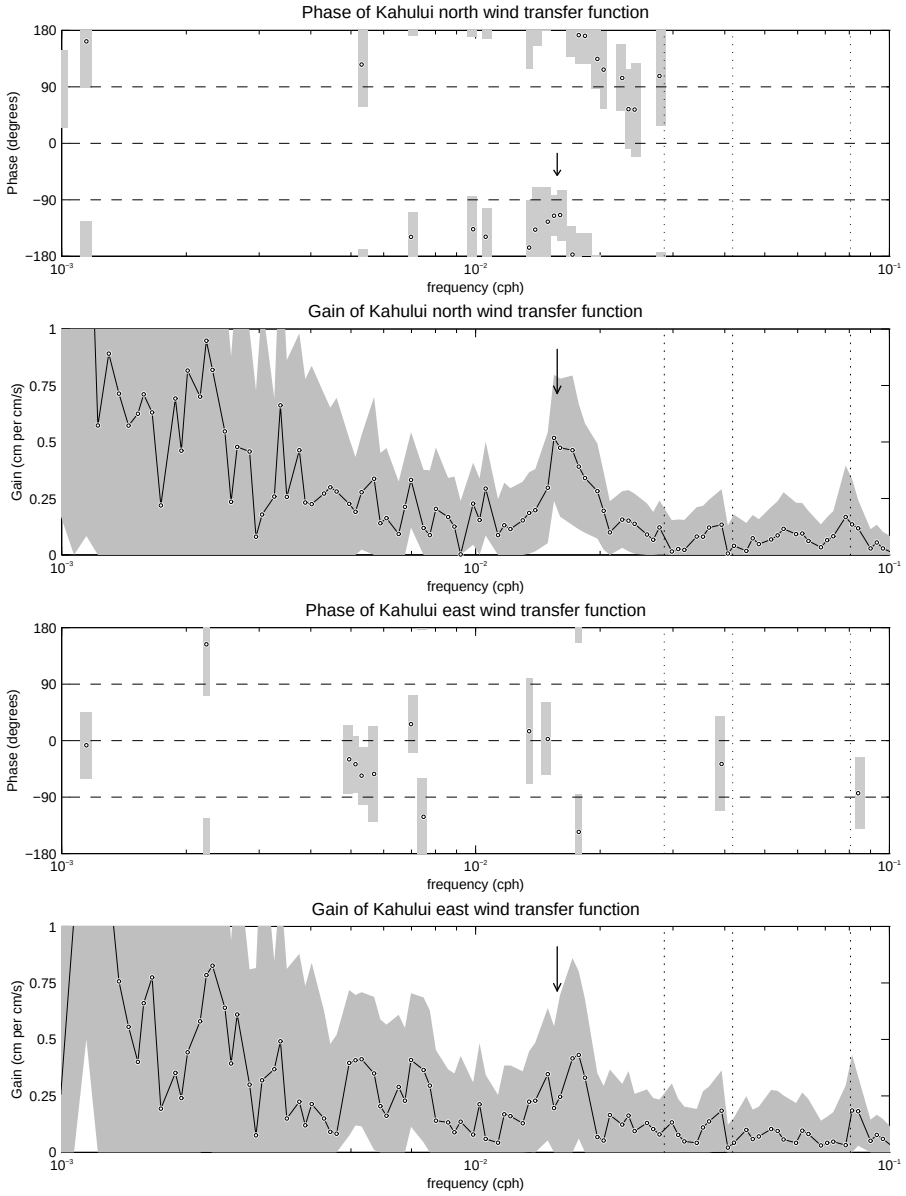

Figure 40: Gain and phase of the transfer functions for the north (top) and east (bottom) winds as determined by the multiple regression described in the text. The observed trapped wave peak in the autospectrum of ASL at Kahului is marked by an arrow. Shading indicates the 95% confidence range for the estimates. Phase is not shown where the error bar spans $(-\pi, \pi)$.

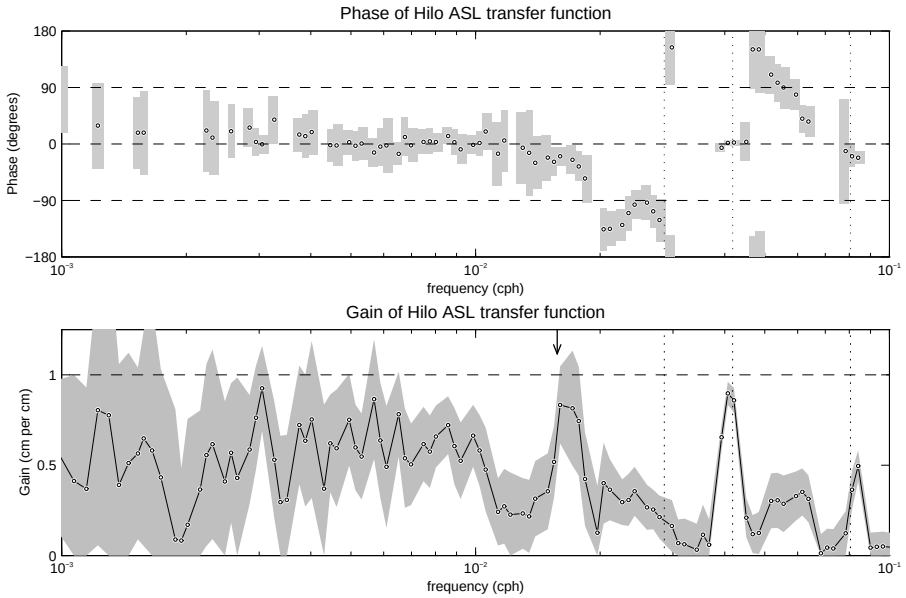

Figure 41: Gain and phase of the transfer function for Hilo ASL (top) as determined by the multiple regression described in the text. The observed trapped wave peak in the autospectrum of ASL at Kahului is marked by an arrow. Shading indicates the 95% confidence range for the estimates. Phase is not shown where the error bar spans $(-\pi, \pi)$.

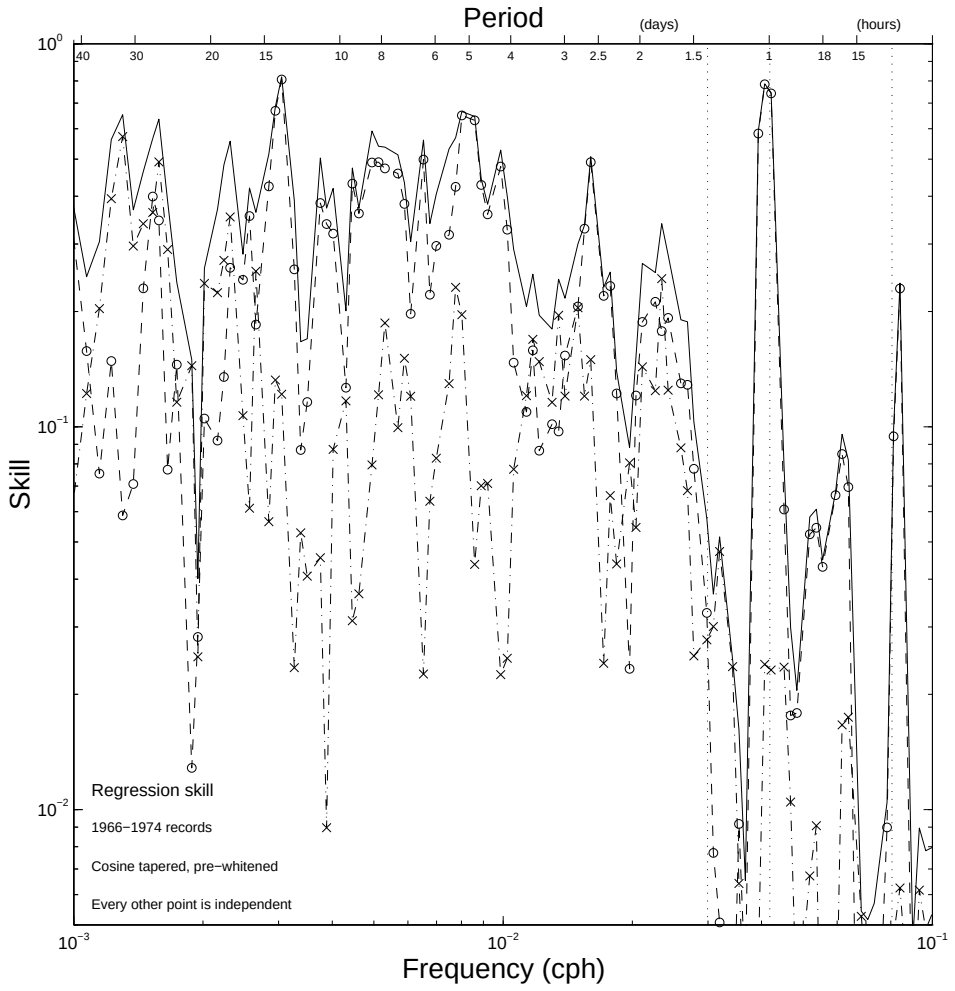

Figure 42: The skill for three linear models of Kahului ASL. The solid line is for the model with Hilo ASL, north wind, and east wind as inputs. The dashed line with circles is for the one-input model, predicting Kahului ASL solely from Hilo ASL. The dot-dash line with crosses is the two-input model, predicting Kahului ASL from the local winds. The skill of the one-input model is close to the skill of the three-input model where remote forcing mechanisms are significant.

Chapter 7

Discussion and conclusions

The dynamical model of the low-mode subinertial trapped waves is consistent with the observations, and reveals the skill with which the actual ray path of a baroclinic Kelvin wave can be mapped onto an equivalent radius for islands of relatively simple geometry [Luther, 1985]. Evidence from current time series such as the Alenuihaha Seadata and Keahole Pt. data sets suggest that a suite of higher-mode trapped waves are also present. A study of the impact of resonant trapped waves on nearshore processes, including residence times of runoff and possible rectification to a mean flow [Luther, 1985], is justified from the magnitude of observed trapped wave currents.

While many hypotheses were proposed for the superinertial oscillations observed in sea level spectra, none were consistent with all observations. It is possible that weak motion which is coherent over large scales is coexisting with superinertial waves trapped (or nearly trapped) to individual Hawaiian Islands. Additional sea level stations have been established throughout the Hawaiian Islands in the last few years; phase information from these stations will certainly clarify our picture of the superinertial motion. The superinertial oscillations remain an enigma, beckoning for a dynamical model consistent with the observations.

With a dynamical picture in hand of the subinertial waves, attention may be turned to such nuances as the balance of remote and local forcing. The model of direct forcing presented in this paper is a first step towards understanding the generation of resonant coastal waves. The next generation of models must address complications such as sloping island flanks, azimuthal asymmetries in the island geometry, and asymmetries in the wind field. Furthermore, the observed event-like nature of the trapped waves must be

addressed. For example, how would the model respond to an impulse rather than a steadily-applied wind field? How would resonant peaks at the natural periods of the system be established under these circumstances?

Remote forcing may play a role in generating some of the variance of the trapped wave at Hilo, but leakage from Hawaii to the Maui group seems to be the dominant forcing mechanism for the spectral peak observed at Kahului. However, in the mean spectra of Kahului sea level, the spectral peak lies near the Maui group's natural period (2.6 days) rather than Hawaii's gravest mode trapped wave period (2.5 days). This suggests that leakage between these islands is particularly effective due to co-resonance. Hawaii is more effectively "rung" by direct forcing, presumably due to its simple geometry. Following this excitation, the physical proximity of Maui (closer than the trapping scale of the coastal wave) allows energy to leak across the Alenuihaha Channel and generate resonant waves around the Maui group. A study of leakage between other Hawaiian Islands goes beyond the scope of this work, but may resolve issues such as the importance of co-resonance in determining the efficiency of leakage.

Other forcing mechanisms were not considered in this work, yet are promising topics for future investigation. For example, LUTHER [1985] suggested that surface waves may generate coastal waves through set-up/set-down of the thermocline; an array of buoys are currently recording swell around the Hawaiian Islands and may be used to test this hypothesis.

Appendix A

Currents around the Hawaiian Islands

Currents around the Hawaiian Islands are examined in several frequency bands, from the mean flow field to semidiurnal motion. Special attention is given to the bands containing subinertial trapped waves and the superinertial sea level oscillations discussed in Chapter 5.

A.1 Introduction

In parallel with the trapped wave study presented in the main body of this paper, an analysis of several Hawaiian current data sets was conducted in order to ascertain the tidal, intertidal, subinertial and mean flow fields. A discussion of the current meter sites appears in Section 3.3; the location, depth, deployment dates and types of meters are summarized in Tables 3.2 and 3.3.

Examination of four frequency bands was conducted by a principle component analysis of band-passed signals in order to determine the direction and magnitude of the semimajor and semiminor axes of the current ellipses. Band-passing was performed with a five-point Butterworth IIR filter and the Matlab routine *filtfilt*. The frequency bands examined in this report are:

Frequency band	Minimum period (h)	Maximum period (h)
Semidiurnal	11	13
Intertidal (wide)	14	20
Intertidal (tight)	17	19
Diurnal	22	26
Near-subinertial	(IP)	72

(IP = inertial period). For this analysis, the tidal frequency bands still contained the phase-locked signal; the intertidal and near-subinertial bands were included due to their possible significance in the dynamics of resonant coastal waves [Luther, 1985].

The eccentricities of the current ellipses for each band, given by

$$e = \sqrt{1 - b^2/a^2} \tag{A.1}$$

where a and b are the magnitudes of the semimajor and semiminor axes, are summarized in Table A.1.

Table A.1: Mean eccentricities of the current ellipses in several frequency bands. The eccentricity is zero for a perfect circle and approaches 1 as the motion becomes linearly polarized.

	Frequency band				
Site	Semi-diurnal	Intertidal (wide)	Intertidal (tight)	Diurnal	Near-subinertial
OTEC-1 Keahole Pt.	.82	.61	.59	.79	.79
DUMAND	.87	.54	.61	.50	.55
Alenuihaha Seadata	.99	.88	.86	.95	.96
Lanai	.75	.54	.61	.72	.56
OTEC-4 Kahe Pt.	.80	.51	.54	.72	.56
TRW OTEC-2 Kahe Pt.	.93	.77	.79	.89	.81
MEAN:	.89	.70	.71	.82	.76

A.2 Subinertial currents

A.2.1 Resulting drift

From 1964 to 1969, Wyrtki *et al.* [1969] deployed an extensive array of paddle-wheel and Geodyne 850 current meters around the Hawaiian Islands. The meters collected data for short intervals (typically 15 to 30 days), mostly in shallow water near an island.

Wyrtki *et al.* [1969] expected to find evidence of Ekman-driven flow in the channels separating the islands; to their surprise, they found mean currents which in some cases were in the opposite direction to the prevailing trade winds. Later analysis [Patzert and Wyrtki, 1974] suggested that a mean clockwise flow exists around each of the major Hawaiian Islands. Patzert and Wyrtki [1974] believed this may result from rectification of tidal currents; Luther [1985] suggested that rectification of the clockwise-

propagating trapped waves could yield the observed low-frequency currents. At the Alenuihaha Seadata site, there is little visual correlation between the amplitude of the low frequency currents and currents in the trapped wave band (Fig. 43). However, there is also not a strong correlation between the currents in the M_2 band and the mean flow (although the maxima of both records occur at roughly the same time).

The resulting drift observed at all current meter sites is displayed in Fig. 44 (solid lines). For comparison, dashed lines show the mean flow deduced by WYRTKI *et al.* [1969]. A mean clockwise pattern around Oahu and Hawaii is suggested by the Noda and DUMAND time series. All data reveal a more complicated pattern around and between the Maui group of islands. While the magnitude and direction of the drift varies with depth and season, all of the time series collected near the island of Hawaii (except the 771 m Aanderaa at the Keahole site) indicate a mean current in the clockwise direction. Much more variability may be observed in the Oahu data sets, although the general clockwise trend is discernible.

A.2.2 Near-subinertial band

Currents in the near-subinertial band lie along the local bathymetry in all cases except for the Lanai mooring S4 (Fig. 45, 46). The eccentricities of the current ellipses in this frequency band are greater than or equal to those in the diurnal band except at the Lanai and Kahe Pt. sites. The eccentricities are greater than 0.7 at all sites except DUMAND, Lanai and the OTEC-4 Kahe Pt. moorings, all of which were in operation during summer and autumn months.

This frequency band contains the seasonal baroclinic trapped waves seen by LUTHER [1985] in sea level data at several Hawaiian stations. A high priority of this study was identifying island-trapped waves in current measurements; thus the principle component analysis of this frequency band was used to define the azimuthal (alongshore) and radial

(offshore) coordinate system.

The currents in this band reached $O(50)$ cm/s in the winter of 1984–1985 at the Alenuihaha Seadata site (see Fig. 43), indicating the influence trapped waves can have on the flow field around the islands.

A.3 Superinertial currents

LIEN [1985] examined the counter-clockwise to clockwise energy ratio for the OTEC-4 Kahe Pt. mooring and found that the consistency relation matched the observed energy ratio at frequencies higher than semidiurnal, while the observed ratio approached unity in the inertial through semidiurnal band. For the other sites examined in this study, the consistency relation holds well for motion relatively far from the island flanks such as at the DUMAND site (Fig. 47). The consistency relation becomes less accurate as the island flanks are approached and the motion becomes polarized in the alongshore direction (Fig. 48). At all sites, CW energy dominates the superinertial spectra or the motion is oriented nearly back-and-forth.

A.3.1 Diurnal band

Diurnal currents trace ellipses with eccentricities between those of the semidiurnal and the intertidal signals (Fig. 49, 50). The diurnal currents' semimajor axes are less than 4 cm/s except in the energetic Alenuihaha Channel. These magnitudes are smaller than those of the WYRTKI *et al.* [1969] study by a factor of 2 to 4, presumably due to the shallower deployment of the meters in that study. The orientation of the semimajor axes are very similar between the Wyrtki *et al.* study and this one.

A.3.2 Intertidal bands

Intertidal currents are much weaker than those in the other frequency bands. The semimajor axes lie along the local bathymetry in most cases, but the ellipses are in all

cases more nearly circular than in any other band (Fig. 51, 52).

A tighter bandpass covering periods of 17 to 19 hours does not reveal motion which is more eccentric than the "wide" intertidal band ellipses (Fig. 53, 54).

An excess of counter-clockwise rotary energy appears in the Keahole Pt. spectrum at periods of 7 h and 15 to 17 h (Fig. 48). These anomalies are strongest at the shallowest (54 m) instrument and become progressively weaker as the depth increases. Such departures from the internal gravity wave consistency relation may indicate the presence of motion with dynamics differing fundamentally from freely propagating baroclinic waves. However, as noted by LIEN [1985], the consistency relation (3.3) does not hold in the presence of external forcing. A spectrogram of the azimuthal velocity (see Fig. 18) suggests that direct forcing occurred along a wide band of frequencies, possibly resulting in the observed anomalies.

A.3.3 Semidiurnal band

Currents in the semidiurnal band are the strongest and most highly polarized of the bands examined here (Fig. 55, 56). Least-squares tidal filtering reveals that a large amount of the variance in this band is at the M_2 frequency.

Semimajor axes of the diurnal current ellipses are oriented roughly alongshore. Three of the five Keahole Pt. ellipses are oriented nearly onshore, as are some of the Kahe Pt. ellipses. The currents are weaker (by a factor of 1.5 to 2) than those measured by WYRTKI *et al.* [1969]. As in the diurnal band, this is presumably due to the shallow deployment of the meters in the Wyrtki *et al.* study. The orientation of the semimajor axes in the Wyrtki *et al.* study were generally closer to alongshore than those shown in Figs. 55 and 56.

A.4 Conclusions

PATZERT AND WYRTKI's [1974] conclusion that a mean clockwise flow exists around Oahu and Hawaii is supported by the Noda and DUMAND data sets, although considerable variations in the resulting drift off Kahe point indicate that the CW pattern is only a rough picture of the low-frequency motion around Oahu. The source of this mean flow pattern is not obvious from a casual examination of the semidiurnal and trapped wave frequency bands.

There is no strong evidence of topographically-associated motion in the intertidal band containing the sea level oscillations discussed in Chapter 5. If such currents exist, they may be masked by the noise level of the inertia-gravity background. Alternatively, this motion may be very tightly trapped to the topography.

There are many features left to explore in these data for the intrepid researcher. As an example, no attention was given to near-inertial internal gravity waves or quasi-geostrophic eddies. The tentative conclusion that a clockwise flow exists around Oahu may be more rigorously tested by the vast number of Kahe Point OTEC data sets; future work may involve calculating a theoretical rectified flow from observed tidal and subinertial motion [LONGUET-HIGGINS, 1970] and comparing this to the observed low-frequency currents. The greatest strength of the Noda data sets is their temporal coverage at a few sites, rather than the spatial coverage emphasized by Figs. 44– 46. A future study of the seasonal and interannual variability in the currents, particularly in the "mean" currents presented in Fig. 44, would expand the present understanding of low-frequency motion near prominent topography.

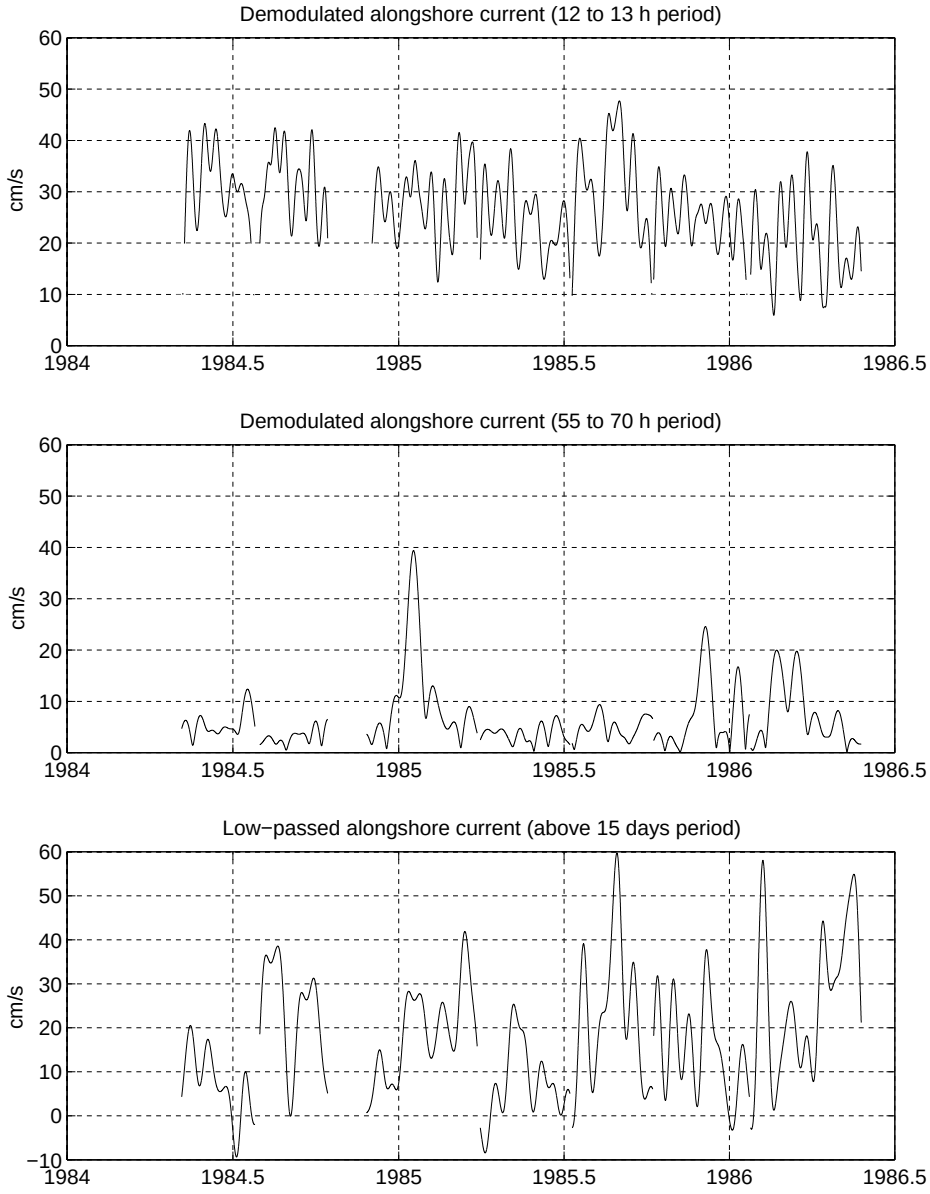

Figure 43: Alongshore currents at the Alenuihaha Seadata site. Top: currents in the semidiurnal band (12 to 13 h period). Center: currents in the gravest trapped wave band (55 to 70 h period). Bottom: low-passed (mean) current. Gaps occur during servicing of the Seadata instrument.

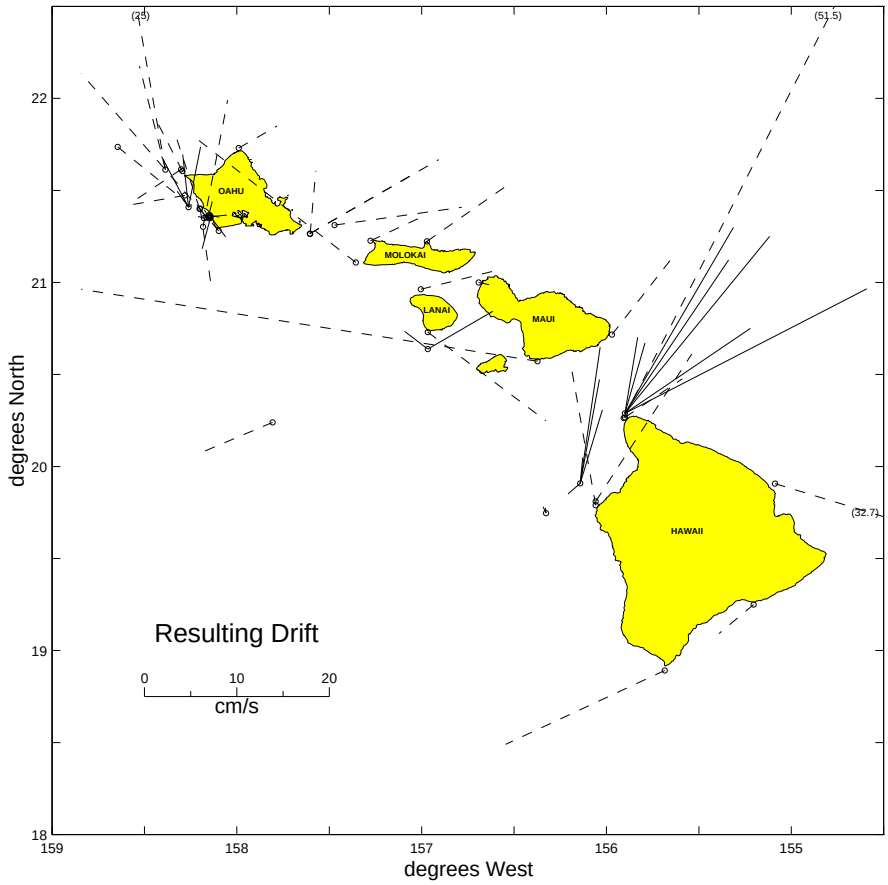

Figure 44: Resulting drift observed at the Noda and UH sites (solid lines) and by Wyrtki *et al.* [1969] (dashed lines).

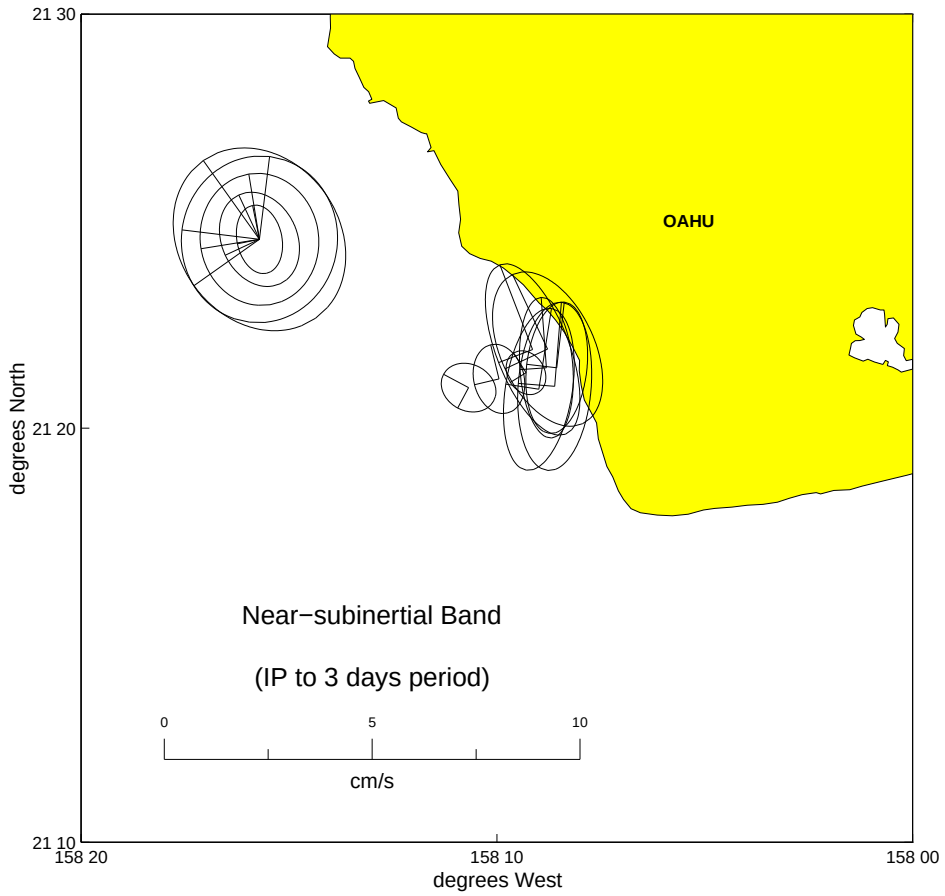

Figure 45: Current ellipses of the near-subinertial motion (inertial to three days period) at the OTEC-4 and TRW OTEC-2 Kahe Pt. sites.

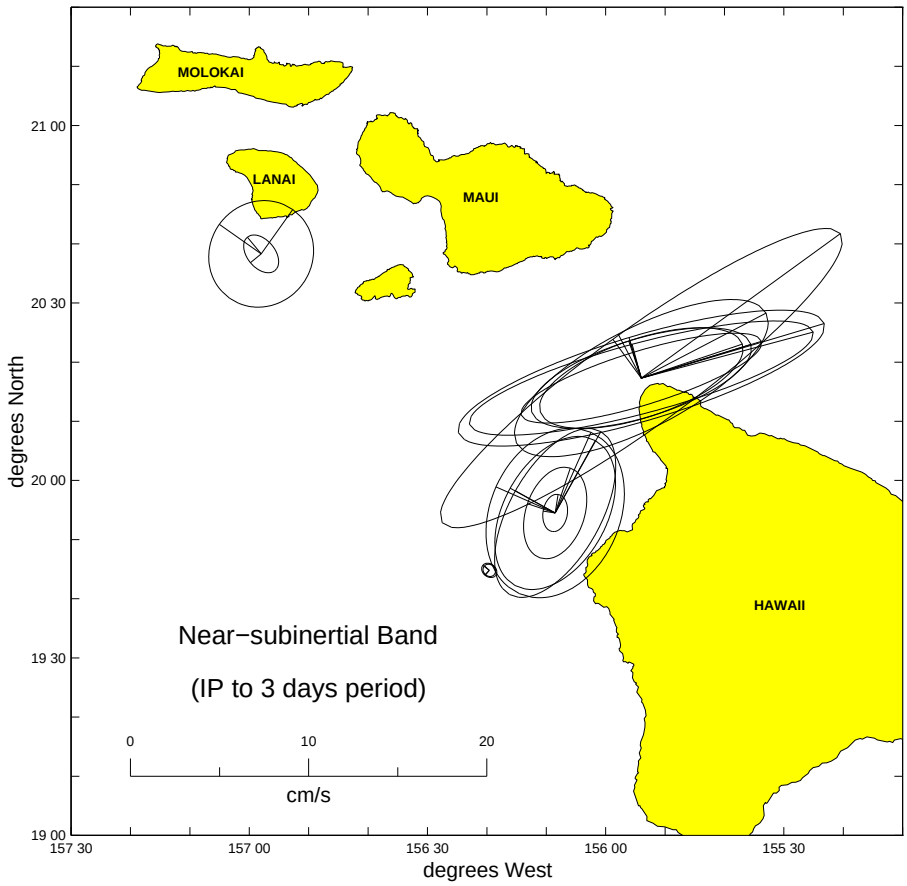

Figure 46: Current ellipses of the near-subinertial motion (inertial to three days period) at the DUMAND, OTEC-1 Keahole Pt., Alenuihaha Seadata and Lanai sites.

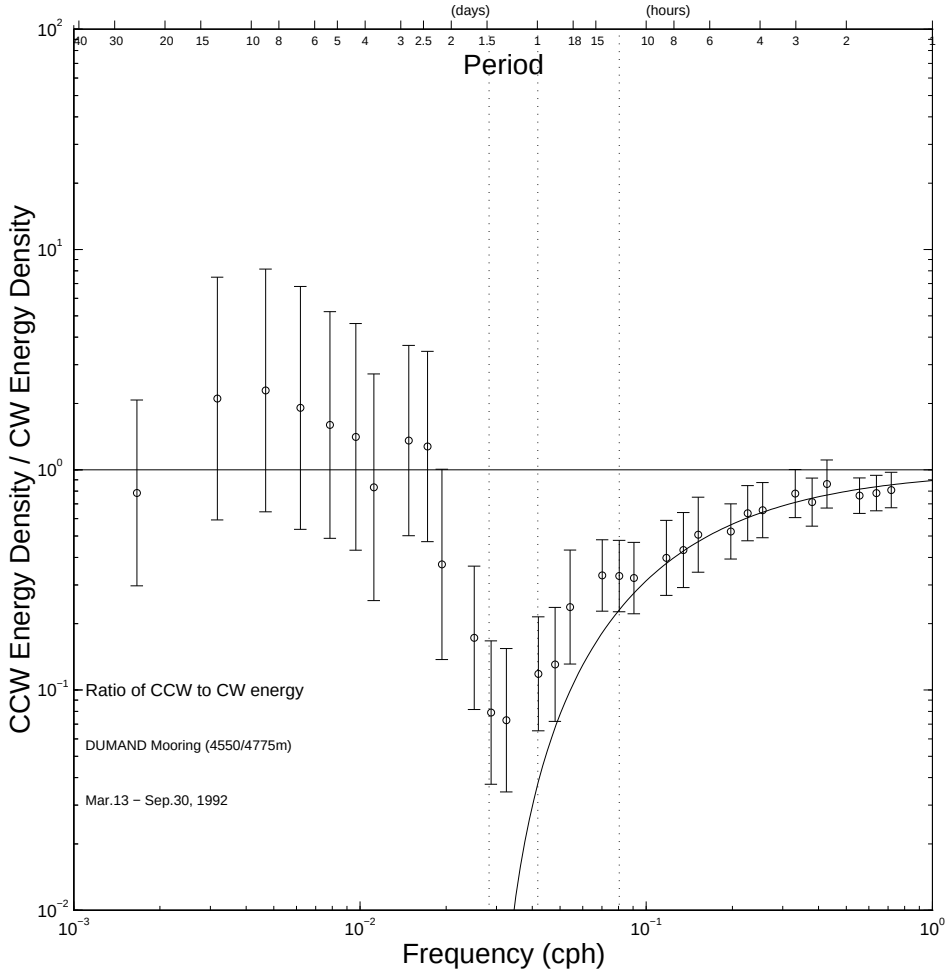

Figure 47: The ratio of counter-clockwise to clockwise energy at the DUMAND mooring 4550 m Aanderaa. Error bars indicate the 95% confidence interval. The solid line gives the theoretical consistency relation for freely-propagating internal gravity waves in a horizonally unbounded fluid; see (3.3).

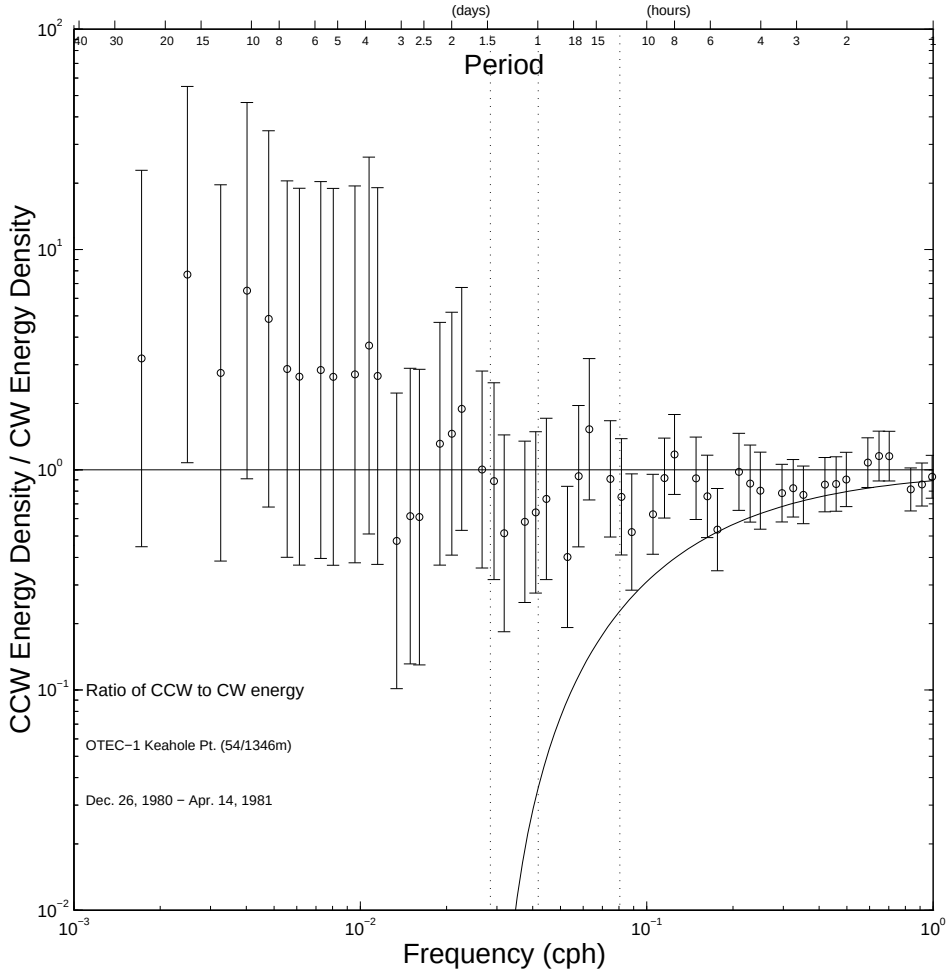

Figure 48: The ratio of counter-clockwise to clockwise energy at the Keahole Pt. 54 m Aanderaa. Error bars indicate the 95% confidence interval. The solid line gives the theoretical consistency relation for freely-propagating internal gravity waves in a horizonally unbounded fluid; see (3.3).

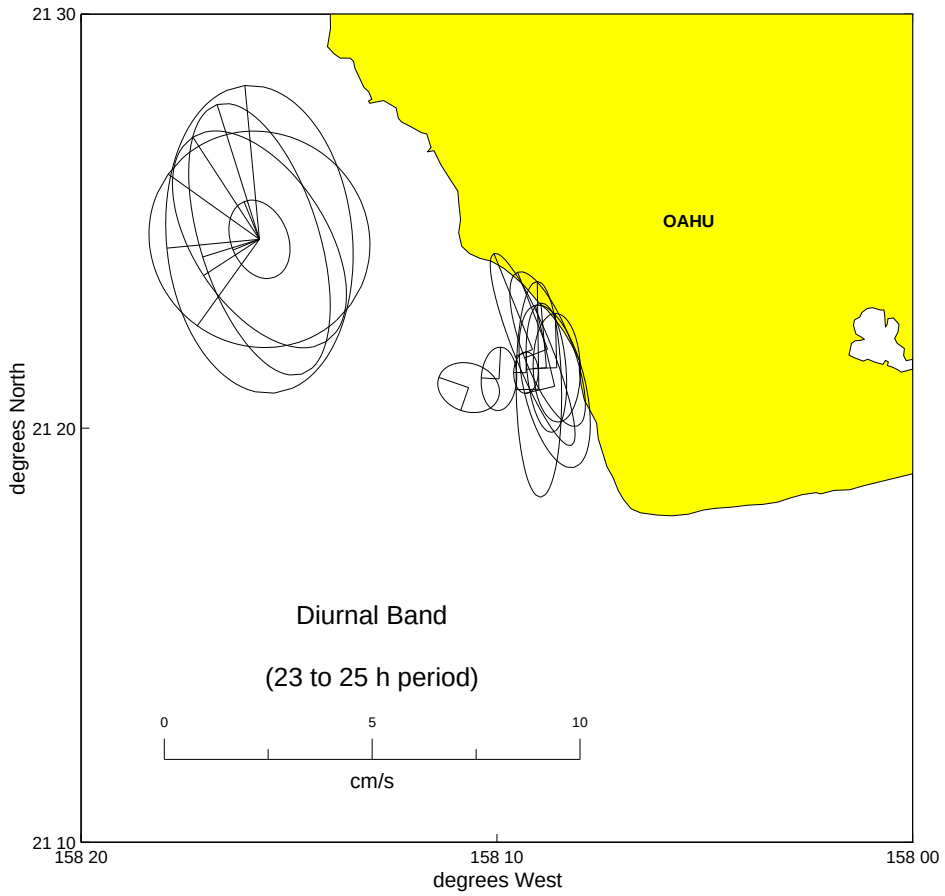

Figure 49: Current ellipses of the diurnal motion (23 to 25 h period) at the OTEC-4 and TRW OTEC-2 Kahe Pt. sites.

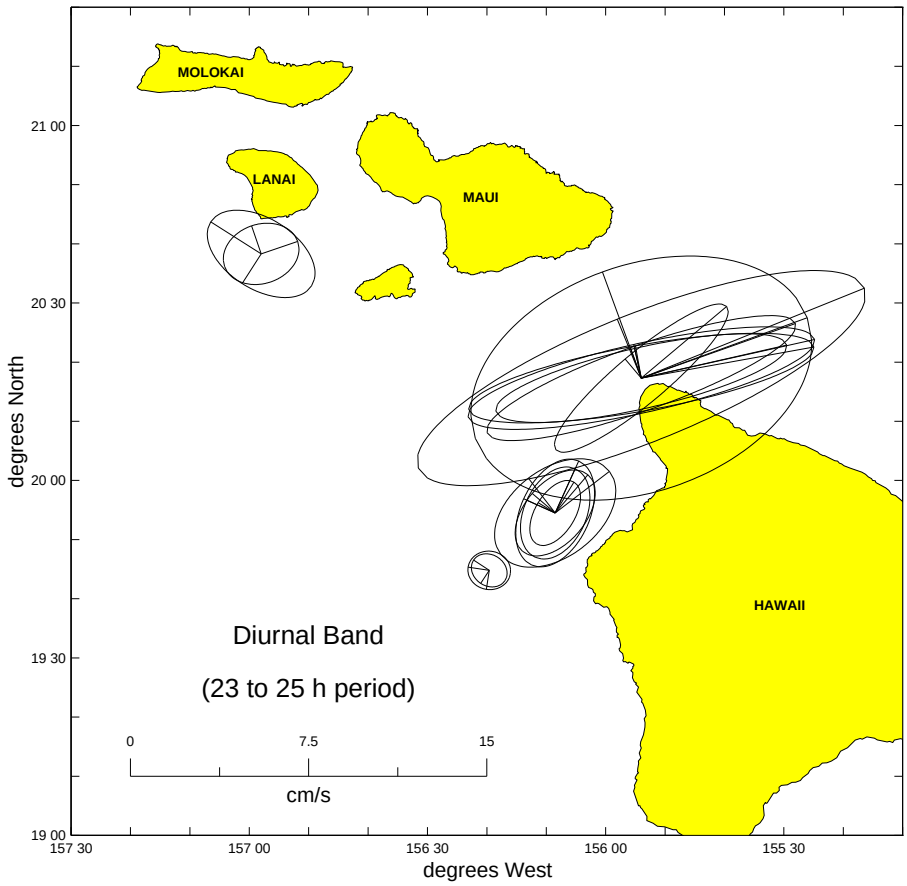

Figure 50: Current ellipses of the diurnal motion (23 to 25 h period) at the DUMAND, OTEC-1 Keahole Pt., Alenuihaha Seadata and Lanai sites.

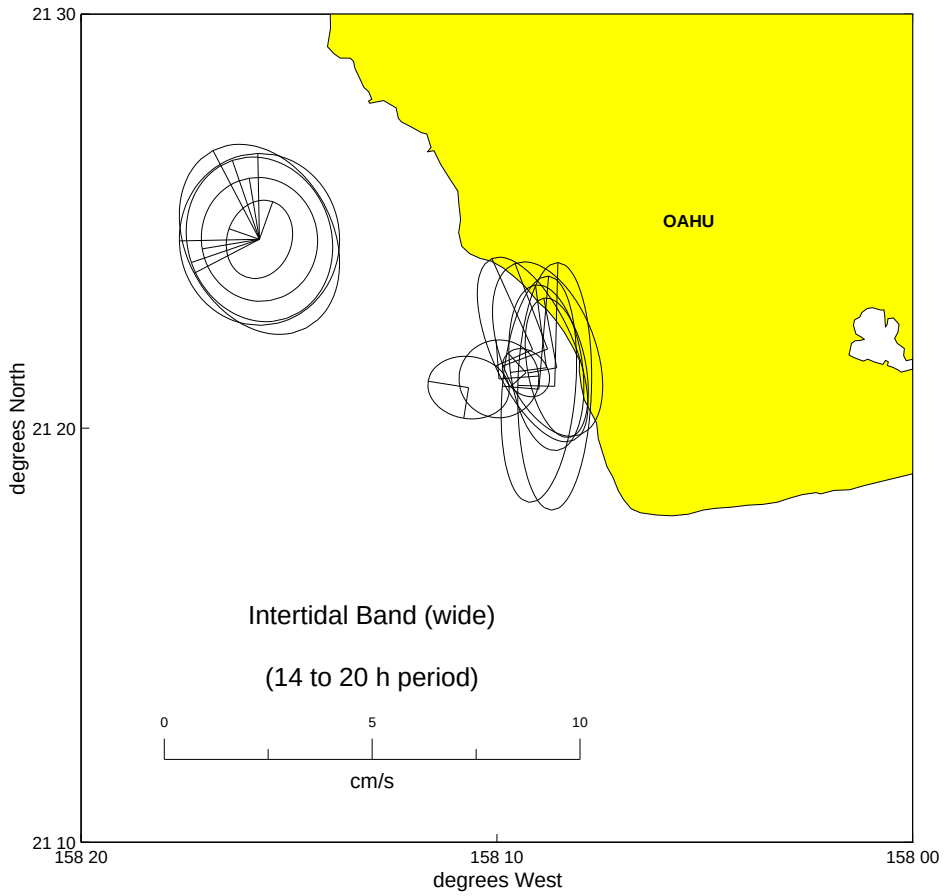

Figure 51: Current ellipses of the intertidal motion (14 to 20 h period) at the OTEC-4 and TRW OTEC-2 Kahe Pt. sites.

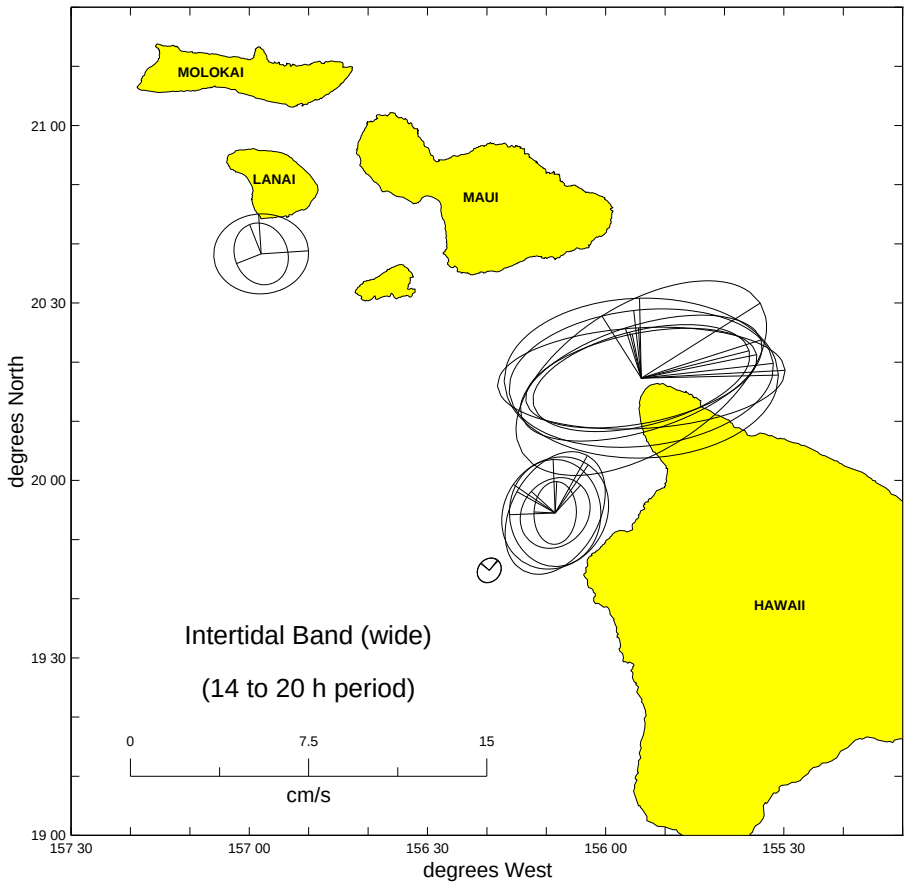

Figure 52: Current ellipses of the intertidal motion (14 to 20 h period) at the DUMAND, OTEC-1 Keahole Pt., Alenuihaha Seadata and Lanai sites.

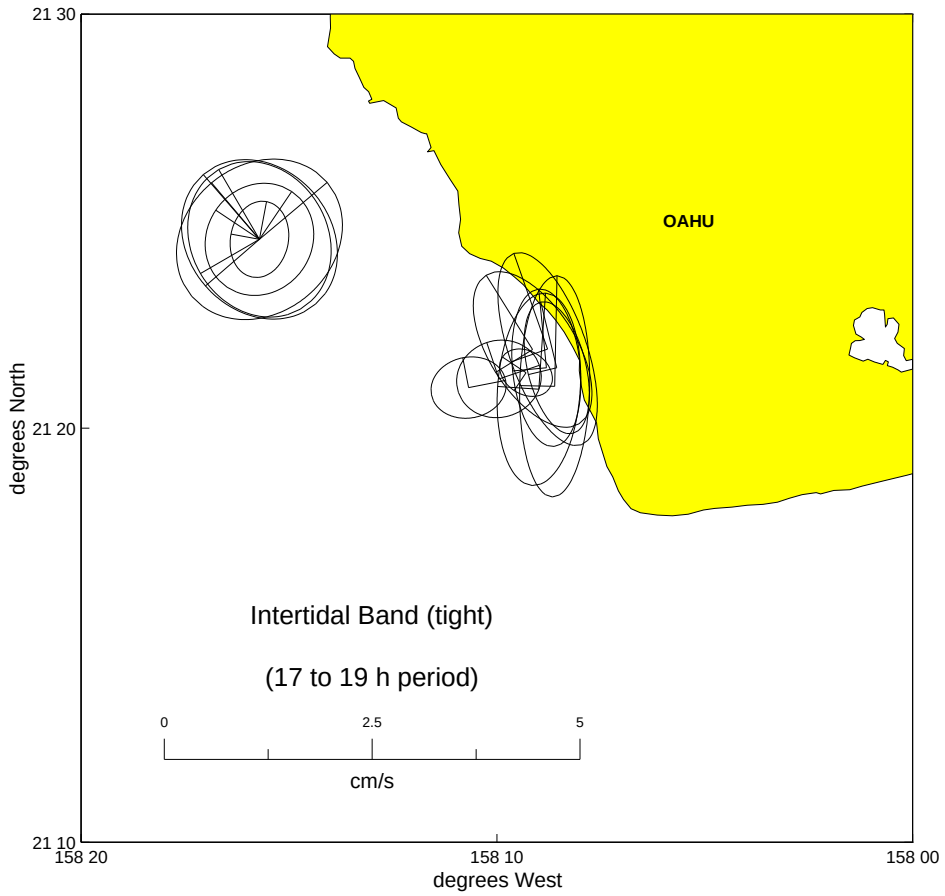

Figure 53: Current ellipses of the intertidal motion (17 to 19 h period) at the OTEC-4 and TRW OTEC-2 Kahe Pt. sites.

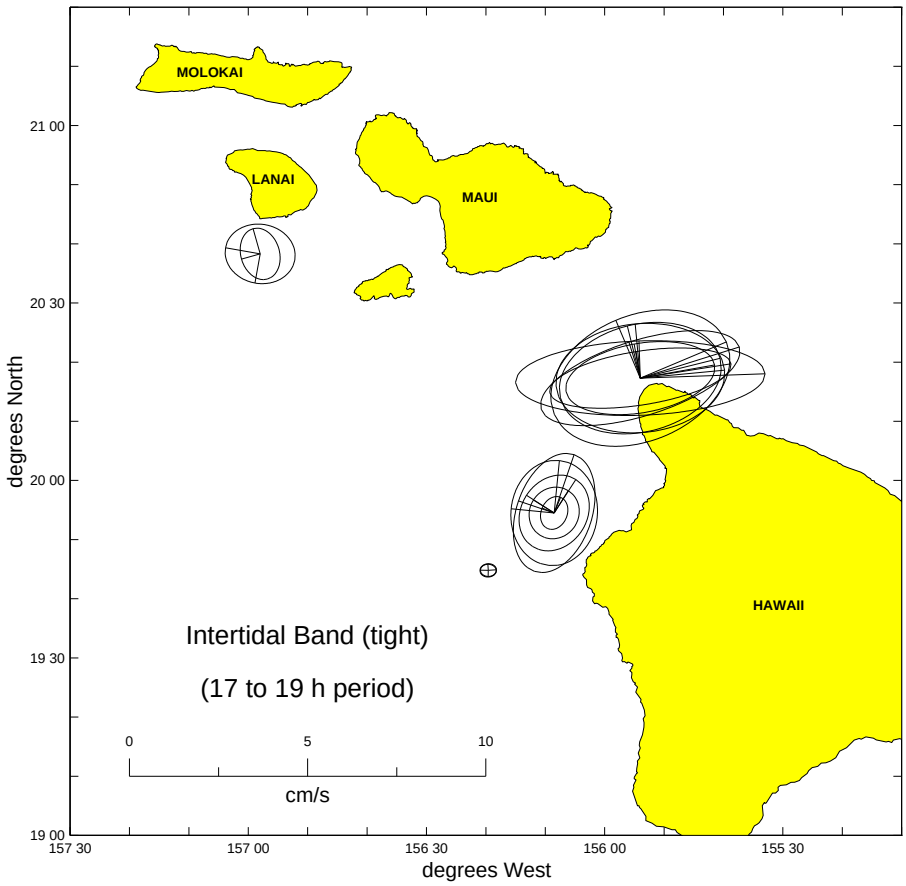

Figure 54: Current ellipses of the intertidal motion (17 to 19 h period) at the DUMAND, OTEC-1 Keahole Pt., Alenuihaha Seadata and Lanai sites.

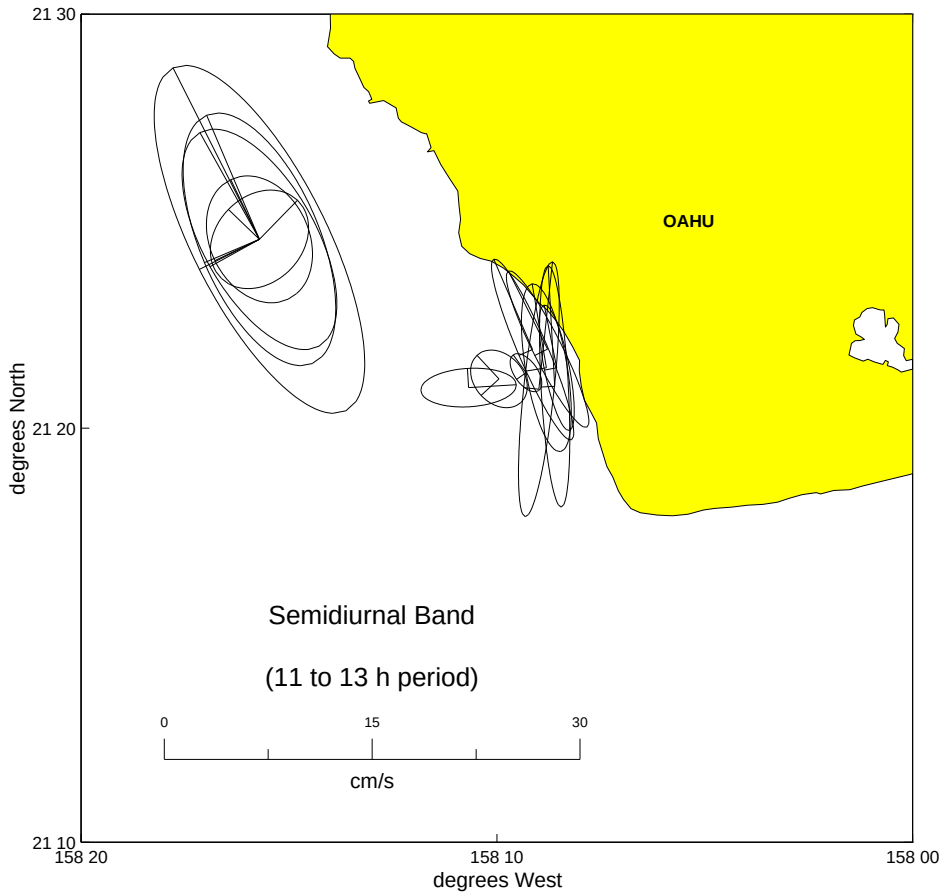

Figure 55: Current ellipses of the semidiurnal motion (11 to 13 h period) at the OTEC-4 and TRW OTEC-2 Kahe Pt. sites.

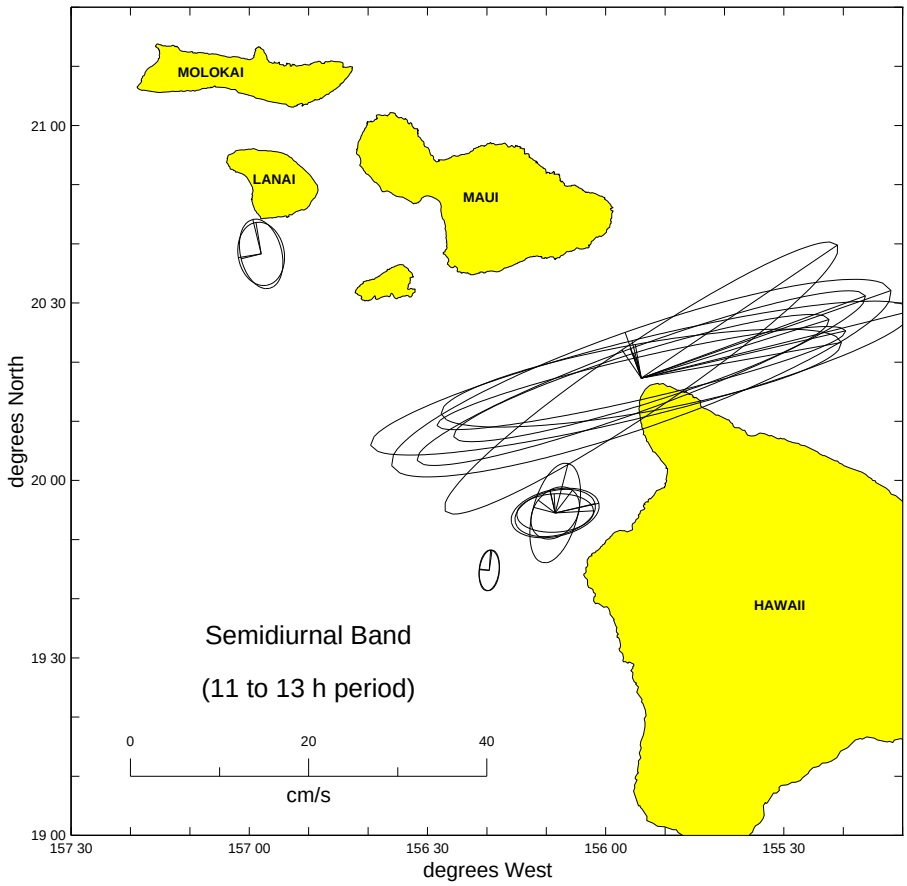

Figure 56: Current ellipses of the semidiurnal motion (11 to 13 h period) at the DUMAND, OTEC-1 Keahole Pt., Alenuihaha Seadata and Lanai sites.

References

Abramowitz, Milton and Irene A. Stegun, 1972: Handbook of Mathematical Functions (9th edition). Dover Publications, Inc., N. Y.

Bendat, Julius S. and Allan G. Piersol, 1986: Random Data (2nd edition). John Wiley & Sons, N. Y.

Brink, K. H., 1989: The effect of stratification on seamount-trapped waves. *Deep-Sea Res.* **36**, 825–844.

Brink, K. H., 1990: On the generation of seamount-trapped waves. *Deep-Sea Res.* **37**, 1569–1582.

Chambers, L. G., 1965: On long waves on a rotating earth. *J. Fluid Mech.* **22**, 209–216.

Davis, Russ E., 1976: Predictability of Sea Surface Temperature and Sea Level Pressure Anomalies over the North Pacific Ocean. *J. Phys. Ocean.* **6**, 249–266.

Davis, Russ E. and Philip S. Bogden, 1989: Variability on the California Shelf Forced by Local and Remote Winds during the Coastal Ocean Dynamics Experiment. *J. Geophys. Res.* **94**, 4763–4783.

Fjeldstad, J. E., 1933: Interne Wellen. *Geofysiske Publikasjoner* 10:6.

Gill, A. E. and A. J. Clarke, 1974: Wind-induced upwelling, coastal currents and sea-level changes. *Deep-Sea Res.* **21**, 325–345.

Godin, Gabriel, 1972: *The Analysis of Tides.* University of Toronto Press, 220–232.

Hogg, Nelson G., 1980: Observations of Internal Kelvin Waves Trapped Round Bermuda. *J. Phys. Ocean.* **10**, 1353–1376.

Jones, D. S., 1964: *The Theory of Electromagnetism.* The Macmillian Company, N.Y., 450–456.

Koopmans, L. H., 1974: The Spectral Analysis of Time Series. *Probability and Mathematical Statistics: A Series of Monographs and Textbooks* **22**, Academic Press, N.Y., 284.

Kundu, Pijush K., 1990: *Fluid Mechanics.* Academic Press Inc., San Diego, 322–325.

Lamb, Sir Horace, 1945: *Hydrodynamics* (6th edition). Dover Publications, N. Y., 320–324.

Lien, Ren-Chieh, 1985: Study of the internal wave field off Kahe Point. Master's Thesis, University of Hawaii.

Longuet-Higgins, M. S., 1969: On the trapping of long-period waves round islands. *J. Fluid Mech.* **37**, 773–784.

Longuet-Higgins, M. S., 1970: Steady currents induced by oscillations round islands. *J. Fluid Mech.* **42**, 701–720.

Luther, Douglas S., 1985: Trapped waves around the Hawaiian Islands. *'Aha Huliko'a Proceedings*, Hawaiian Institute of Geophysics, 261–301.

Miyata, Motoyasu and Gordon W. Groves, 1971: A Study of the Effects of Local and Distant Weather on Sea Level in Hawaii. *J. Phys. Ocean.* **1**, 203–213.

MÜLLER, P. AND G. SIEDLER, 1976: Consistency relations for internal waves. *Deep-Sea Res.* **23**, 613–628.

NATIONAL OCEANOGRAPHIC DATA CENTER, 1994: *Sea Level Data from the TOGA Sea Level Center and the Permanent Service for Mean Sea Level.* CD-ROM NODC-42. U. S. Dept. of Commerce, NOAA, Washington, D. C.

NOBLE, MARLENE A., LESLIE K. ROSENFELD, ROBERT L. SMITH, JAMES V. GARDNER AND ROBERT C. BEARDSLEY, 1987: Tidal Currents Seaward of the Northern California Continental Shelf. *J. Geophys. Res.* **92**, 1733–1744.

NOBLE, MARLENE A., K. H. BRINK AND CHARLES C. ERIKSEN, 1994: Diurnal-period currents trapped above Fieberling Guyot: observed characteristics and model comparisons. *Deep-Sea Res.* **41**, 643–658.

PATZERT, WILLIAM C. AND KLAUS WYRTKI, 1974: Anticyclonic flow around the Hawaiian Islands indicated by current meter data. *J. Phys. Ocean.* **4**, 673–676.

PLATZMAN, GEORGE W., GARY A. CURTIS, KIRK S. HANSEN, AND RICHARD D. SLATER, 1981: Normal Modes of the World Ocean, Part II: Description of Modes in the Period Range 8 to 80 Hours. *J. Phys. Ocean.* **11**, 579–603.

RHINES, PETER, 1970: Edge-, Bottom-, and Rossby Waves in a Rotating Stratified Fluid. *Geophys. Fluid Dyn.* **1**, 273–302.

WUNSCH, CARL, 1972: The spectrum from two years to two minutes of temperature fluctuations in the main thermocline at Bermuda. *Deep-Sea Res.* **19**, 577–593.

WYRTKI, KLAUS, VOLKER GRAEFE AND WM. PATZERT, 1969: Current observations in the Hawaiian Archipelago. Hawaiian Institute of Geophysics report HIG-69-15.